Summer 7-2024

Additively Manufactured Flexible Piezoelectric Wave-Based Multifunctional Sensor

Rishikesh Srinivasaraghavan Govindarajan
Embry-Riddle Aeronautical University, srinivr1@my.erau.edu

By

A Dissertation Submitted to the Faculty of Embry-Riddle Aeronautical University

In Partial Fulfillment of the Requirements for the Degree of

Doctor of Philosophy in Aerospace Engineering

Embry-Riddle Aeronautical University

Daytona Beach, Florida

To my cherished family,

To my parents and brother, whose unwavering love, support, and guidance have been the cornerstone of my journey, I am forever grateful. Your sacrifices and encouragement have propelled me forward, shaping me into who I am today. Each step of this path, from the earliest days of my academic pursuits to this momentous achievement, has been enriched by your presence and belief in me. Thank you for being my constant pillar of strength.

To my esteemed teachers,

I extend my deepest appreciation to those who have illuminated my path with knowledge and wisdom since the beginning of my educational journey. Your dedication, guidance, and passion for teaching have inspired me to strive for excellence and pursue my aspirations. Your influence on my life and academic growth is immeasurable, and I am forever indebted to you for your invaluable contributions to my success.

This dedication is not merely a recognition of my own efforts but a tribute to the myriad ways you have facilitated my success. Your love and sacrifices have made this achievement possible.

With deepest gratitude and love,
Rishi

ACKNOWLEDGEMENTS

I am profoundly grateful to my advisors, Dr. Daewon Kim and Dr. Foram Madiyar, whose unwavering support, mentorship, and invaluable guidance have been the cornerstone of my doctoral journey in Aerospace Engineering. Their thoughtful insights and encouragement have not only shaped my research endeavors but also nurtured my growth as a scholar. I deeply appreciate the opportunity they provided, including presenting at prestigious international conferences, where I could share my research findings and engage with peers in meaningful discussions. I extend my heartful appreciation to my esteemed committee members, Dr. Alberto Mello, Dr. Mandar Kulkarni, and Dr. Eduardo Rojas, for their invaluable feedback and encouragement throughout this academic pursuit.

My sincere gratitude goes to the dedicated lab supervisors who graciously provided access to essential research facilities, enabling me to conduct my experiments and analyses effectively. I am also thankful to the Department of Aerospace Engineering and the Department of Physical Science for their financial support and academic resources, which have been instrumental in advancing my research endeavors.

I wish to express my profound thanks to my cherished friends and colleagues, Stan, Zefu, Taylor, Nicholas, Suma, and Sandeep, for their unwavering support, camaraderie, and encouragement during this treasurable journey. Their friendship has been a personal and professional source of strength and inspiration.

Lastly, I am deeply indebted to my beloved parents, Mr. Govindarajan and Mrs. Rani, and my esteemed brother, Dr. Srinivasavaradan, for their unconditional love, staunch encouragement, and support. Their sacrifices and belief in my abilities have been the driving force behind my academic achievement and personal growth.

ABSTRACT

The demand for acoustic wave-based sensors has rapidly increased in the aerospace, chemical, gas, and biological fields due to their versatility in sensing measurands. This study aims to develop a flexible piezoelectric sensor exhibiting enhanced piezoelectric properties using additive manufacturing techniques that can detect mechanical strains and gas or volatile organic compounds (VOCs) by incorporating functional material into the sensing layer. This research explores piezoelectric substrate fabrication through diverse additive manufacturing techniques, including new material development made of polymer/nano-fillers with electrodes that are filled using different printing techniques. Notably, the design of the interdigital transducer (IDT) in the piezoelectric sensor is crucial as it determines the effectiveness of wave propagation, providing invaluable information for desired parameters. Moreover, this research investigates the characteristics and effectiveness of sensors with various IDT layouts placed in different configurations through numerical and experimental analysis. The numerical study involves 3D modeling of sensor design to examine wave characteristics and sensor performance in both time and frequency domains. A well-known PVDF polymer is modeled to ensure the concordance between the theoretical (COM MATLAB algorithm), numerical, and experimental results with surface-mounted and embedded IDTs. Additionally, the developed sensor's strain detection capability is explored by measuring the change in scattering parameters using a network analyzer. The primary results serve as a foundation, helping to define an approach to predict sensor behavior for specific designs in varying conditions. This, in turn, extends the sensor's application for multifunctional devices by integrating a nanoparticle sensing layer capable of detecting various concentrations of VOC. Finally, the implementation and feasibility of the developed sensor for wireless sensing and VOC detection are studied.

TABLE OF CONTENTS

LIST OF FIGURES

LIST OF TABLES

NOMENCLATURE

2PP	Two Photon Polymerization
ADS	Advanced Design System
AM	Additive Manufacturing
BAW	Bulk Acoustic Wave
BNNT	Boron nitride nanotubes
BTO	Barium titanate
BVD	Butterworth-Van Dyke
CAD	Computer Aided Design
CCTO	Copper calcium titanate
CNT	Carbon nanotube
CO_2	Carbon dioxide
COM	Coupling of Modes
CVD	Chemical Vapor Deposition
DAQ	Data Acquisition
DDM	Direct Digital Manufacturing
DEF	Diethly fumarate
DIC	Digital Image Correlation
DLP	Digital Light Processing
DMA	Dynamic Mechanical Analysis
DMF	Dimethylformamide
DMSO	Dimethyl sulfoxide
DSC	Differential Scanning Calorimeter
DUT	Device Under Test
EBL	Electron Beam Lithography
EBM	Electron Beam Melting
EDX	Energy Dispersive X-Ray
FDM	Fused Deposition Modeling

FDM	Fused Deposition Modeling
FEM	Finite Element Method
FFF	Fused Filament Fabrication
FOM	Figure of Merit
FTIR	Fourier Transform Infrared Spectroscopy
GNP	Graphene Nanoplatelets
IDT	Inter Digital Transducer
IL	Insertion Loss
KNN	Potassium sodium niobate
LCD	Liquid Crystal Display
$LiNbO_3$	Lithium niobate
$LiTaO_3$	Lithium tantalite
MEMS	Microelectromechanical System
Micro-CT	Micro Computed Tomography
NA	Numerical Aperture
NDT	Nondestructive Testing
NH_3	Ammonia
NO_2	Nitrogen dioxide
PA	Polyamide
$PbTiO_3$	Lead(II) titanate
PC	Polycarbonate
PDMS	Polydimethylsiloxane
PEDOT: PSS	poly(3,4-ethylene-dioxythiophene): poly(styrenesulfonate)
PFM	Piezoresponse force microscopy
PGMEA	Propylene glycol monomethyl ether acetate
PMMA	Polymethyl methacrylate
PVC	Polyvinyl chloride
PVD	Physical Vapor Deposition

PVDF	Polyvinylidene fluoride
PVDF-TrFE	Polyvinylidene trifluoroethylene
PVTF	Polyvinylidene fluoride-trifluoroethylene
PZT	Lead zirconate titanate
RF	Radio Frequency
RMS	Root mean square
SAW	Surface Acoustic Wave
SBN	Strontium barium niobate
SEM	Scanning Electron Microscope
SHM	Structural Health Monitoring
SH-SAW	Shear horizontal Surface Acoustic Wave
SLA	Stereolithography
SLS	Selective Laser Sintering
SNR	Signal Noise Ratio
UAV	Unmanned Aerial Vehicle
UV	Ultraviolet
VNA	Vector Network Analyzer
VOC	Volatile Organic Compound
XRD	X-Ray Diffraction
ZnO	Zinc Oxide

1 Introduction

This chapter elucidates the motivation behind the research work conducted on additive manufacturing of piezoelectric sensors with multifunctional capabilities, outlining the primary objectives of this research in achieving efficient AM printed sensor devices.

1.1 Motivation

In today's fast-paced world, where technological advancements drive innovation across various industries, the demand for smart sensing solutions is ever-growing. From structural health monitoring (SHM) in engineering fields to advanced biomedical applications, the necessity for efficient, reliable, and versatile sensors has become increasingly evident. In response to these challenges, the intersection of additive manufacturing (AM) and piezoelectric materials presents a compelling avenue for innovation, promising unprecedented flexibility and customization in sensor design and fabrication.

Traditional sensing technologies, while indispensable in many respects, often face inherent limitations that impede their efficiency in modern applications. The rigid nature of sensor materials, coupled with the complexity of fabrication processes, poses significant challenges in meeting the evolving demands of emerging technologies such as flexible sensors suitable for electronic devices. Moreover, conventional sensors may lack compatibility with the intricate geometries and dynamic environments encountered in real-world scenarios, thereby constraining their utility and adaptability.

This research seeks to bridge the gap between conventional sensing methodologies and the growing demands of contemporary applications by harnessing the synergistic potential of additive manufacturing and piezoelectric materials. AM, with its inherent capabilities for precise control of geometry and customizable design, offers a paradigm shift in sensor fabrication. By leveraging AM techniques, it becomes possible to create flexible, intricate sensor architectures that seamlessly

conform to irregular shapes and dynamic environments. However, it is important to recognize that certain limitations are inherent to every manufacturing technique. Thus, it is crucial to identify these limitations for various AM methods in flexible sensor fabrication and establish approaches to improve manufacturing quality. By addressing these challenges, researchers can make informed decisions about selecting and modifying the chosen AM technique to expedite their research.

Furthermore, the integration of piezoelectric materials amplifies the sensing capabilities of these devices, endowing them with heightened sensitivity, responsiveness, and energy storage functionalities. Piezoelectric sensors, capable of detecting mechanical stimuli such as strain, pressure, and vibration, represent a versatile solution for a myriad of applications spanning SHM and human-machine interfaces.

What sets the proposed research apart is its focus on developing multifunctional sensors that transcend the limitations of traditional sensing technologies. By seamlessly integrating AM with piezoelectric materials, these sensors possess the capacity to perform multiple sensing tasks. Whether it entails monitoring structural integrity or detecting environmental changes, these sensors offer a versatile solution adaptable to diverse application requirements.

In summary, the motivation underlying this research endeavor lies in its aspiration to push the boundaries of sensor technology by combining the power of AM with the unique properties of piezoelectric materials. By developing flexible, multi-functional sensors that can be seamlessly integrated into various systems and applications, this research aims to pave the way for the new era of smart sensing solutions that are transformative in their capabilities and impact.

1.2 Significance

The significance of this research lies in its potential to transform the field of SHM through the development of smart, additively manufactured flexible piezoelectric wave-based multifunctional sensors. Traditional SHM methods often face challenges in terms of cost, reliability, and

scalability. By utilizing suitable AM techniques and the unique properties of piezoelectric materials, this research aims to overcome these limitations and offer a novel solution for real-time structural monitoring. These smart sensors are designed to detect various forms of structural stimuli, with high sensitivity and accuracy. Their flexibility and adaptability make them suitable for a wide range of applications across industries, including aerospace, biomedical, civil infrastructure and beyond.

By integrating advanced sensing capabilities directly into the structure itself, the need for periodic inspections and maintenance can be significantly reduced, leading to cost savings, improved safety, and enhanced operational efficiency. Additionally, the scalability of AM enables the mass production of these smart sensors, making them accessible to a broader range of industries and applications. Overall, this research has the potential to make significant contributions to the field of SHM, paving the way for safer, more reliable, and more sustainable structures and systems empowered by smart sensor technology.

1.3 Research Objectives

In alignment with the presented motivation and the literature review conducted in Chapter 2 on the current state of piezoelectric device fabrication, this section delineates the objectives of this research. Given the existing challenges in piezoelectric device fabrication, this dissetation endeavors to address key aspects involved in the development of novel additively manufactured multifunctional sensors. This includes elucidating fabrication methodologies, assessing the performance and manufacturability of sensor materials, exploring new methods and configurations for sensor device production, and optimizing design through necessary modeling techniques. The following objectives are formulated to tackle the prevailing issues:

- *Manufacturing* – Conduct a comprehensive analysis of potential additive manufacturing techniques aimed at reducing manufacturing complexity compared to traditional methods

and facilitating rapid prototyping. Describe, design, and evaluate a manufacturing procedure to improve printing quality and sensor performance.

- *Material performance* – Enhance the electromechanical performance of the developed sensor device through the improvement in piezoelectric properties. Explore various filler materials to determine the most effective means of enhancing properties considering the production process and investigate the effect of materials in sensing performance with efficacy.
- *Electrode material and performance* – Employ numerical modeling of different electrode configurations to improve sensitivity and figure of merits. Implement various deposition techniques for electrode configurations and locations related to sensor performance. Introduce embedded electrodes using respective fabrication techniques.
- *Multifunctionality* – Integrate functional material into the sensing layer to detect various concentrations of VOCs and addition of microstructures to enhance the active sensing area for the development of novel multi-functional sensors.
- *Sensor validation* – Validate the intended stimuli for each technique via various RF signal measurement techniques. Study the sensitivity among selected AM techniques for each parameter detected in varying environments.

2 Review of the Relevant Literature

This chapter reviews the current trends in SHM technology, Surface Acoustic Wave (SAW) sensors and sensing mechanisms via the AM process, and their configurations and applications. Based on the review, important conclusions are drawn throughout the chapter to specifically address the research objective and prepare the reader for the study's methodology and results.

2.1 Structural Health Monitoring

Structural health monitoring (SHM) is a class of damage detection and condition monitoring techniques that have been rapidly developed in the modern world to detect defects at the right time, which could prevent fatal damages or failures in structures with increased structural reliability and human safety. The necessity to monitor deformations that occur due to various loads, such as aerodynamic, thermal, and external damages in aerospace structures during flight, demands an unobstructed and intelligent sensing device to ensure safety. SHM stands at the forefront of modern engineering practices, offering a proactive approach to ensuring the integrity and safety of critical infrastructure. By leveraging advanced sensor technologies, data analytics, and predictive maintenance strategies, the SHM system provides continuous insights into the conditions of structures, enabling early detection of defects, damage or deterioration.

One of the key advantages of SHM is the ability to monitor structures continuously, in contrast to traditional NDT methods, which are typically performed intermittently. This continuous monitoring allows for the early detection of anomalies or deviations from expected behavior, enabling timely intervention to prevent further damage or failure. By providing real-time insights into structural health, SHM systems empower engineers to implement proactive maintenance strategies, minimizing risks and optimizing asset performance.

There are two main categories of SHM approach, active and passive. Passive SHM involves the continuous monitoring of structural parameters such as vibration, strain, and temperature,

without the need for external stimuli. Changes in these parameters over time can indicate the presence of damage or degradation within the structure. Active SHM, on the other hand, involves actively stimulating the structure with external stimuli, such as acoustic waves or electromagnetic fields, and analyzing the response to detect anomalies or defects. Both approaches have their unique advantages and applications, and the choice between them depends on factors such as the type of structure, the nature of the damage being monitored, and the desired level of sensitivity.

In the aerospace industry, where safety is paramount, SHM plays a critical role in ensuring the integrity and reliability of aircraft structures. By continuously monitoring critical components such as wings, fuselage, and engine components, SHM systems can detect early signs of damage or fatigue, allowing for proactive maintenance and repair. This proactive approach not only enhances flight safety but also reduces maintenance costs and extends the lifespan of aircraft, ultimately benefiting both operators and passengers.

SHM system comprises several important subsystems aimed at ensuring the safety, integrity, and longevity of critical structures and systems [1, 2]. Firstly, the sensor system is tasked with gathering data on various environmental factors and the condition of structures, including strain, displacement, temperature, humidity, and load variations [3-6]. These useful data are collected by utilizing wired and wireless in-situ sensors, which mainly contribute to the diagnosis stage. Secondly, the data acquisition and transmission subsystem collects and transmits the data gathered by the sensor system. The data processing and analysis subsystem then processes and analyzes the collected data for further utilization. Subsequently, the data management subsystem receives and stores the observed data. The structural health evaluation system assesses the condition of the intended structure, while the decision-making and management subsystem facilitates decision-making processes for structural maintenance, repair, and reinforcement. Together, these

subsystems enable the SHM system to provide real-time safety information, prioritize maintenance and repair tasks, detect anomalies, and validate design parameters, contributing to the overall safety and reliability of the aerospace structures. The SHM systems are summarized in Figure 2.1.

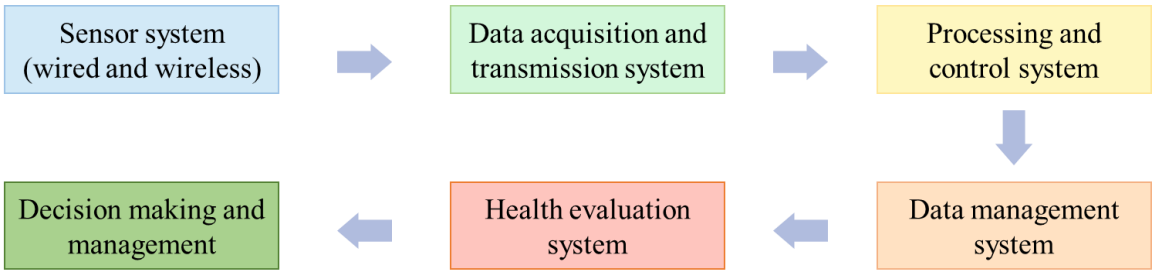

Figure 2.1 The architecture of SHM subsystems.

Recent advancements in sensor technology, data analytics, and wireless communication have revolutionized the field of SHM. Miniaturization of sensors has enabled their integration into structural components, providing real-time monitoring capabilities without compromising structural integrity. Wireless sensor networks allow for remote monitoring of structures, even in challenging environments or hard-to-reach locations. Moreover, advancements in data analytics, including machine learning algorithms [7], enable more accurate and reliable detection of structural anomalies, enhancing the effectiveness of SHM systems. The benefits of SHM over NDT are summarized in Table 2.1. While the benefits of SHM are clear, several challenges remain, including cost-effectiveness, regulatory compliance, and integration with existing infrastructure. Addressing these challenges requires collaboration between industry stakeholders, regulatory bodies, and research institutions. Continued advancements in sensor technology, materials science, and data analytics will further enhance the capabilities of SHM systems and expand their applicability across various sectors.

Table 2.1 Comparison between NDT and SHM technologies.

Factors	**NDT technology**	**SHM technology**
Detecting device	Separate from the structure or mounted temporarily	Mounted or embedded into the structure permanently
Maintenance	• Time-based • Reactive/ preventive	• Condition-based • Predictive/ intelligent
Detection mode	Offline	Online/ Offline
Detection time	Time-consuming and manual data collection	Quick and automatic data collection
Inaccessible area	Not during service	In service

As SHM technologies continue to evolve, they are expected to play an increasingly critical role in ensuring the safety, reliability, and sustainability of the intended structure worldwide. By harnessing the power of SHM, industries can minimize risks, optimize maintenance practices, and enhance operational efficiency. With ongoing research and development efforts focused on improving sensor performance, data analysis techniques, and system integration, the future of SHM holds great promise for enhancing the resilience and longevity of critical infrastructure.

2.2 Application of SHM in Aerospace Engineering

Aerospace structures operate under extreme conditions and are subjected to high levels of stress and fatigue during flight. Ensuring the structural integrity of aircraft components is paramount for safe and reliable operation. SHM systems have emerged as indispensable tools for continuously monitoring the health of aerospace structures, detecting early signs of damage, and predicting potential failures before they occur. This section explores the application of SHM in aerospace engineering, highlighting its significance in enhancing safety, reducing maintenance costs, and optimizing operational efficiency.

In the aerospace industry, safety is of paramount importance, and any compromise in structural integrity can have catastrophic consequences. SHM systems offer a proactive approach to maintenance by providing real-time data on the condition of aircraft structures. By monitoring parameters such as strain, load, vibration, and crack propagation, SHM systems enable early detection of damage, allowing for timely intervention and preventive maintenance. This proactive approach minimizes the risk of in-flight failures and ensures the safety of passengers and crew.

Aerospace SHM systems comprise a network of sensors strategically embedded within the aircraft structure to monitor key parameters. These sensors can include piezoelectric transducers, strain gauges, accelerometers, and acoustic emission sensors, among others [8-13]. The data collected by these sensors are processed and analyzed using advanced algorithms to assess the structural health and detect anomalies. Additionally, SHM systems often incorporate wireless communication and data transmission capabilities, enabling remote monitoring and real-time decision-making [14-16].

Several case studies demonstrate the efficacy of SHM systems in enhancing the safety and reliability of aerospace structures. Examples include the continuous monitoring of critical components such as wings, fuselage, and engine mounts to detect fatigue cracks, corrosion, and delamination. SHM systems have also been instrumental in identifying manufacturing defects and design flaws during the development phase of new aircraft models, leading to improvements in structural design and material selection. Additionally, SHM technology is being increasingly integrated into unmanned aerial vehicles (UAVs) and space exploration vehicles to ensure their structural integrity in harsh operating environments [17-21].

In the aerospace field, various commercially available sensors, such as strain gauges, thermocouples, and fiber optics, have been utilized to measure strain and temperature in different

aircraft components like wings, fuselage, and engine parts [22, 23]. However, these sensors have drawbacks such as requiring battery power and complex wire setups in the hub, making them challenging to deploy in inaccessible and harsh environments. In specific, mechanical strains for aerospace applications were measured using commercially available strain gauges or image correlation techniques, but they may not be suitable for high frequency and harsh environments due to their limited sensitivity and drift error over time [24, 25]. In contrast, the SHM field employs smart materials with a range of sensors operating on different principle mechanisms. Common principles include resistance, capacitance, and voltage-based mechanisms, wherein external loads induce changes in capacitance, resistance, or voltage generation, as shown in Figure 2.2.

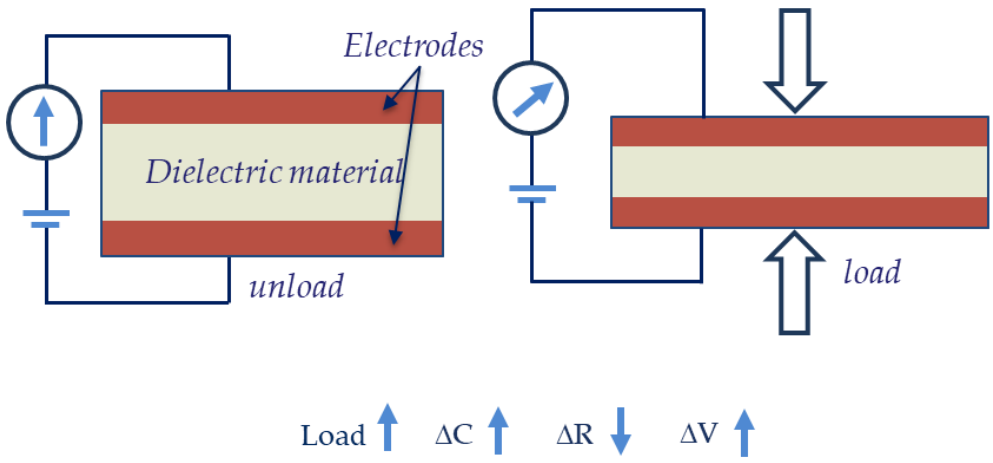

Figure 2.2 Schematic illustration of capacitive, resistive, and piezoelectric sensors.

Researchers have developed resistive or capacitive sensors using polymers such as Polydimethylsiloxane (PDMS), poly(methyl methacrylate) (PMMA), and Polyimide (PI), combined with electrode materials like silver nanowires, PEDOT: PSS, and carbon black solutions [26-38]. Despite their potential, these methods have drawbacks such as power consumption and susceptibility to temperature effects, which can impact sensor performance. Among these sensor

types, piezoelectric sensors, in specific wave-based acoustic sensors, stand out as a promising candidate due to its unique combination of high sensitivity and passive nature, offering reliable and accurate monitoring capabilities, which are explained in detail in the following sections.

2.3 Advancements and Application of Piezoelectric sensors

Piezoelectric sensors are devices that utilize the piezoelectric effect to convert mechanical stress into electrical signals. They play a crucial role in various industries, offering high sensitivity, fast response times, and wide-ranging applications. This section provides an overview of the advancements and applications of piezoelectric sensors across different sectors. The development of piezoelectric sensor technology has evolved significantly since its inception. Early applications were primarily focused on acoustic devices and ultrasonic transducers. However, advancements in materials science and manufacturing techniques have enabled the miniaturization, integration, and customization of piezoelectric sensors for diverse applications. This section also explores the key highlights in the evolution of piezoelectric sensor technology and their contribution to ensuring the safety and reliability of the structures.

In the field of SHM, piezoelectric sensors are utilized to detect and monitor structural changes in civil infrastructure, aerospace components, and mechanical systems. They offer advantages such as high sensitivity, low power consumption, and compatibility with harsh environments. Industrial automation relies on sensors for monitoring and controlling manufacturing processes. Among different sensors, piezoelectric sensors play a vital role in detecting vibration, pressure, force, and acceleration in machinery and equipment. They are used in condition monitoring systems, predictive maintenance, and quality control applications.

2.4 Piezoelectric Sensors and 3D printing Materials

Piezoelectric sensors play a pivotal role in SHM, offering unique capabilities in detecting structural deformations and mechanical stresses, with benefits discussed in the previous section.

Traditionally, piezoelectric materials like quartz crystals and ferroelectric ceramics were employed for such sensors [39-42]. However, advancements in materials science have led to the development of innovative piezoelectric composites, particularly in the realm of polymer-based materials.

Piezoelectric composites combine the high piezoelectric and dielectric properties of ceramics with the flexibility and pliability of polymers. These composites offer enhanced sensor functionalities by dispersing piezoelectric ceramic particles within a polymer matrix. The mechanical, piezoelectric, and dielectric properties of these composites can be tailored by adjusting the ceramic content during fabrication. Various connectivity patterns between the ceramic and polymer phases influence the electrical and mechanical performance of these composites, with 0-3 connectivity being a common configuration [43-45]. Noteworthy piezoelectric ceramic particles used in composites include Lead zirconate titanate (PZT), Barium titanate ($BaTiO_3$), Calcium copper titanate (CCTO), and Lead(II) titanate ($PbTiO_3$), while popular polymer matrices include PVDF, PDMS, and Polyvinyl chloride (PVC) [46-52].

The emergence of 3D printing technology has revolutionized material fabrication processes, offering unparalleled flexibility and customization in manufacturing. Table 2.2 summarizes the advantages and challenges of AM. From polymers to metals and ceramics, a diverse range of materials can be utilized in 3D printing, each with its unique properties and applications. In the context of SHM and piezoelectric sensor fabrication, the choice of 3D printing materials plays a critical role in determining the performance and functionality of the final product.

Polymer-based materials are widely used in 3D printing due to their versatility, cost-effectiveness, and ease of processing. Materials like polyamide (PA), acrylonitrile–butadiene–styrene copolymers (ABS), polycarbonate (PC), PVDF, and PDMS are commonly employed for rapid prototyping and manufacturing of sensor components [53-57]. These materials offer

excellent flexibility and can be tailored to specific mechanical and electrical properties required for piezoelectric sensor applications.

Ceramic-based materials offer unique properties such as high-temperature resistance, chemical inertness, and electrical insulation, making them ideal for specialized sensor applications. In 3D printing, ceramics like alumina, zirconia, and silicon carbide can be processed to create intricate sensor components with precise geometries [58-61]. Advanced ceramic AM techniques allow for the fabrication of complex sensor structures with enhanced performance characteristics, contributing to the advancement of SHM technology.

Table 2.2 Summary of Additive manufacturing advantages and challenges.

Advantages	**Challenges**
Design Freedom (complex structures)	Availability of materials
Material usage and cost reduction	Post processing requirement
Rapid prototyping	High quality CAD/ stl design requirement
Design shareability	Support structure wastage
Custom material adaptability	Unsustainable materials (ability to reuse/ recycle)

Among different AM processes, resin-based, filament-based, powder-based, and ink-based techniques are the most common techniques explored in the fabrication of polymer/ composites. Resin-based AM processes involve selectively curing liquid resin layer by layer using light sources such as UV light (e.g., Stereolithography (SLA), Liquid Crystal Display (LCD), and Digital Light Processing (DLP)) or two-photon polymerization (2PP). This technique offers several advantages, including high resolution, custom material compatibility, smooth surface finishes, moderate to fast

print speeds, and suitability for small scale production, making them ideal for producing intricate parts with fine details [62, 63]. However, they come with limitations such as limited material options, post-processing requirements, higher material costs, and safety precautions due to the liquid nature of the resins. Filament-based AM, including Fused Filament Fabrication (FFF) and Fused Deposition Modeling (FDM), utilizes a heated nozzle to extrude thermoplastic filament onto a build platform [64, 65]. This method offers cost-effective and durable parts suitable for functional prototypes and end-use applications. However, they typically have limited resolution, visible layer lines on printed parts, slower print speeds, and restricted material compatibility with certain advanced custom-made materials involving complicated fabrication processes. Powder-based AM, such as Selective Laser Sintering (SLS), Powder Bed Fusion (PBF), and Electron Beam Melting (EBM), selectively fuses powdered polymer material layer by layer using various energy sources [66]. These methods enable the production of complex geometries and support a wide range of materials, but they involve post-processing steps, which require specialized handling of hazards associated with powder materials and high equipment costs. Ink-based AM, specifically microdispensing, involves depositing liquid polymer material droplets onto a substrate layer by layer [67]. This method offers excellent resolution, material compatibility, and the ability to produce smooth or textured finishes, making it suitable for producing functional prototypes. They provide moderate to fast print speeds and are economical for prototyping. However, ink-based AM systems may have higher operating costs due to consumable materials, limited resolution compared to resin-based techniques, and nozzle clogging issues. The summary of polymer AM techniques with its highlights are summarized in Figure 2.3.

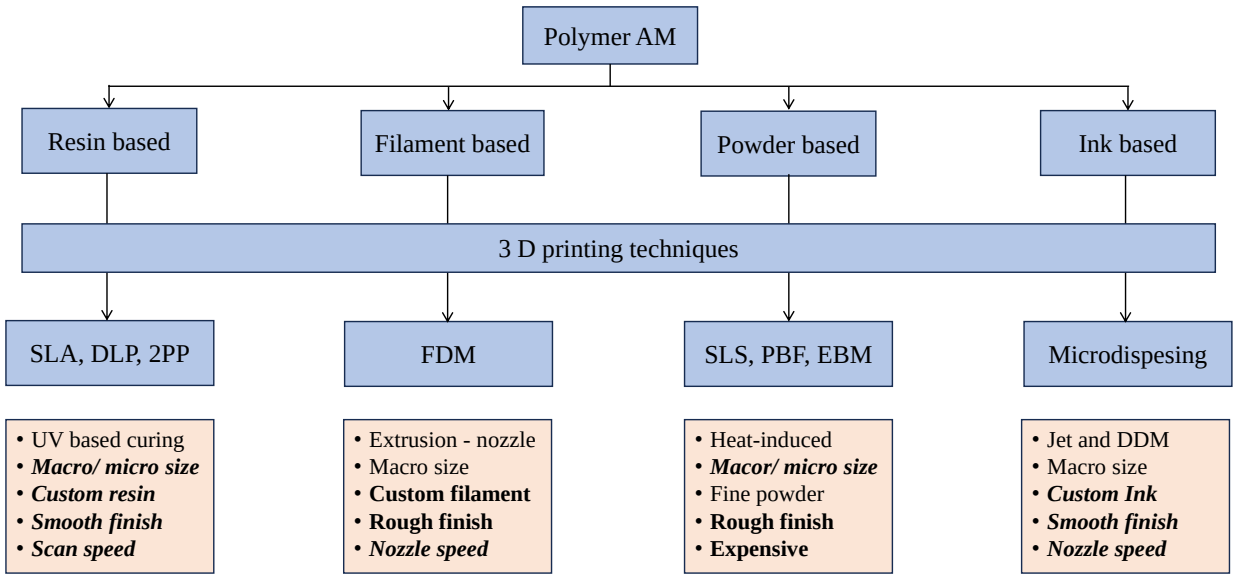

Figure 2.3 Flow chart of different AM techniques suitable for fabrication of polymers.

Based on the pros and cons of each technique, this study focuses on two prominent polymer AM techniques: ink-based and resin-based technology. Ink-based methods primarily involve microdispensing, while resin-based approaches encompass LCD and 2PP methods. These selected techniques offer distinct advantages and functionalities, making them particularly relevant to the objectives of this research.

The intersection of piezoelectric sensors and 3D printing materials presents an intriguing avenue for advanced sensor development. With 3D printing, researchers can precisely control the composition and structure of sensor components, including the piezoelectric elements, substrate, and electrodes. This flexibility allows for the customization of sensor properties to meet specific application requirements, such as sensitivity, frequency response, and durability. By leveraging the unique capabilities of 3D printing, engineers can explore novel piezoelectric materials, optimize sensor designs, and integrate sensors into complex structures with ease. Additionally,

AM enables rapid prototyping and iteration, accelerating the sensor development process and facilitating innovation in SHM and other fields.

Transitioning from the broader context of piezoelectric sensors and 3D printing materials, we delve into acoustic wave-based sensors, a subset of piezoelectric sensors, encompassing both surface and bulk wave phenomena [68, 69]. These sensors utilize piezoelectric materials to generate and detect acoustic waves propagating along the substrate. The integration of these sensors with 3D printing materials opens up new possibilities for enhanced sensor performance, miniaturization, and integration into complex structures.

2.5 Acoustic Wave-based Sensors

Acoustic sensors are a class of microelectromechanical systems (MEMS), which are capable of sensing physical (strain, temperature, and pressure) and chemical parameters based on wave propagation. Acoustic wave-based sensors, being highly sensitive, self-powered, unobstructed in size, and stale in a high-frequency range (<GHz), have attracted great interest in measuring mechanical strains. The acoustic sensor, with its exceptional capabilities, works under the principle of piezoelectric effect, i.e., direct effect (voltage generation by external stress) and converse effect (strain caused by electrical potential). These piezoelectric sensors generally consist of a piezoelectric substrate and interdigital transducer (IDT) placed at a certain distance named delay line where the generated wave propagates, as shown in Figure 2.4. Constitutive equation [70] for the measurement of strain or electric displacement in the material is described in quantitative form as,

$$S_p = s_{pq}^E T_q + d_{kp} E_k \tag{2.1}$$

$$D_i = d_{iq} T_q + \varepsilon_{ik}^S E_k \tag{2.2}$$

where S_p and T_q (Pa) describe the mechanical strain and stress components for the mechanical domain, D_i (Coulomb/m^2) and E_k (Volt/m) represent the electric displacement for the electric domain s_{pq}^{E} (Pa^{-1}), d_{kp} (Coulomb/N) and ε_{ik}^{S}denote the elastic stiffness, piezoelectric strain, and dielectric constants, respectively.

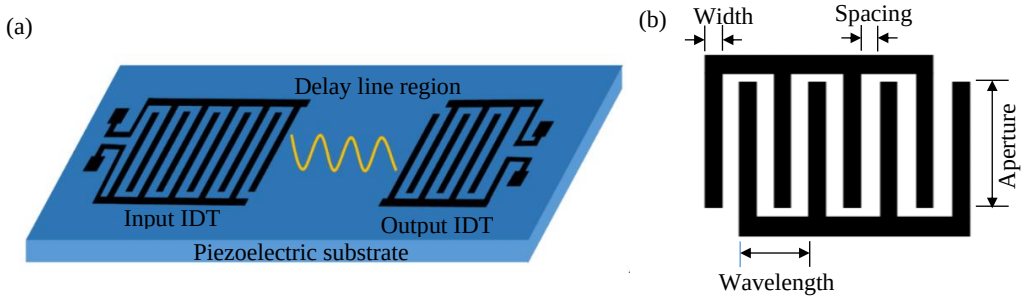

Figure 2.4 (a) Schematic of two-port IDT sensor and (b) IDT parameters.

Previously, commercially available traditional sensors such as strain gauges and thermocouples were used to measure strain and temperature that occurred in aircraft engine parts [25]. However, their complex wire setup and power supply requirements limited the range of applications, which can be circumvented by using an acoustic sensor utilized in this research. The following section will delve into piezoelectric substrate information, an important part of wave-based piezoelectric sensors.

2.6 Piezoelectric Composite Development

In recent years, significant strides have been made in the development of piezoelectric devices through the integration of well-known traditional and a few additive manufacturing techniques and the incorporation of micro and nanofillers. Researchers have explored various manufacturing techniques with the aim of enhancing the piezoelectric properties of these devices, which play a major role in the performance of developed devices for diverse applications. The literature review

offers a glimpse into extensive research conducted on piezoelectric device composite substrate development by scholars in this field, showcasing various techniques and outcomes achieved.

Chanankar et al. developed a pressure sensor based on PVDF polymer, enhancing its piezoelectric properties by adding PZT micro fillers. They achieved a maximum d_{33} of 22.93 pC/N and a dielectric constant of 104 with 60 wt.% of PZT, using electrospinning methods. Similarly, Wu et al. fabricated a novel sound-absorbing material using an electrospun PVDF membrane with CNT nanofibers. PVDF with a d_{33} of 10.51 pC/N with a maximum of 18.8 pC/N was reported with stretched PVDF/CNT composite. Moreover, Ponamma et al. fabricated PVDF-HFP mixed with Nickel ferrite nanoparticles ($NiFe_2O_4$) using chemical co-precipitation and electrospinning method. They reported a maximum dielectric constant value of 118 with 1 wt.% and a maximum voltage of 4 V being generated at 35 Hz with 2 wt.% of synthesized nanofiller, useful for energy harvester application.

In addition, Sahoo et al. fabricated an energy harvesting device based on PVDF-TrFE and ZnO coated with calcium as a nanofiller via the tape casting method. They achieved a maximum voltage of 0.28 V with an applied force of 0.5 N. Bhunia et al. contributed to the nanogenerator by preparing a film made of PVDF with ZnO particles utilizing the sol-gel technique. They reported a dielectric constant of 1.25, and by adding 0.03 M ZnO, the dielectric constant enhanced to 63.55 with a maximum output voltage of 4 V. Furthermore, Li et al. investigated the effect of BTO calcination in developed PVDF polymer via the hot-press method. They reported a measured d_{33} of 5 pC/N and a dielectric constant of 54 at 1 kHz. The maximum values achieved by introducing the calcination process were 20 pC/N and 120 at 1050 °C.

Moving forward, Cauda et al. explored the effect of dimensional confinement and oriented crystallization with an array of 1D polymeric nanowires with PVDF and PVTF. They showed that

nanoconfinement leads to preferential crystallization with an increment in crystalline phase, resulting in a 6.5 (PVDF) and 8.2 (PVTF) pC/N, an alternative method for electrothermal poling or mechanical stretching. Li et al. investigated the effect of adding a dispersant propylamine and silane coupling agent to PVDF-TrFE/ ZnO composite made using the spin coating method. They reported a maximum d_{33} of 34.7 pC/N when both agents were added, up from 14.8 pC/N with PVDF-TrFE and CNT composite.

Additionally, Wegener et al. prepared a 100 μm thin film using the solvent casting method based on PVDF-HFP and PZT ceramic fillers. They reported a dielectric constant of 62.6, and the highest d33 of up to 11 pC/N was found with 48 vol% ceramic. Fortunato et al. delved into the piezoelectric properties of composite film made of PVDF filled with GNP fabricated using solution casting via piezoresponse force microscopy (PFM). A maximum d33 value of 5.19 was reported with 0.5 wt% of GNP presence in the composite. They also addressed the performance with the addition of ZnO on top of the composite, resulting in a maximum d33 value of 6.08 pm/V. Kumar et al. studied the dielectric and figure of merit based on pyroelectric properties of the composite made of PVDF and strontium barium niobate (SBN) for sensor applications using the hot-press technique. Pi value of 13.475 μC/m2K and dielectric constant of 28 were obtained with 30 vol% of selected filler. Ponraj et al. developed a nanocrystal-based composite based on PVDF with KNN (an alternative option for lead-based fillers) using the hot-press technique. A maximum d_{33} value of 32 pC/N was obtained by adding 60 vol% of KNN crystals. Furthermore, Srinivasaraghavan et al. discussed the effect of adding micro and nanofillers such as PZT, CCTO, and CNTs in PVDF on the piezoelectric and dielectric properties. Results show that a maximum piezoelectric d_{33} of the composite reached up to 42 pC/N with CNT nanofillers, with the combination of PZT and CNT approaching closer to 28 pC/N after polarization prepared using the hot-press technique. In

addition, they demonstrated a wave-based strain sensor with higher sensitivity using the developed nanocomposites. Babu et al. developed a highly flexible material for soft sensor application consisting of PDMS filled with PZT ceramic based on the solution casting technique. They reported a maximum d_{33} value of 25 and a dielectric constant of 40 with 50 vol% of PZT. Additionally, Soin et al. prepared a PVDF film via a phase inversion technique with a maximum d_{33} value of 37 pC/N, which was achieved after quenching at room temperature, exhibiting higher crystalline behavior aimed for electroactive and energy harvesting applications. Parangusan et al. fabricated PVDF nanocomposite filled with iron-doped ZnO using solution casting along with gamma irradiation. After gamma irradiation with enhanced filler-polymer interaction, a maximum d_{33} of 9.44 pC/N and an output voltage of 2.4V were obtained with 2% nanoflowers.

Over the years, researchers have explored the potential of AM to further enhance the manufacturability of piezoelectric devices. Ikei et al. prepared an in-situ 3D printing based on FDM with corona poling playing a significant effect increasing the d_{33} from almost none to 12 pC/N after applying 8 kV with an applied elevated temperature. Similarly, Kim et al. presented an FDM-based 3D printing process made of PVDF with an obtained maximum d_{31} value of 0.048 pC/N with 12 kV electric voltage supplied using the corona poling technique aimed for sensor and energy harvesting applications. Additionally, Kirkpatrick et al. demonstrated piezoelectric behavior using FDM printed PVDF sample exhibiting a maximum d_{33} value of 0.36 pC/N for a capacitance-based sensor. Furthermore, Bodkhe et al. developed a single-step ink writing-based 3D printing system to fabricate a piezoelectric substrate assisted with solvent evaporation and polarization. A maximum d_{31} value of 18 pC/N with a 2.8 V output response was reported when 10 wt.% of BTO was added. Kim et al. developed a nanocomposite filament made of PVDF infused with MWCNT and BTO suitable for FDM based AM. They reported a maximum dielectric

constant of 118 and a dielectric loss of 0.11 measured at 1 kHz with the addition of 1.7 wt.% CNT and 45 wt.% BTO nanoparticles into the base polymer. Transitioning to alternative AM approaches, Yuan et al. reported a poling-free piezoelectric pressure sensor application made of PVDF and PZT using the direct ink writing technique. By implementing ball milling, they induced a stretch effect, resulting in a maximum dielectric constant of 9.8 and a loss tangent of 0.17 measured at 100 Hz with seven layers of piezoelectric composite developed. All the piezoelectric properties discussed in the literature are summarized with the fabrication method in Table 2.3 for reference.

Table 2.3 Summary of piezoelectric composite materials with PVDF base polymer fabricated using traditional and 3D printing manufacturing techniques.

Fabrication method	**Materials**	**Measured property**	**Application**
Solution casting [71]	PVDF/ Fe-ZnO and ZnO	d_{33} = 6.15 (PVDF) and 9.44 (PVDF/ 2%) pC/N	Piezoelectric generator
Template wetting [72]	PVDF/ PVTF	d_{33} = 6.5 and 8.2 pm/V	Piezoelectric device
Phase inversion [73]	PVDF	d_{33} = 37 pC/N quenched at room temperature	Electroactive and energy harvesting
Solution casted [74]	PDMS/ PZT	d_{33} = 25 pC/N, ε_r= 40, g_{33} = 75 mVm/N	Soft sensor and transducer
Hot-press [75]	PVDF/ KNN	d_{33} = 10 (40 vol%) - 32 (60 vol%) pC/N	Piezoelectric device
Hot-press [76]	PVDF/ SBN	P_i = 1.4 (pure)- 13.475 μC/m^{2}K; ε_r=28 (30 vol%)	Piezoelectric device

Solution casting [77]	PVDF/ GNP	d_{33} = 2.24 (pure) and 5.19 (0.5 wt%)	Piezoelectric generator
Solution casting [78]	PVDF/ GNP/ ZnO	d_{33} = 6.08 pm/V	Piezoelectric film
Solvent casting [79]	PVDF-HFP/ PZT	d_{33} = 11 pC/N, ε_r = 62.6 (48 vol%)	Piezoelectric film
Hot-press [47, 80]	PVDF/ PZT, CNT, and CCTO	d_{33} = 16 (pure) and 42 (2 wt% CNTs) pC/N	Strain sensor
Hot-press [81]	PVDF/ BTO	d_{33} = 5 pC/N and ε_r = 54 at 1 kHz	Piezoelectric film
Spin coating [82]	PVDF-TrFE/ ZnO	d_{33} = 14.8 pC/N	Piezoelectric generator
Electrospinning [83]	PVDF-HFP/ $NiFe_2O_4$	ε_r = 118 at 1 Hz; output voltage = 4 V at 35 Hz	Energy harvester
Electrospinning [84]	PVDF/ PZT	d_{33} = 10.51 – 20 pC/N; ε_r= 21-104	Pressure sensor
Electrospinning [85]	PVDF/ CNTs	d_{33} = 10.5 (pure) – 18.8 (CNTs) pC/N	Sound absorbers
Tape casting [86]	PVDF-TrFE/ ZnO Ca-doped	Output voltage = 0.28 V at 0.51 N	Energy harvester
Sol-gel [87]	PVDF/ ZnO	ε_r= 1.25 (pure) – 63.55 (ZnO) at 1 kHz and output voltage = 4 V	Nanogenerator
FDM [88]	PVDF/ BTO	d_{33} = 0.01 (pure) and 0.101 (15 wt%) pC/N	Pressure sensor
FDM [89]	PVDF	d_{33} = 0.36 pC/N after poling	Capacitance sensor

FDM [90]	PVDF-TrFE	d_{33} = 4 after polarization	Pressure sensor
FDM [91]	PVDF	d_{31} = 0.048 pC/N after polarization	Sensor and energy harvesters
DIW [92]	PVDF/ BTO	d_{31} = 18 pC/N and output voltage = 2.8 V	Piezoelectric device
FDM [93]	PVDF/ MWCNT/BTO	ε_r= 118 at 1 kHz and loss tangent = 0.11	Sensor and energy harvester
DIW [94]	PVDF/ PZT	ε_r= 9.5 and loss tangent = 0.17 at 100 Hz	Pressure sensor

As of now, the existing literature predominantly revolves around traditional techniques, which often entail complex development processes and offer limited design flexibility. In contrast, the exploration of AM techniques for piezoelectric device development is still in its nascent stage. Particularly noteworthy is the focus on synthesizing new materials rather than relying solely on commercially available ones. This shift towards innovative materials and manufacturing methods holds promise for developing effective piezoelectric devices. Cognizant of this disparity between traditional and AM approaches, this research aims to bridge the gap by delving into material synthesis and assessing performance using selected AM techniques.

2.7 Current State of Wave-based Sensors

The following section intends to provide a detailed literature review of wave-based piezoelectric sensors with various types, modeling approaches, and research work with challenges intended to be addressed by the explored piezoelectric sensor developed in this study.

Previously, a strain measurement sensor made of $LiNbO_3$ using (SH-SAW) was fabricated, demonstrating a strain and temperature sensitivity of 77 ppm/°C and 1 ppm/με [95]. Another study

explored a SAW resonator mounted on a wafer stripe to measure longitudinal and lateral strain with sensitivities of -0.987 ppm/με and 0.190 ppm/με, respectively [96]. Additionally, a SAW sensor fabricated on a quartz substrate exhibited a sensitivity of 20 Hz/με to measure longitudinal strains [97]. A LiNbO3-based SAW sensor was also developed to measure pressure and temperature, showing sensitivities of 3.7 rad/bar and 0.013 rad/°C, respectively [98]. Furthermore, a two-port pressure sensor made of ST-cut quartz was fabricated to operate in harsh environments with a sensitivity of 14 Hz/psi [99]. Another sensor using langasite to detect oxygen with a sensing layer of tin oxide was also developed [100]. Similarly, various sensors have been utilized to detect mechanical strain, pressure, temperature, and chemicals [101-107].

In terms of numerical and theoretical approaches to developing efficient sensors prior to manufacturing, researchers have focused on several models. For instance, a LiNbO3 sensor with IDT modeling based on an equivalent circuit model was executed to operate at 100 MHz [108]. A SAW IDT design based on a COM model using the transmission matrix approach was explored to introduce a convenient cascading technique [109]. Additionally, some research works were conducted to numerically validate sensor performance based on time delay and frequency responses [110, 111]. Although these works provided significant insight into the multifunctional capability of the proposed wave-based sensor, their suitability for high-frequency range strain applications and harsh environments, as well as their lack of flexibility due to the substrate material nature, remain limited. Furthermore, a better interpretation of wave characteristics and design methodology with proper validation has yet to be examined. This research work aims to address these major drawbacks by selected theoretical, numerical, and experimental approaches. The findings from the discussed literature work are summarized in Table 2.4.

Table 2.4 Summary of SAW sensor development for different stimuli detection using traditional rigid substrates.

Sensor	**Substrate material**	**Electrode material**	**Sensitivity**
Mechanical strain	$LiNbO_3$	Aluminum	0.22 ppm/με
	128° $LiNbO_3$	Aluminum	0.18 ppm/με
	$LiNbO_3$	Aluminum	0.41 ppm/με
	Wafer	Gold	0.190 ppm/με
	AT-X Quartz	Aluminum	252 Hz/με
Pressure	ZnO/Si	Aluminum	130 ppm/bar
	AlN/Si	Molybdenum	112.68 ppm/MPa
	St-cut Quartz	Aluminum	14 Hz/psi
Temperature	$LiNbO_3$	Aluminum	77 ppm/°C
Oxygen	Langasite	Platinum	Low frequency
Humidity	ST-cut Quartz	Aluminum	~520 kHz

3 Methodology

In this chapter, the research approach for the sensor development, as well as the materials, printer technology, characterization techniques, and equipment used for validating sensor performance are discussed.

3.1 Research Approach

The research approach primarily centers on the three main constituents of the sensor: the substrate, IDT, and sensor performance validation. This research will predominantly explore ink-based and resin-based 3D printing among various AM processes due to the advantages outlined in Section 2.4. Material selections are specifically aimed at enhancing printability and piezoelectric properties by utilizing composites. Each printing process or new exploration of concepts involves thorough numerical validation using COMSOL Multiphysics software.

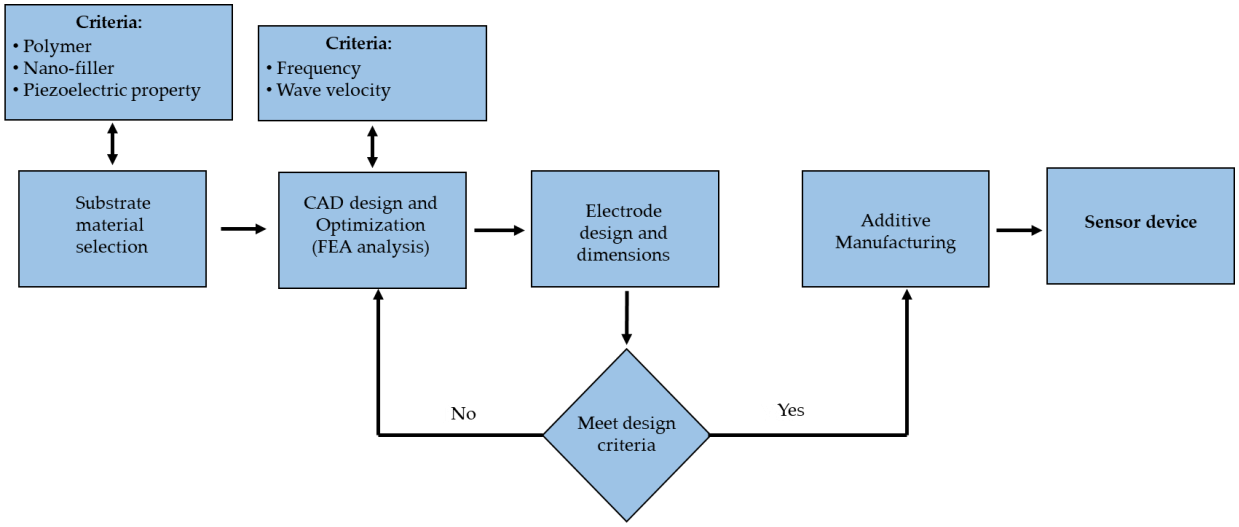

Figure 3.1 Flow chart of proposed sensor development based of different AM techniques.

Once the design meets the criteria, the selected fabrication process respective to the substrate and IDT will be executed, culminating in the development of the sensor device. The sensor

response is then measured under selected conditions to validate the expected functionality with sensitivity analysis. If the baseline expectations are not met, the selection process will be refined in an iterative process until the sensor exhibits optimal performance. Figure 3.1 summarizes the flow of the research approach in the development of the proposed sensor.

3.1.1 Design and Procedures

To begin with, CAD modeling serves as the initial step, facilitating the creation of precise geometrical models for the sensor components. Subsequently, the printing process unfolds layer by layer, guided by the CAD models, ensuring the accurate reproduction of the sensor's intricate features. Throughout this process, careful attention is paid to validate the print quality based on the selected printing technique, ensuring that each layer is deposited with precision and fidelity. Of particular importance is the quality of the printed IDT, as it directly influences the performance of the sensor. Thus, meticulous inspection and evaluation are conducted to ascertain the integrity and functionality of the IDT, laying the foundation for robust sensor operation. Each method utilized for property measurement or characterization technique is detailed extensively in the following section, providing comprehensive insights into the research methodology.

3.2 Methods used for Various Measurements

Different techniques with appropriate equipment to measure structural, thermal, piezoelectric, mechanical, optical, rheological, and sensor performance are presented in this section. As a quick outline, a glimpse of listed properties explored in various chapters of this study are listed below,

- *Structural properties*: crystalline phase information, homogeneity, and dispersion of micro and nanofillers.
- *Thermal properties*: Melting temperature, heat enthalpy, crystallinity content.

- *Piezoelectric properties*: Piezoelectric strain coefficient, dielectric constant at different frequencies, piezoelectric voltage coefficient, effect of polarization in aligning dipole presence in the developed piezoelectric materials.
- *Mechanical properties*: Young's modulus; viscoelastic properties such as storage modulus, loss modulus, complex modulus, and dissipation factor; and indentation hardness.
- *Optical properties*: The UV visible absorption spectrum for photocuring-based material.
- *Rheological properties*: Viscosity measurement with constant and varying shear rate.
- *Sensor performance*: Irrespective of the application aimed for each chapter or concept explored in multiple approaches, as the developed device is RF-based, the Scattering parameter with a frequency sweep, along with capacitance, impedance, and admittance values, are mostly measured specifically to the optimal designs.

To begin with, Fourier Transform Infrared Spectroscopy (FTIR), is an analytical technique for investigating the molecular composition and crystalline structure of the materials. By subjecting a sample to infrared radiation, FTIR measures the transmittance or absorption of light at various frequencies, providing insights into the functional groups present in the material. This method is particularly useful for polymers incorporated with micro and nanofillers, as it helps identify their molecular composition and structural characteristics. Additionally, this technique is used to quantify the polar phase presence in this study, which is directly related to the piezoelectric property of the developed and utilized material in this research.

X-ray diffraction (XRD) is an essential technique for analyzing the crystal phase and structure of materials. By directing X-rays at a sample, XRD measures the diffraction patterns produced as the X-ray interacts with the crystal lattice. This pattern provides valuable information about the

arrangement of atoms within the material, allowing the identification of the crystalline phases and structural properties.

Raman spectroscopy is another powerful tool for characterizing materials, offering insights into their chemical composition and molecular structure. By shining laser light onto a sample, Raman spectroscopy measures the scattering of photons as they interact with the material's vibrational modes. This scattering produces a Raman spectrum, which can be analyzed to identify functional groups, molecular bonds, and other structural features. Unlike other spectroscopic techniques, Raman spectroscopy does not rely on the absorption of light by the material. Instead, it measures the inelastic scattering of photons, which is less affected by the black body effect. Therefore, Raman spectroscopy can provide insights into the chemical composition and structural properties of materials, even when they possess black body characteristics.

For morphological analysis, the scanning electron microscope (SEM) technique is utilized for investigating the distribution and homogeneity of polymer and selected fillers within the piezocomposite substrate developed, which is directly related to the quality assurance of the selected mixing techniques. By examining the surface morphology, SEM enables the precise analysis of particle dispersion and uniformity within the 3D printed sensor material. For different techniques explored in this research, the FEI Quanta 650 SEM machine is used to examine the surface quality. All samples are coated with ~0.2 μm Gold with 45 sec exposure for better conduction while imaging. In some cases, particle size was quantitatively determined by calculating the average size observed in the scanned microscope image. Additionally, the print quality in terms of dimensional accuracy and the surface roughness of the printed parts are measured using a Filmetrics Profilm 3D profilometer.

Differential Scanning Calorimetry (DSC) analysis was employed to investigate the thermal properties of the piezoelectric composite substrates. DSC measures the heat flow associated with material transitions as a function of temperature. In this study, thermal properties such as melting temperature, heat enthalpy, and crystallinity content were analyzed to provide insights into the thermal behavior, particularly the arrangements inside the polymer chain that move freely with additional heat flow, showing exothermic or endothermic peaks of the developed materials. The measurement data were collected using a Mettler Toledo DSC 3 (Columbus, OH, USA). To obtain thermogram data, the initial step involved setting the nitrogen gas flow rate to 10 mL/min. Samples were then weighed and encapsulated inside a 40 µL aluminum crucible, which was placed in the sample holder next to the reference crucible to follow the thermal cycle. The cycle involved isothermal and dynamic ramping from 30 °C to 180 °C at a heating rate of 10 °C/min.

Piezoelectric materials are subject to characterization based on critical properties, including the piezoelectric strain coefficient (d_{ij}), voltage constant (g_{ij}), dielectric permittivity (ε_r), and electromechanical coupling factor (k), which represents the main terminologies involved in the piezoelectric constitutive equation. The piezoelectric strain coefficient represents the induced polarization per unit stress applied in the thickness direction, as shown in Figure 3.2 (a). d_{33} was measured using an APC YE2730A piezometer (Mackeyville, PA, USA) with a 250 mN applied force. Achieving a higher d_{33} is beneficial as it showcases the mechanical displacements suitable for effective sensing applications. On the other hand, dielectric permittivity governs the capacity of material to be polarized under an applied electric field and is completely dependent on the material type and operational frequency. This constant was determined through parallel plate capacitor measurements of 3D printed samples sandwiched between aluminum plates. Capacitance values were obtained with a high precision Hioki IM 3570 impedance analyzer (Dalla, TX, USA)

across a frequency range from 100 Hz to 1 MHz. Additionally, the piezoelectric voltage constant (g_{33}), represent the electric filed produced by the piezoelectric material per unit of applied stress or the mechanical strain experienced per unit of applied displacement, was derived from the measured d_{33} and dielectric constant.

Mostly for semi-crystalline polymers, to induce the transition from non-polar α phase to polar active β phase, it is essential to subject the sample to stretching and polarization under a high electric field. Among different polarization techniques, corona poling, a non-contact method, offers advantages by eliminating surface defects from electrode contact, reducing the likelihood of arcing at high voltages, and ensuring uniform voltage distribution. In this technique, an electric charge is applied to a corona multiple needle setup, ionizing gas molecules around the sample's surface to create an electric field. Factors affecting poling efficiency include voltage amount, poling duration, and distance between the corona tip and sample surface.

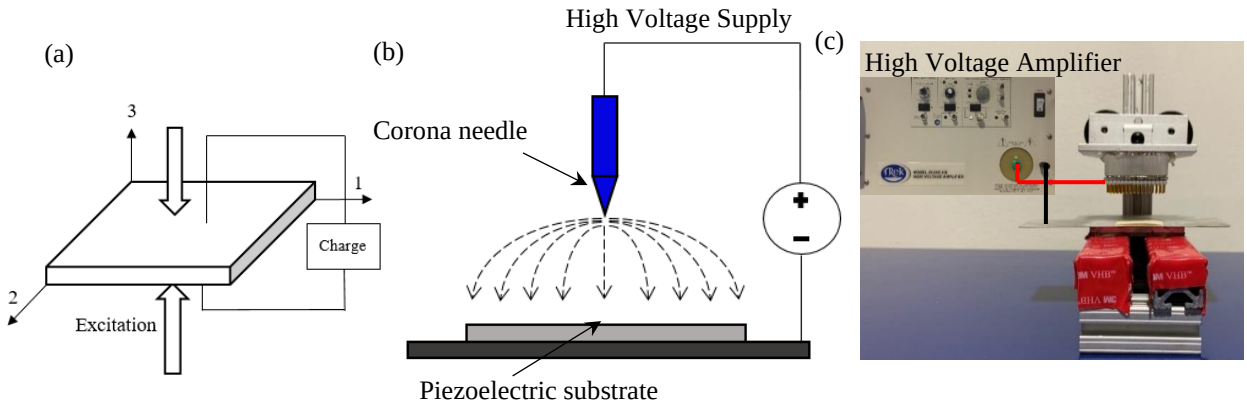

Figure 3.2 (a) Schematic of piezoelectric strain coefficient, (b) schematic of corona poling process and (c) actual setup for piezoelectric strain coefficient enhancement.

For each development method, the d_{33} values are measured after the poling process for the selected combinations. During poling, the randomly distributed diploes align along the direction of the applied external electric field. Figure 3.2 (b and c) depicts the corona poling schematic along with the custom-developed actual setup used for polarization throughout this research.

Mechanical characterization of the developed and 3D printed samples was conducted using a typical universal testing machine, the AMETEK CS225 (Berwyn, PA, USA), equipped with a 10 kg load cell, operating at a 1 mm/min extension rate. Additionally, a Bruker Hysitron TI-980 (Billercia, MA, USA) with a 10 mN low load transducer was utilized. Single indentations and micro-scale dynamic analyses were performed to study the material's reduced modulus, viscoelastic properties, and creep characteristics, respectively. For the single indentation test, a peak force of 5 mN and a dwell time of 5 seconds were used to measure the reduced modulus at a frequency of 100 Hz. In the microDMA test, a peak force of 5 mN and a dwell time of 5 seconds were applied to measure the storage modulus, loss modulus, and dissipation factor over a frequency sweep ranging from 10 to 220 Hz. Finally, the creep test was conducted for one hour with the same peak force.

Specific to optical properties, spectrophotometry experiments were conducted to obtain UV-visible spectra for the UV-curable material developed in this study. A UV-visible Go Direct SpectroVis Plus spectrophotometer was employed to measure the absorbance of the material over a range of wavelengths. Samples were prepared by dissolving the material into a solvent with a 1:9 ratio and placed in the spectrophotometer cuvette for analysis. The absorbance spectra were recorded in the UV-visible range, typically from 380 nm to 780 nm, providing insights into the material’s absorption characteristics and allowing for the determination of key parameters such as absorbance peaks and optical properties.

The rheological properties of the developed resins with varying proportions of constituents were conducted utilizing a TA Instruments HR 20 hybrid rheometer (New Castle, DE, USA). The testing geometry comprised a two 25 mm parallel plate with a 0.75 mm gap, with temperature control maintained by a Peltier plate setup. Two types of measurements were performed: 1) viscosity over a varying shear rate from 1 to 100 1/s at 25 °C; 2) viscosity at a constant shear rate of 100 1/s for 60 seconds duration at 25 °C.

The strain correlations are measured using the commercially available Digital Image Correlation (DIC) optical technique to determine the displacement, which can then be correlated with the frequency response obtained from the RF tests. A DIC system equipped with two 6 MP high-resolution cameras is employed for this purpose, with calibration performed using images to establish their precise location and angle relative to each other. The cameras are focused on the host structure with the developed sensor mounted. The region of interest, corresponding to the area under the sensor, is defined using VIC-3D software. As strain increases, the cameras track displacement in the Y direction between consecutive images by following the speckle pattern of the subsets. This non-contact optical technique allows for the measurement of quantitative strain values in various deformed shapes using a correlation algorithm applied to the selected area under the sensor.

The experimental setup for evaluating sensor performance involves key instruments tailored to specific electrical measurements. To capture the sensor's frequency response accurately, a Vector Network Analyzer (VNA) is employed for S-parameter measurements, which characterize the transmission of electromagnetic or acoustic waves propagating on the sensor. This allows for detailed analysis of how the sensor interacts with incident signals across different frequencies.

To be specific, S-parameters, or scattering parameters, are fundamental metrics used in electrical RF measurements to characterize the behavior of linear electrical networks or devices, such as filters, resonators, and sensors. These parameters describe how signals propagate through the device, including how much of the signal is reflected, transmitted, or absorbed at various frequencies. In a two-port network, the most relevant case to the sensor explored in this research, there are four S-parameters: S_{11}, S_{12}, S_{21}, and S_{22}. S_{21}, for example, represents the transmission coefficient between port 1 and port 2, indicating the ratio of output signal to input signal when the device is excited at port 1. Similarly, S_{11} represents the reflection coefficient at port 1, while S_{12} and S_{22} describe the transmission and reflection coefficient at port 2, respectively. Understanding these parameters is essential for analyzing the performance, impedance matching, and signal integrity of RF devices.

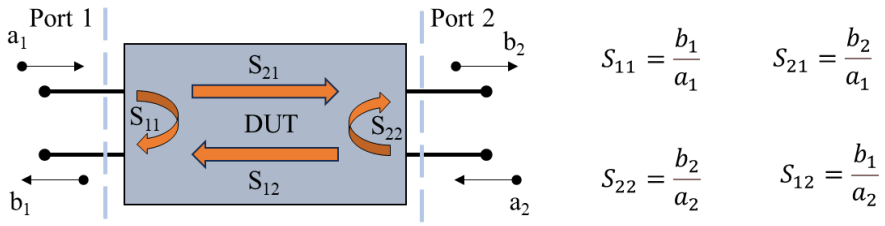

Figure 3.3 Two-port network showing incident and reflected waves used in scattering parameter coefficient from both sides of DUT.

Impedance and admittance values, represented by complex numbers, provide insights into the resistance and reactance of a device or a network at a given frequency. An impedance analyzer is utilized to access the response of the sensor, which provides valuable insights into the electrical behavior, aiding in the interpretation of its performance characteristics. The Smith chart, a graphical tool used in RF engineering, visualizes these impedance or admittance values to aid in

impedance matching and network analysis. By correlating impedance and admittance values with S-parameters, researchers can optimize RF-based systems for improved performance and efficiency. Overall, to visualize and interpret the collected data effectively, a basic chart illustrating S-parameters plots is generated.

The corresponding sections of the report will discuss specific details and results collected from each method associated with the chapters.

4 Microdispensing Technique

This section will explore the development of piezoelectric sensors, particularly the substrate and IDT, using the AM technique.

4.1 Background and Overview

Evaluation of aerospace structure's strain concentration due to several loads such as aerodynamic, thermal, and defects necessitates a real-time monitoring system that can provide beneficial information. Mechanical strains for aerospace applications are commonly measured using strain gauges or piezoresistive sensors, but they are not suitable for high frequency and harsh environments due to their limited sensitivity and drift error over time [24, 25]. To address this issue, a novel development of a Rayleigh wave-based sensor with enhanced piezoelectric properties is explored in this work by utilizing the AM potential. Generally, the IDT electrode design is patterned through traditional techniques such as photolithography or electron beam lithography [112]. As these techniques exhibit major limitations requiring clean room and the development of complex photomasks, which involve UV exposure, additive manufacturing can be deemed to be an ideal fabrication technique. Besides the deposition technique, the design of IDT plays a vibrant role in wave generation, which dictates the frequency responses measured in the signal. Evaluation of the IDT design towards operational frequency ranges is executed through FEA tools, which simulate and analyze the sensor response through parameters such as eigen frequency, scattering parameter, and time delay prior to fabrication [111, 113]. Direct digital manufacturing (DDM), a new technique evolved as an interconnection between AM and information communication technology (ICT) [114], which is a concept to match the requirements of Just in Time (JIT) production. Building upon the need for advanced monitoring systems, this chapter explores innovative approach in sensor development. The following research questions will guide the investigation: a) how can advanced manufacturing techniques and novel materials

enhance the fabrication and performance of acoustic wave-based sensor, particularly in achieving single-step fabrication of the entire sensor device? What are the optimal parameters for using the selected 3D printing technique to print high-quality sensors? c) will numerical analysis before fabrication increase the efficiency of the developed sensor? and d) how accurately does the AM printed sensor detect mechanical strains in attached host structures? Based on these research questions, the following hypotheses are developed: a) Utilizing advanced manufacturing techniques such as micro dispensing, in conjunction with novel materials like piezocomposites, will enable the single-step fabrication of sensors with enhanced performance characteristics, b) Optimizing parameters such as nozzle diameter, printing speed, and material composition in the selected 3D printing technique will result in high-quality sensors with improved durability compared to traditional manufacturing methods, c) FEA tool such as COMSOL simulations will effectively optimize the sensor performance, informing design refinements for improved reliability, and d) Resonant frequency shifts of the sensor will significantly correlate with the mechanical strain levels in the host structure. With the hypotheses in mind, the major objectives of this chapter are,

- Develop a thin, flexible substrate through DDM with enhanced piezoelectric properties.
- Improve IDT design using the FEA tool to meet design criteria.
- Microdispense the designed IDT pattern.
- Validate developed sensor strain detection capability.

4.2 Nanocomposite Substrate Development

4.2.1 Development of Piezoelectric Substrate

In this method, we intend to develop the SAW device completely using the microdispensing technique. To develop a flexible piezoelectric substrate, a polymer and nanocomposite-based substrate comprising PVDF as a polymer matric and CNTs as nano-fillers is designed and

fabricated. PVDF is a linear fluorinated hydrocarbon arranged by a repeating unit of -(CH_2-CF_2)- with four major possible polymorph phases, i.e., α, β, δ, and γ phases. Among them, the most common thermodynamically stable polar phase (β) is composed of all-trans conformation, presenting essential characteristics, such as ferroelectric properties, that can induce a strong dipole moment whereas the non-polar α phase's dipole arrangements cancel each other. To enhance the piezoelectric properties, the β phase can be obtained from different conformations, commonly through annealing, stretching, and aligning the dipoles [115, 116]. In order to make the fabricated PVDF nanocomposite piezoelectrically active, mechanical stretching or polarization under a higher electric field is necessary. On the other hand, CNTs play a vital role as nano-fillers with their renowned electrical and mechanical properties [117]. With the selected polymer and fillers' known properties, piezoelectric nanocomposite can be fabricated through common techniques such as compression molding, tape casting, and hot-press [118, 119]. Even after substrate fabrication, a separate technique is always required for SAW device development, especially for IDT deposition, and the substrate should also comprise flatness, which was lacking in conventional techniques. In this work, DDM, a new manufacturing paradigm [120] that exhibits freedom of design and modification in a cost-effective manner, is used to develop a SAW device (substrate and IDT) with desired flexibility and electrode patterns. DDM technique is carried out by following two steps: 1) design CAD model as input to a 3D printer and 2) fabricate SAW device maintaining structural integrity with desired printer parameters.

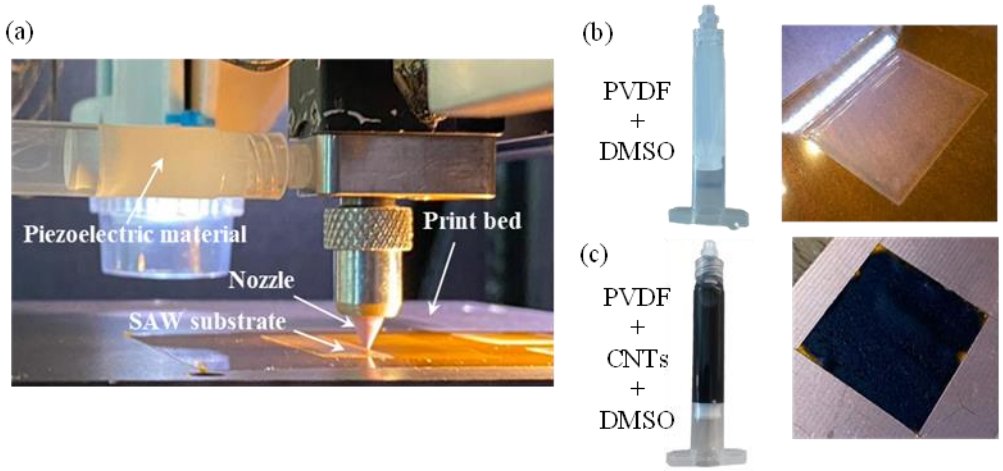

Figure 4.1 (a) Microsipensing of a piezoelectric substrate; (b) and (c) printed PVDF and PVDF/ CNTs substrate after curing.

The piezoelectric substrate is fabricated using the selected microdispensing nScrypt printer with high precision motion, as shown in Figure 4.1 (a). Polar solvent dimethyl sulfoxide (DMSO, 85 wt. %) is used to dissolve PVDF (15 wt. %) polymer through a THINKY mixer (ARM-310), which involves both rotational and revolution axis motion with a deaeration option (removing air bubbles). CNTs (2.5 wt. %) is also incorporated in combination with respective PVDF polymer and DMSO wt. % to form the nanocomposite (PVDF/CNTs) substrate. The substrate with less porosity, particle cluster, and agglomeration is fabricated using a 550 µm nozzle, as shown in Figure 2(b, c), and DMSO is completely evaporated in both substrates after curing. Printing parameters used for SAW device fabrication are mentioned in Table 4.1.

Table 4.1 nScrypt 2Dn series parameters for printing SAW device: substrate/ IDTs, speed of (IDT bus bar and terminal/ *denotes speed of IDT fingers).

	Nozzle diameter, µm	**Printing height, µm**	**Printing speed, mm/s**	**Pressure, psi**
PVDF	550	180	10	5
PVDF/CNTs	550	250	10	5
IDTs	100	40	5 /15*	7

4.2.2 Piezoelectric Property and Chemical Characterization

Piezoelectric properties are essential attributes that dictate a material's efficiency for sensing the desired measurand. Among important SAW device properties, such as d_{33}, ε_r, and coupling coefficient, piezoelectric coefficient (d_{33}) is measured using a piezometer, and enhancement in d_{33} is expected by incorporating CNT nanofillers to the polymer while maintaining desired flexibility. In specific, the semi-crystalline polymer PVDF exhibits four major polymorph phases (as mentioned earlier), α (trans gauche trans gauche', TGTG', nonpolar), β (all trans, TTTT, polar), δ (TGTG', polar), and γ (T3GT3G', polar), with the α and β phases being the most prevalent. Among these phases, the β phase is the essential thermodynamically stable form, particularly for piezo-, pyro-, and ferro-electric properties. In the β phase, the polymer chains adopt a zigzag configuration with an all-trans conformation, resulting in higher polarity. The crystalline region of the β phase consists of carbon backbones with fluorine atoms arranged on one side and hydrogen atoms on the opposite side, inducing a significant dipole moment. In contrast, the α phase exhibits a semi-helical antiparallel dipole configuration, where the dipole moments align in such a way that they cancel each other out. Various methods, such as annealing, drawing, and poling, are employed in general to induce phase transitions from nonpolar to polar crystalline phases, as depicted in Figure 4.2.

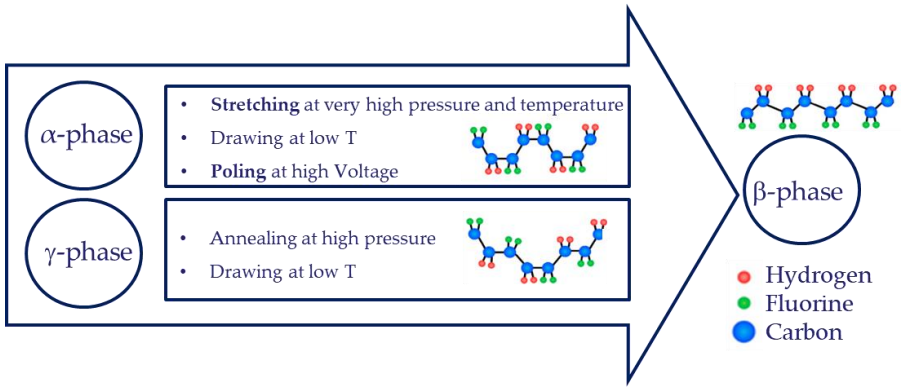

Figure 4.2 Methods of inducing phase transition from nonpolar to polar crystalline phase.

In this research, to convert the non-polar α phase to the active polar β phase, a non-contact polarization process is carried out where a high electric field is applied through electrically charged needles, which align the dipoles in piezoelectric substrate towards the applied electric field direction. A high voltage of 10 kV is applied to the sample placed 2 cm away from the needle tips. An increase in d_{33} is observed from the measured values after polarization, which ensures the dipole alignment. Additionally, a maximum d_{33} value of 43 pC/N is achieved in the PVDF/CNTs substrate with a 30.3 % increase after polarization. Measured piezoelectric coefficients before and after polarization are listed in Table 4.2.

Knowing the phase information of PVDF polymer is important as it plays a major role in piezoelectric properties. FTIR spectra of the fabricated PVDF substrate is analyzed to characterize the presence of different crystalline phases. An Agilent spectrometer is operated in a wavenumber range of 650-1550 cm^{-1} with automatic background correction. Figure 4.3 (a) shows the corresponding spectra such as 773 cm^{-1}, 874 cm^{-1} and 1070 cm^{-1} representing presence of α phase [121] and spectra at 835 cm^{-1}, 1167 cm^{-1}, 1230 cm^{-1} and 1401 cm^{-1} representing β phase presence [122]. These spectra denote major molecular motions, namely wagging, vibration, bending, and stretching of carbon, fluorine, and hydrogen presence in the polymer.

Table 4.2 Measured piezoelectric property of developed substrate using microdispening technique.

Material	**d_{33}, pC/N**	
	Unpolarized	**Polarized**
PVDF	9	14
PVDF/CNTs	33	43

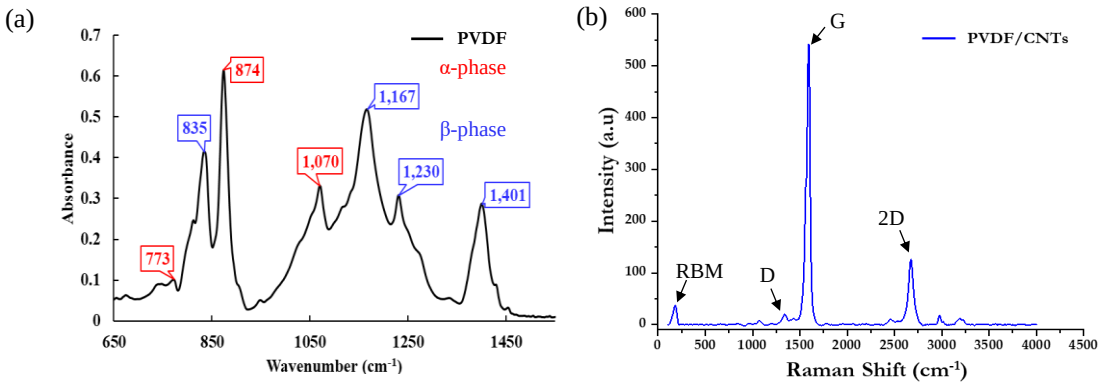

Figure 4.3 (a) FTIR absorbance spectra of PVDF substrate (b) Raman spectra of PVDF/ CNTs substrate.

Raman spectra analysis is also carried out to characterize the presence of CNT nanofillers, as they are the black body that absorbs all lights in FTIR and end up with a lot of noise in the spectra. The main noticeable bands for CNTs through Raman analysis are D (disordered), G (graphite), and RBM (radial breathing modes). Raman analysis with a laser wavelength of 532 nm excitation is used to examine all four main regions of CNTs. Figure 4.3 (b) displays the corresponding peak such as the RBM peak below 300 cm^{-1} (symmetrical radial vibration of carbon atoms), D peak at 1343 cm^{-1} (surface and structural defects), G band at 1594 cm^{-1} (longitudinal and transversal in-plane phonon), and 2D-band at 2658 cm^{-1} (symmetrical overtone of D band) [123]. From the D/G ratio, purity and defects in CNTs can be quantified [124]. Even though knowing the defect percent

will be beneficial, the main aim of Raman analysis is to characterize the presence of CNTs incorporated with PVDF polymer.

4.3 IDT Design and Fabrication using a Microdispensing Process

In this section, we explore the numerical design and precise fabrication of IDTs utilizing the microdispensing process. The subsections will cover the numerical analysis methodology to optimize the IDT design, ensuring enhanced performance and validation before experimentation, followed by a detailed description of the microdispensing technique used for the fabrication of the IDTs. These methods collectively contribute to the development of efficient flexible wave-based polymer sensors.

4.3.1 Numerical Analysis

Several parameters can reveal the device's acoustic wave performance in different aspects, such as the scattering parameters (S-parameters), insertion loss (IL), electrical impedance (Z), admittance (G), susceptance (B), and quality factor (Q-factor) in which S-parameters are the elements of the frequency-dependent matrix that model the reflection and transmission characteristics of a defined transmission line system [125]. The IL measures the loss of power that occurs due to the insertion of a component when a signal travels through the transmission system, which presents a network's transmitting ability and is often used to plot the device frequency response in decibel form [126]. Besides, an electrical impedance mismatch in a network could lead to avoidable signal loss. The electrical impedance [127] of the SAW device is generally related to several factors, such as substrate material properties (electromechanical coupling factor (k^2) and permittivity (ε)) and the IDT dimensions (acoustic aperture (ap), metalized ratio (η), numbers of finger pair (Np), and finger thickness (t)). In addition, a higher Q-factor produces a narrower bandwidth and a sharper frequency response peak near the center frequency, contributing to a higher sensor sensitivity.

It is essential to design an optimized IDT and its dimensions to develop a SAW sensor at an anticipated center frequency with low loss and high sensitivity. The wavelength is determined by both center frequency f_0 and SAW velocity v, which can be calculated as $\lambda = v/f_0$. IDT design with better performance can be developed by refining a few parameters, such as aperture, electrode material properties, and delay line distance, through numerical analysis. The numerical analysis solves the device directly from the material constants, device dimensions, and defined boundary conditions to evaluate the device's performance. In this paper, numerical analysis is carried out through COMSOL Multiphysics due to its dedicated piezoelectric interface for acoustic wave-based devices with all major factors considered.

Figures 4.4 (a) and (b) show the SAW sensor geometry with the IDT dimensions built in COMSOL Multiphysics and eigenfrequency mode occurred at 1.51 MHz, representing the surface acoustic wave mode. The S-parameter response of the SAW sensor made of PVDF with designed IDT is measured in a frequency range from 500 kHz to 3 MHz expecting a resonant peak near the surface wave mode eigenfrequency. Due to the complexity of composite substrate material properties, a substrate made of only PVDF is evaluated in numerical analysis. A fundamental frequency peak at 1.53 MHz is observed in both S_{11} and S_{21} analyzed responses, as shown in Figure 4.4 (c) and (d) respectively, which satisfies the design criteria.

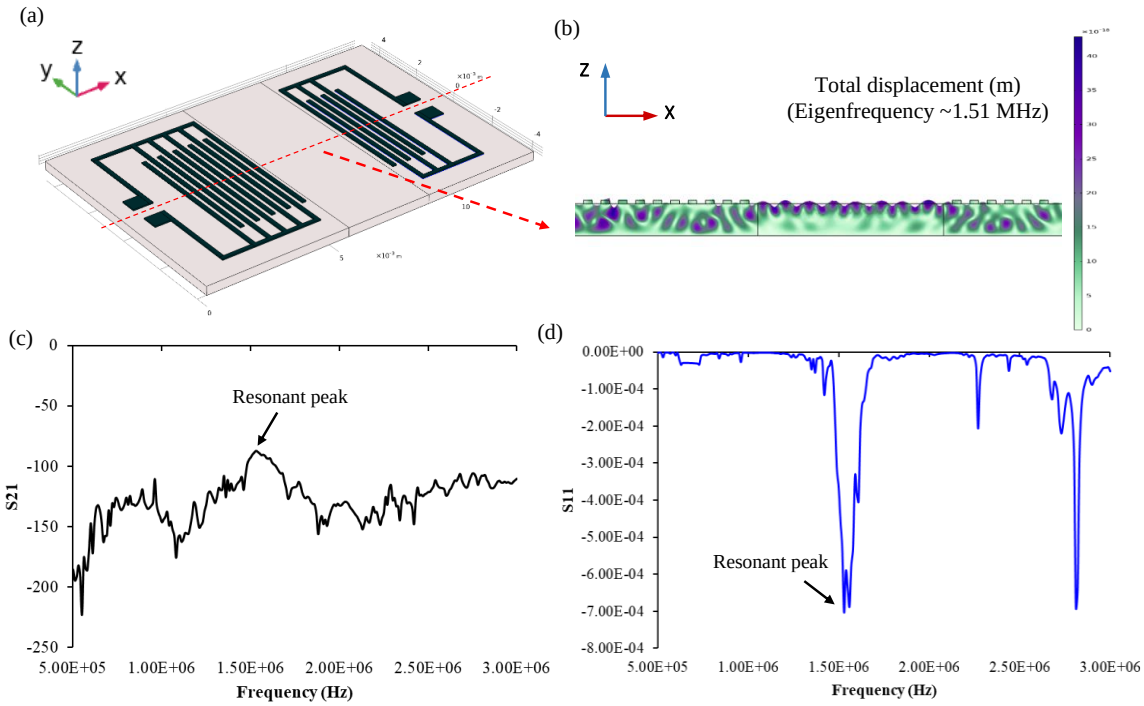

Figure 4.4 (a) 3D geometry of PVDF SAW; (b) SAW mode eigenfrequency; S-parameter responses; (c) S21 and (d) S11 response.

4.3.2 Microdispensing of Designed IDTs

A refined IDT design is used to print the input and output IDTs made of conductive silver paste on top of the developed substrate. Nozzle diameter and desired printing parameters are varied for different substrates, depending on the spacing requirements and material properties, as mentioned in Table 4.1. Printed IDT design with 150 µm spacing and other dimensions compared with previous work [119], as shown in Table 4.3, are examined through an FEI Quanta 650 scanning electron microscope (SEM) to evaluate the overlapping and continuity factor. Figure 4.5 shows a schematic of the IDT microdispensing process and SEM figures of input and output IDTs. It can be seen that IDTs made of silver paste are printed well without discontinuity or minor corner blobs and are well bonded to the base substrate.

Table 4.3 Redefined dimensions of SAW IDTs for microdispensing technique.

Dimension	**Initial design [119]**	**Refined design**
Finger width (free space width), μm	150 (500)	150 (150)
Metallized ratio (η)	0.23	0.5
Wavelength (λ), μm	1300	600
No. of input (output) finger pair (Np)	3 (2)	5 (3)
Acoustic aperture (ap), mm	3.5	5
Finger thickness (t), μm	100	40

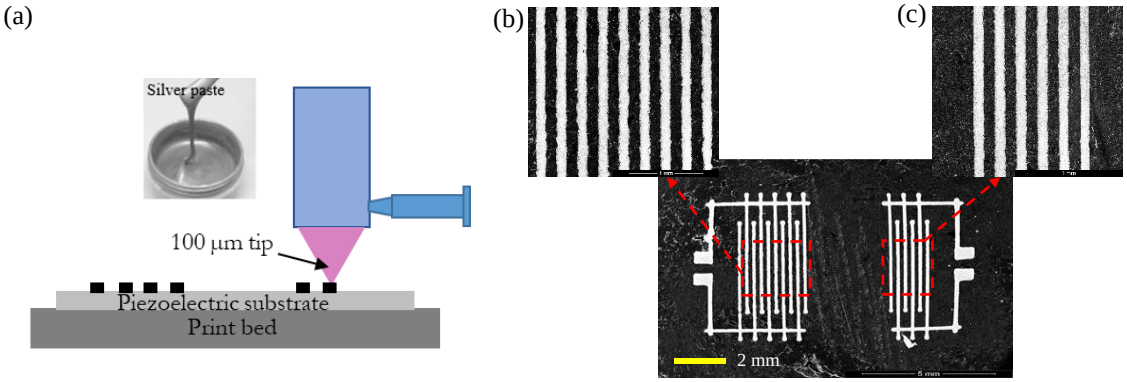

Figure 4.5 (a) Schematic of IDT (cross-section) microdispensing; SEM images of printed (b) input and (c) output IDTs.

4.4 Summary and Conclusion

In this work, a flexible two-port acoustic wave-based sensor based on PVDF and CNTs as nanofillers is successfully fabricated through a novel microdispensing DDM process. The developed sensor device exhibits increased piezoelectric properties along with flexibility, thereby extending its application range to include curvilinear aerospace structures. Moreover, it is found

that adding CNTs as fillers has a significant impact, producing a maximum of 43 pC/N after polarization. IDT dimensions are designed and evaluated through selected FEM tools, including sensor performance with S-parameter and eigen frequency analysis, and are additively manufactured with desired quality.

Although fine IDT lines are achieved, eventually the width of the IDT needs to be reduced to increase the operational frequency (which is challenging to achieve with the selected process). This necessitates the use of a micro scale high resolution 3D printing technique. Also, when exposed to environment over time, the electrode gets damaged in some cases, which can be avoided if the electrode pattern is embedded inside the substrate. Conceptually, it is essential to study the sensor performance with electrode placed inside the substrate to validate this approach. Given the development of the sensor is a multi-step process, it is beneficial to analyze it using a numerical tool before experimental steps. The next section will explore different IDT configurations to study the numerical study in both time and frequency domains.

5 Numerical Study on IDT Location Optimization

This section will explore the numerical analysis study focused on finding the optimal location of electrodes that exhibit better sensitivity toward aimed measurements.

5.1 Background and Overview

Modeling and optimization play a major role in developing susceptible and portable devices before production by offering a substantial benefit in reducing time and money. IDT design and location are directly related to the effectiveness of the wave propagation. However, a better interpretation of wave characteristics and design methodology has not yet been examined to understand the underlying Multiphysics [128, 129]. In this work, a highly advanced 2PP process is selected, which allows extremely high-resolution parts in micro- and nano-scales [130, 131]. This process is employed to sputter coat the pattern onto the substrate with ease by utilizing the fine-made stencil. The wave-based piezoelectric sensor made of PVDF and featuring various electrode configurations, including surface mounted or embedded inside the substrate, is examined to study the sensor's generated wave characteristics and effectiveness through numerical, theoretical, and experimental analysis. Compared to the IDT electrodes deposited on the surface, studies demonstrate an enhancement of electrocoupling coefficient (k^2) [132] by embedding the electrodes in the substrate, where the IDTs will be protected from the external damage with effective wave generation, expanding the range of applications to have a completely embedded sensor in the desired structures. To guide the exploration in electrode location optimization, the following research questions will direct the investigation: a) what are the effects of electrode configuration on the overall effectiveness of wave generation in piezoelectric sensors and b) what is the effective way to validate the IDT location for maximizing wave propagation efficiency? Based on these questions, the following hypotheses are proposed: a) embedding the electrode inside the substrate will enhance the electrocoupling coefficient and improve wave generation

effectiveness compared to surface-mounted configurations and b) integration of numerical simulations and theoretical models will optimize the IDT location, leading to improved efficiency.

5.2 Numerical and Theoretical Modeling of the Acoustic Wave-based Sensors

The primary goal of the acoustic sensor is to be highly sensitive with low loss to the strain concentration that occurs in aerospace structures. To validate the sensor's performance with different electrode configurations, wave characteristics are examined using a numerical tool in the time domain (voltage response and wave patterns) and frequency domain (scattering parameter). The obtained frequency response is then validated using the theoretical model.

5.2.1 Numerical Study

Computer-aided simulation, such as the finite element method (FEM), helps efficiently design the piezoelectric sensor to study the characteristics owing to its easy way of analyzing complicated geometries. In this study, all the simulations are based on PVDF substrate, employed with commercially available finite element analysis, COMSOL Multiphysics 6.0 package, including two physics of solid mechanics and electrostatics following the piezoelectric equations, as shown in equations 2.1 and 2.2. Among other FEM tools, the COMSOL model is more reliable by including the piezoelectric effect and its dependence on the external impact, such as strain on a real scale with exact material properties. The essential properties to be specified for piezoelectric materials are compliance matrix [s], electrical permittivity [ε], and density [ρ]. Additionally, poling direction plays a vital role in the piezoelectric material in COMSOL, which is set to the z-axis by default.

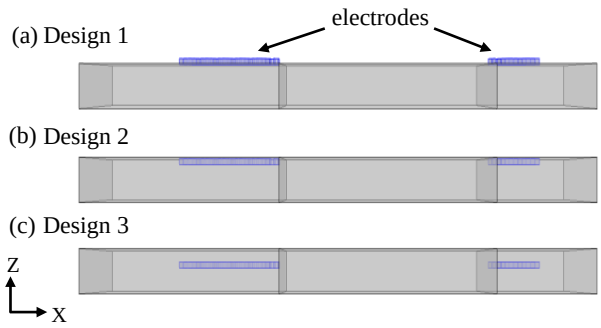

Figure 5.1 Different sensor configuration (a) Design 1, IDTs on surface, (b) Design 2, IDTs embedded immediate to surface, and (c) Design 3, IDTs embedded three times the thickness below the surface.

A 3D model with three different positions of electrodes along the thickness direction, as shown in Figure 5.1, is studied in both time and frequency domains. The boundary conditions used during the simulation include a fixed constraint on the bottom surface and low-reflective boundary conditions at the side walls to avoid border reflections. For the IDTs, an electrode pattern made of gold with 200μm wavelength maintaining a 50% metallization ratio, λ/4 width of 50 μm and thickness of 50 μm with 850 μm aperture, is designed and placed in different places along the thickness direction (design 1: on the surface, design 2: embedded immediately below the surface and design 3: three times the thickness of electrode below the surface). Overall, the model with IDTs and substrate is meshed using a tetrahedral element with a size of λ/8 and λ/4, respectively.

Table 5.1 Material properties used in numerical simulation of different IDT designs explored in this study.

Description	**Value**
Polyvinylidene fluoride (PVDF)	
Density ρ, kg/m^3	1780

Young's modulus (E), GPa	3
Poisson's ratio *v*	0.3
Elastic compliance matrix, 10^{-10}. Pa^{-1}	s_{11} = 3.781 s_{12} = -1.482 s_{13} = -1.724 s_{33} = 10.92 s_{44} = 14.28 s_{66} = 11.1
Permittivity matrix	ε_{11} = 7.4 ε_{22} = 9.3 ε_{33} = 7.6
Electromechanical coupling factor k^2	0.14
Gold (Au)	
Density ρ, kg/m^3	19300
Young's modulus (E), GPa	70
Poisson's ratio *v*	0.44

Table 5.1 lists the required material properties assigned to the substrate and electrodes from the COMSOL library. The numerical simulation studies are executed at two levels - time and frequency domain analysis.

5.2.2 Frequency Domain Analysis

A frequency domain analysis is studied to calculate the scattering parameter (S_{21}), which displays how much signal exists within a specific band at a given range of frequencies. The

terminal feature is used in COMSOL to evaluate the frequency-based S-parameter. The terminated type connects the aimed terminal to a characteristics impedance that represents the wave transmission from input to output IDTs. Input power of 0.01 W is given to the sensor based on the power used in VNA for the experimental measurement, whose input power is 10 dBm. The S-parameter is measured in terms of insertion loss (IL), representing the power loss that occurs when the signal travels through the transmission system. The obtained frequency peak information shown in Figure 5.2 for different designs is mentioned in Table 5.2. An increase in insertion loss is observed with each design's distinct frequency peak information respective to the wave characteristics. Embedding the electrode completely below the substrate still exhibits an evident resonant peak that can be utilized as a sensor with acoustic wave propagation. This frequency study will stand out as a reference point for further analysis to dictate the performance of the sensor before fabrication.

Table 5.2 Center frequency peak information for different IDT desings.

Configuration	**Center frequency, MHz**	**Insertion loss, dB**
Design 1	3.81	116
Design 2	3.85	125
Design 3	4.00	137

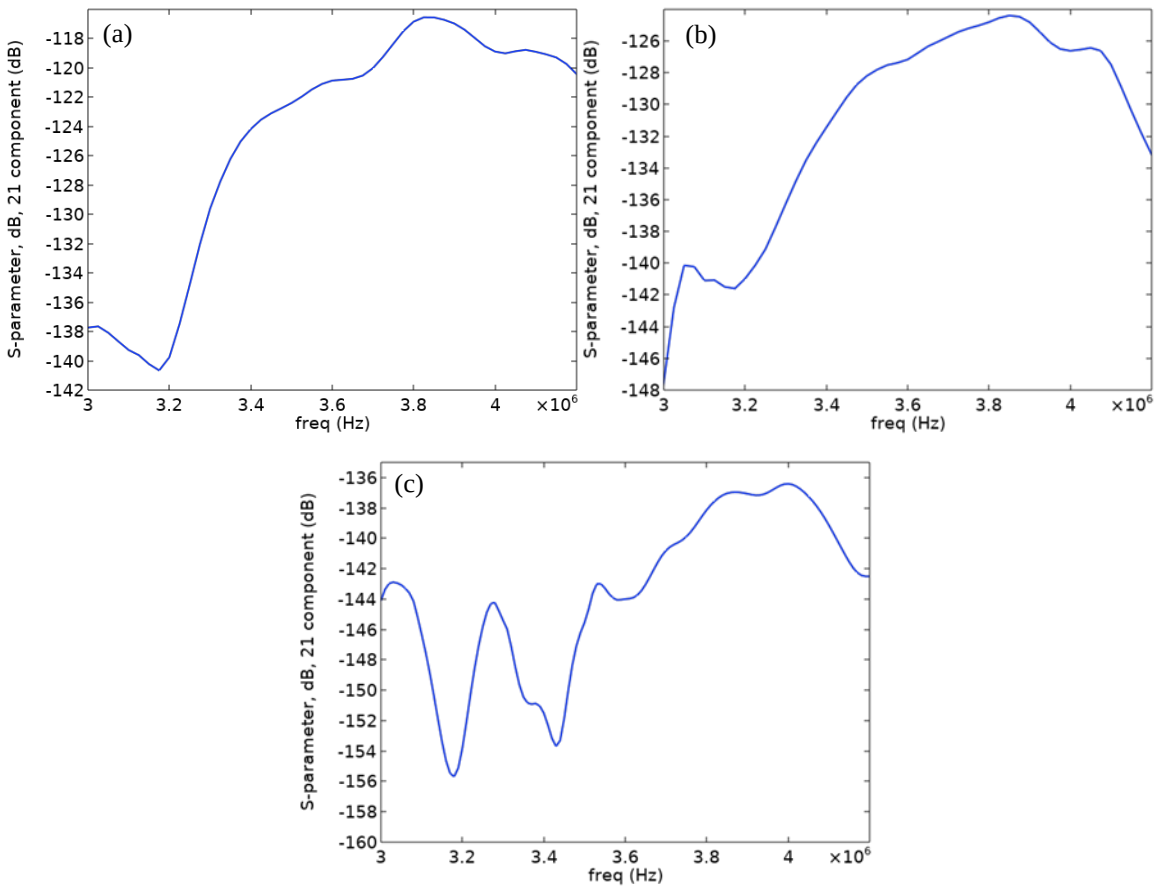

Figure 5.2 Frequency domain S_{21} response (a) Design 1, (b) Design 2, and (c) Design 3.

5.2.3 Time Domain Analysis:

A time domain analysis is studied to evaluate the change in input signal over time. Transient analysis of PVDF based sensor model, with an input sinusoidal signal of 3.8 MHz and magnitude of 1 V lasting 18 cycles (~4.75µs), is executed. This signal is applied to positive electrodes in the input IDT where the negative side is grounded. While running the transient analysis with a short pulse excitation, different wave modes that are generated will be separated after traveling a certain distance due to their velocity difference. Due to a large number of wave reflections between the electrodes, a slight fluctuation in the wave is noticed. Positive electrodes in the output IDT receives the mechanical wave and transforms it into a voltage response.

Table 5.3 Time domain analysis information for different IDT designs.

Configuration	**Time delay, μs**	**Output signal amplitude, mV**
Design 1	3.16	0.43
Design 2	3.42	0.18
Design 3	3.63	0.04

It is also noticed that the width of the received wavelength shows consistency with the wavelength of the input signal. The obtained time delay and amplitude of received voltage response information for different designs are shown in Figure 5.3, and values are mentioned in Table 5.3. It is noticed by embedding the electrodes, the amplitude level decreases with an increase in time to reach the output IDTs, as the substrate material surrounds it. The time delay information is collected at a specific wave mode's amplitude, in which velocity is decreased by embedding the electrodes below the surface.

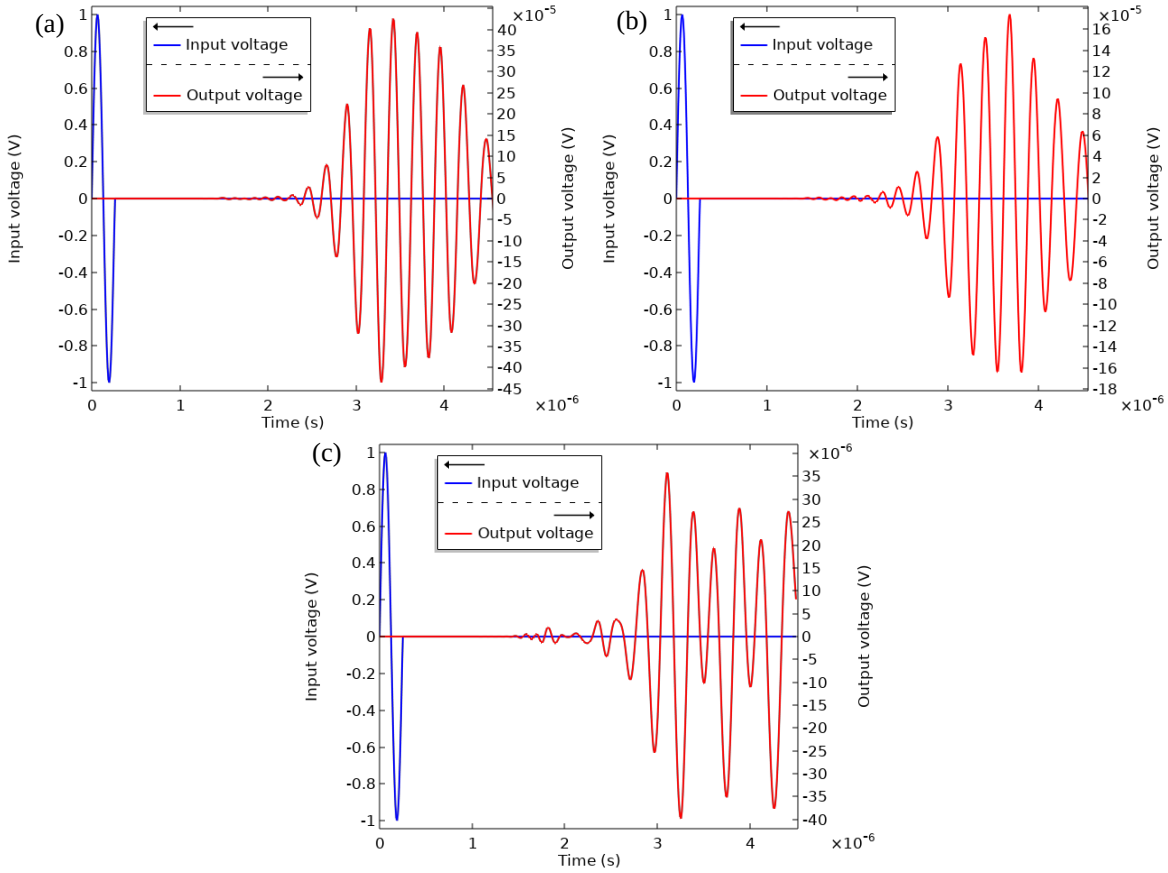

Figure 5.3 Time-domain voltage response collected from output IDT for (a) Design 1, (b) Design 2 and (c) Design 3.

5.2.4 Theoretical Modeling Validation

The coupling of modes (COM) model is a widely accepted theoretical model, among other models such as impulse response, green's function model, and equivalent circuit model [119, 133-135] due to its advantages such as the inclusion of second-order perturbation effects, which makes this model more reliable and accurate to the realistic case. The COM model uses a set of first-order wave equations, propagating in forward and backward modes with an electrical port. The waves are described by r (x, ω) and s (x, ω), representing modes propagating in the positive and negative x-direction.

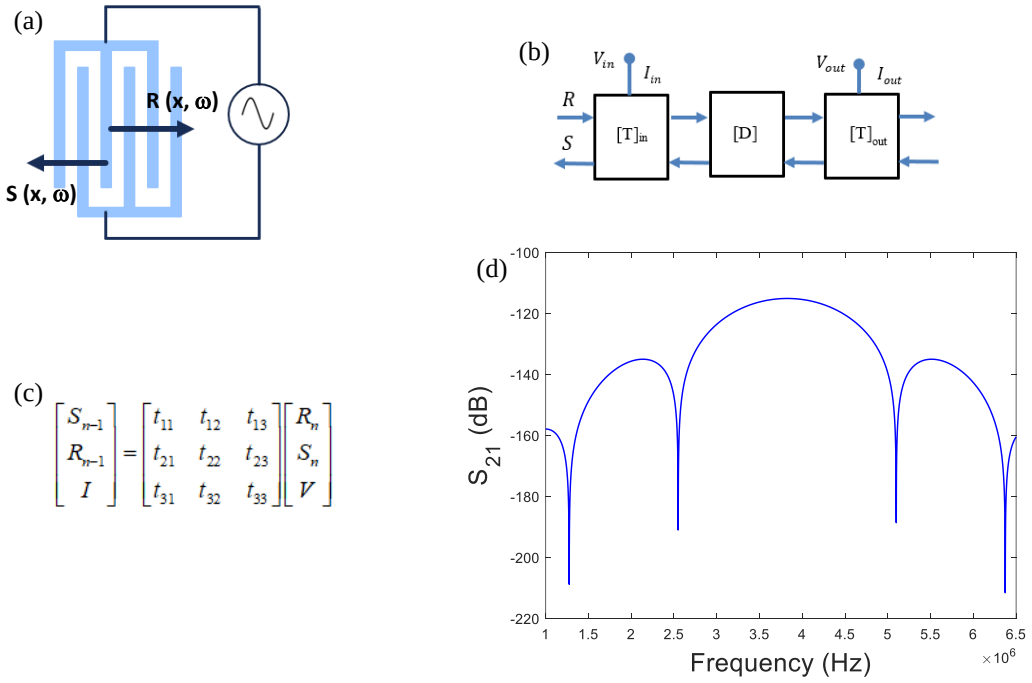

Figure 5.4 (a) Schematic of bi-directional IDTs with forward and backward generated waves, (b) transmission line of a three-component sensor device, (c) modified transmission matrix, and (d) center frequency response of design 1 using COM theoretical model.

These two waves are initially uncoupled and unperturbed before the presence of grating, whose wave equations in the time domain are described as follows,

$$\frac{dR\ (x,\omega)}{dx} = -jk_R(x,\omega)R(x,\omega) \tag{5.1}$$

$$\frac{dS\ (x,\omega)}{dx} = +jk_R(x,\omega)S(x,\omega) \tag{5.2}$$

$$k_R = \frac{2\pi}{\lambda_R} = \frac{\omega}{\vartheta_R(x,\omega)} \tag{5.3}$$

where $\vartheta_R(x,\omega)$ denotes the spatially and frequency-dependent velocity of the Rayleigh wave. The wave propagating through the electrode gratings is frequency-dependent and the first-order wave equation in the frequency domain is derived using the Fourier transform.

A modified transmission matrix based on the COM model is utilized to increase the computational speed of the model, with a major component of metalized, non-metalized, and delay line regions, as shown in Figure 5.4 (a, b, and c). Material properties and IDT dimensions, such as thickness, aperture, and number of input and output finger pairs (same values used in the numerical approach), are given as inputs to the model. The theoretical response with a center frequency of about 3.79 MHz, as shown in Figure 5.4 (d), is obtained with 115 dB insertion loss, which shows an agreement with the center frequency obtained from the numerical model for design 1. Additionally, the numerical model is suitable only for design 1 with surface waves.

5.2.5 Numerical Mechanical Strain Analysis for Different IDT Locations

For the strain analysis, initial strain conditions are applied from no strain to 10,000 με with 2,500 με increments. The strain and ambient phenomena are accounted as the static load, while the input signal is a harmonic load. The root mean squared (RMS) displacement is used to replace the S_{21} parameter based on the numerical tool used. Strain is applied in the longitudinal direction, and from the obtained response, as shown in Figure 5.5, there is an evident frequency shift with an increase in applied strain, which fits the fact that external strain leads to additional loss of signal power.

This change in frequency shifts occurs due to the combination of changes in IDT geometry and acoustic wave velocity, particularly with different designs used in this study. The numerically obtained shift in frequency with corresponding strain values is utilized to plot each design's sensitivity, as shown in Figure 5.6. Comparing different designs, embedding the electrode below the surface shows an increase in sensitivity associated with wave velocity and frequency response. A maximum sensitivity of 0.47 ppm/με is obtained in design 3, which significantly supports the embedding concept in this study.

$$f_s = \frac{\Delta f}{f} = \frac{f' - f_0}{f_0} \times 10^6 \; ppm \tag{5.4}$$

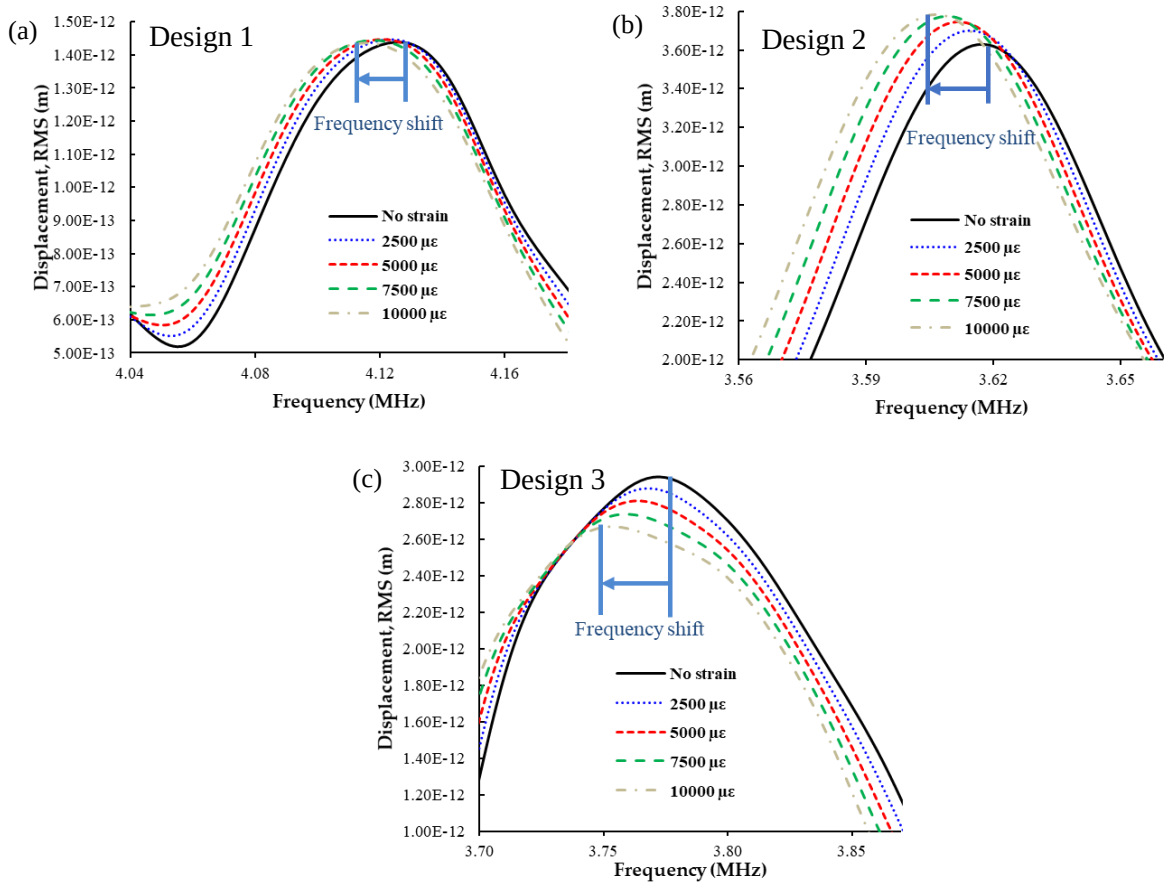

Figure 5.5 Numerical strain analysis showing a shift in resonant frequency peak with applied longitudinal strain for (a) Design 1, (b) Design 2, and (c) Design 3.

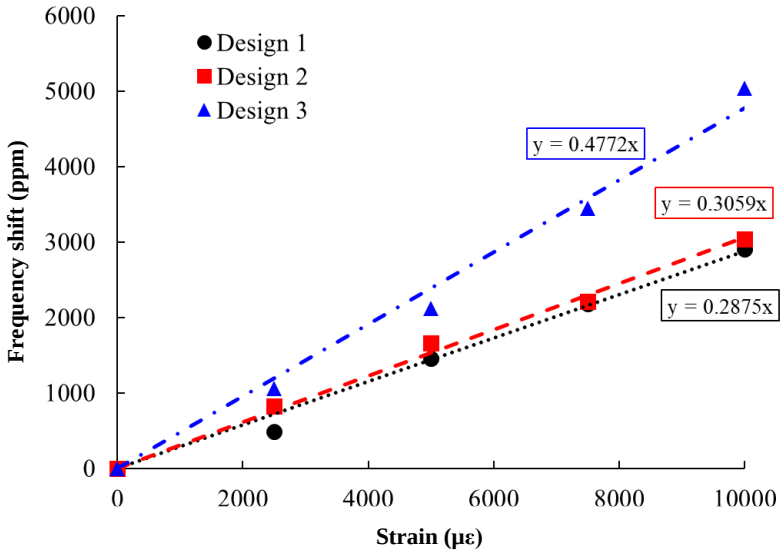

Figure 5.6 Resonant peak frequency shift vs. strain values for the wave-based sensor.

5.3 Experimental Work on Design 1

A PVDF transparent film (PolyK Technologies, PA, USA, P056) is used as a piezoelectric substrate to deposit electrodes for experimental validation. The PVDF substrate's material properties, such as piezoelectric strain coefficient (d_{33}) of 23 pC/N and Young's modulus of 1.2 GPa, are measured using a piezometer (YE2730A) and a universal testing machine AMETEK CS225 (Berwyn, PA, USA). For electrode deposition, a stencil made of negative photoresist (IP-Q) with an IDT pattern is designed using the exact dimensions used in the numerical model and developed using a two-photon polymerization-based GT2 printer (Photonic Professional GT2, Nanoscribe GmBH Karlsruhe, Germany) equipped with a 780 nm femtosecond laser and a 0.3 numerical aperture (NA) lens.

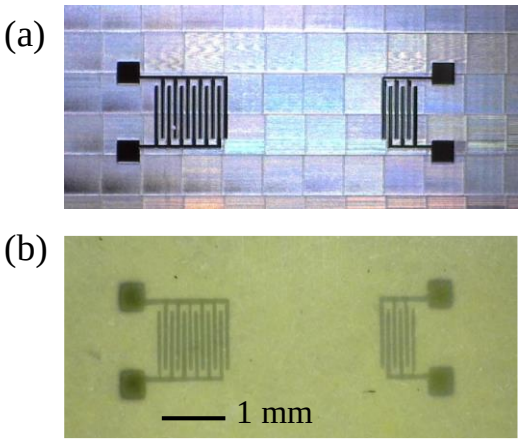

Figure 5.7 (a) 2PP printed stencil and (b) Gold sputtered IDT surface type electrodes.

The printer parameters used to print the stencil are 4 µm slicing distance, 1 µm hatching distance, 100 mm/scan, and 90% laser power on a 2" silicon wafer. The stencil is removed using a sharp razor blade after heating on a hot plate at 100°C for 10 seconds. The gold sputtering technique is used to deposit the electrode on the substrate with the stencil placed on top, which acts as a mask where the electrode material is transferred onto the PVDF substrate, except in areas made impermeable to the gold by a blocking mesh. Figure 5.7 (a) and (b) show the 2PP printed stencil and electrode pattern through the gold sputtering technique without discontinuity.

5.4 Summary and Conclusion

Through the implementation of the selected 2PP printed stencil concept, we have achieved a significant refinement in the fabrication of IDTs, leading to a finer electrode pattern. This section discussed the importance of the numerical, theoretical model, and fabrication procedure of acoustic wave-based piezoelectric sensors based on PVDF polymer substrate and gold electrodes. The change in wave characteristics of the sensor with different electrode configurations is studied in both time and frequency domains and is validated using a COM theoretical model. Simulation results clearly indicate that embedding the electrodes into the substrate not only enhances the

applied longitudinal mechanical strain sensitivity but also provides crucial protection against possible environmental factors. Among different designs, the embedded electrode concept (design 3) shows a higher sensitivity of 0.47 ppm/με to the applied mechanical strains, despite the degradation in signal amplitude. This successful numerical validation serves as a solid foundation before proceeding with the experimental exploration of design 2, which involves the embedded electrode concept using the reverse replication process – an approach detailed in a subsequent section. An important takeaway from these previous endeavors is the remarkable capability of 2PP to achieve micro-scale resolution in IDT patterns. These key insights represent a significant summary derived from the findings in this section's approach.

6 Half-embedded Reverse Replication Process

This chapter focuses on the development of piezoelectric sensors, emphasizing the piezocomposite substrate and IDT fabrication using AM and a simple screen-printing process. It delves into the creation of sensors with half-embedded electrodes via the reverse replication process. To guide this exploration, the following research question is posed: how does the integration of advanced fabrication technique enhance the production specific to half-embedded electrode (Design 2) process? The hypothesis suggests that the integration of advanced methods such as 2PP master mold with IDT impressions and screen printing for filling embedded electrodes will lead to improved fabrication efficiency and enhanced performance towards applied mechanical strains.

6.1 Approach

This section presents a novel reverse replication technique of piezoelectric substrate, as shown in Figure 6.1, which exhibits enhanced piezoelectric properties with embedded electrodes (Design 2) capable of detecting mechanical strains.

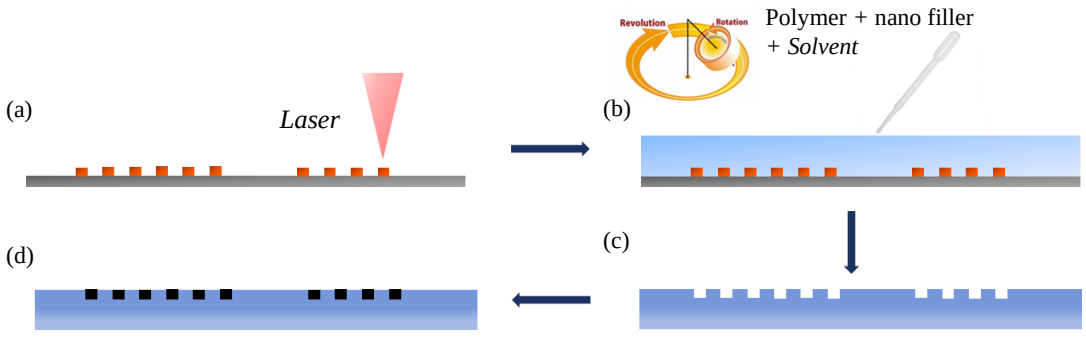

Figure 6.1 Reverse replication process of a piezoelectric substrate with embedded electrodes (a) 2PP printing of master mold, (b) positive mold made of polymer-nanofiller composite, (c) positive mold after peeling off, and (d) conductive electrode deposition.

6.2 Master Mold using 2PP

A master mold with IDT design is developed on a 2-inch silicon wafer to replicate the piezoelectric sensor with empty electrode channels. The IDT master mold made of high viscous negative photoresist (IP-Q, Nanoscribe, Karlsruhe, Germany) is printed using a 2PP printer (Photonic Professional GT2, Nanoscribe GmBH, Karlsruhe, Germany) equipped with a 780 nm femtosecond laser. IP-Q resin and the 0.3 numerical aperture lens are utilized for increasing the voxel size with quicker modeling of the structured IDT master mold.

Table 6.1 IDT master mold dimensions used in 2PP printing.

Parameters	**Dimension**
Finger width (Free space width), μm	125
Metallized ratio (η)	0.5
Wavelength (λ), μm	500
No. of input (output) finger pair	3 (2)
Acoustic aperture, μm	850
Depth of IDTs, μm	300
Delay line distance, μm	1000
Bus bar width, μm	150

After cleaning the silicon wafer using acetone and isopropanol, the wafer is activated with an oxygen plasma etch PE-50HF system (Plasma Etch, Caron City, USA) at a pressure of 149.8 mTorr, a flow rate of 20 cc/min, and a radio frequency (RF) power of 20 W for 40 seconds. The printer parameters used are 4 μm slicing distance, 1μm hatching distance, 100 mm/scan, and 90% laser power. The printed master mold is developed for 20 min in propylene glycol monomethyl

ether acetate (PGMEA) (Merck kGaA, Darmstadt, Germany), developed for 5 min in isopropanol, and dry-blown with compressed air. Master mold dimensions printed using a 2PP printer are mentioned in Table 6.1.

6.3 Piezoelectric Substrate Development Procedure

To develop a flexible piezoelectric composite, PVDF-TrFE incorporated with BTO particles is fabricated through a novel replication process. Primary materials selected for the piezoelectric composites are listed below,

- PVDF-TrFE powder 80/20 mol (PolyK, State College, PA, USA), a density of 1.88 g/mL and Curie temperature of 135 °C.
- $BaTiO_3$ (BTO) 99.5% purity (TPL Inc., Albuquerque, NM, USA), near-spherical particles with an average diameter of 420 nm, a specific surface area of 4 m^2/g, and a density of 6 g/cm^3.
- DMSO (Sigma-Aldrich, St. Louis, MO, USA), Mw ~78.13 g/mol.

PVDF-TrFE polymer is dissolved in polar solvent dimethyl sulfoxide (DMSO) due to the polymer insolubility in water using a planetary THINKY mixer (Laguna Hills, CA, USA) for 12 min at 2000 rpm. The dissolved base polymer PVDF-TrFE is then mixed with different wt. % proportions (40% and 60 %) of the BTO ceramic particles. Particles are well mixed with the base polymer in both rotational and revolution axed motion without bubbles due to the deaeration capability of the mixing technique used. The mixture is then poured into a custom-made 0.63 cm thick acrylic mold, where the 2PP printed master mold is placed tight, as shown in Figure 6.2 (a). After room temperature curing, the positive mold is peeled off from the master mold with empty channels to be filled with the conductive electrode material. Figures 6.2 (b) and (c) show the

positive mold with DMSO evaporated forming composite substrate maintaining structural integrity and master mold after peeling off with few particles stuck to it, respectively.

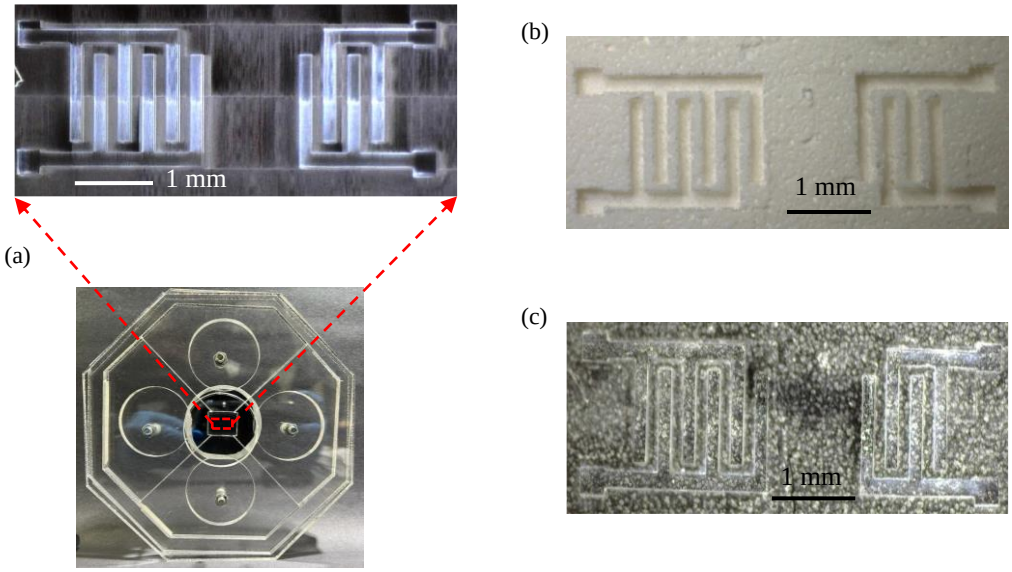

Figure 6.2 (a) Master mold placed in the acrylic mold where the mixed material is poured in for curing, (b) Piezoelectric positive mold peeled off after curing with electrode channels, and (c) Master mold after peeling.

6.4 Surface Morphology of the Developed Substrate with Nanofillers

To investigate the nanofiller distribution in the polymer matrix, the fabricated substrate is examined using a scanning electron microscope. For better conductivity, samples are sputtered with gold, and images are captured at 10 kV with a 4.0 spot size. As shown in Figure 6.3, pure PVDF-TrFE along with 40 wt. % and 60 wt. % of BTO are analyzed. Pure PVDF-TrFE resembles a foamy texture with pores and is overly soft. Composite combination with 40 wt. % exhibits flexibility with less stiffness and pores, making it unsuitable for electrode deposition. In 60 wt. % combination, BTO particles have well adhered with less porosity and uniform dispersion, suitable for embedding electrodes with sturdiness. BTO particle with an average particle size of 420 nm is

observed through particle size distribution analysis based on 382 particles, as shown in Figure 6.3 (c).

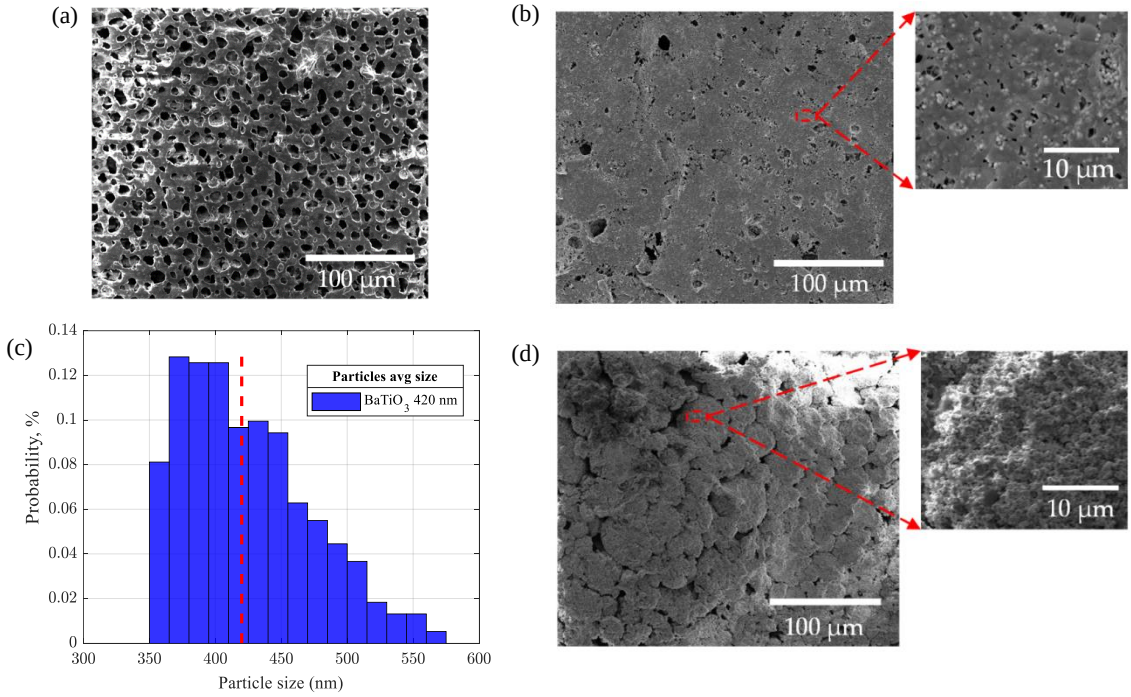

Figure 6.3 SEM images (a) PVDF-TrFE, (b) PVDF-TrFE with 40% BTO, (c) BTO particle distribution, and (d) PVDF-TrFE with 60 BTO.

6.5 Piezoelectric and Mechanical Property Study of the Developed Nanocomposite

The conversion of the non-polar phase to an active phase is carried out by applying a high voltage of 8 kV through a non-contact poling process, which enhances the piezoelectric property by aligning the dipoles towards the electric field direction. A maximum d_{33} value of 36.5 pC/N is achieved in a composite with 60 wt. % BTO, with an 8.5% increase after polarization. A compression test is performed using a universal testing machine AMETEK CS225 (Berwyn, PA, USA) with a 10 kg load cell at a 1 mm/min extension rate. When comparing pure PVDF-TrFE with 40 and 60 wt. % BTO combinations, an increase in stiffness is observed as the particle loading

increases. A maximum Young's modulus of 1.26 MPa is obtained with 60 wt. % BTO maintaining stiffness and pliability. Measured piezoelectric strain coefficients, with crystalline phase information are listed in Table 6.2 and stress vs. strain plot is shown in Figure 6.4.

Table 6.2 Piezoelectric strain coefficients measured for different piezoelectric composite types before and after polarization.

Material	**d_{33}, pC/N**		**F (β), %**
	Unpolarized	**Polarized**	
PVDF-TrFE	21.5	23.8	73.1
PVDF-TrFE/ 40 wt. % BTO	28	29.3	75.9
PVDF-TrFE/ 60 wt. % BTO	33.7	36.5	78.5

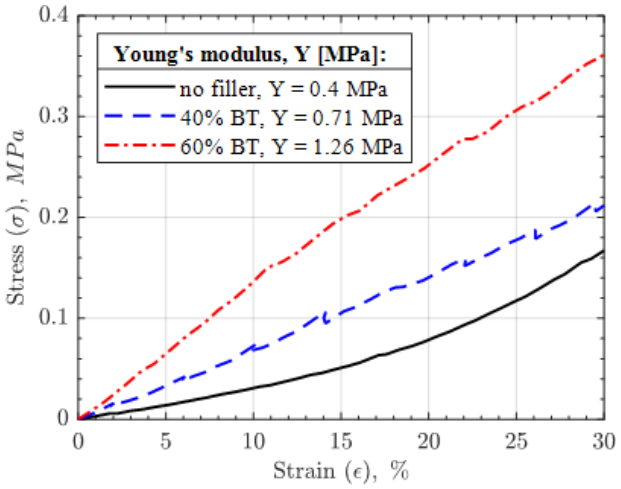

Figure 6.4 Young's modulus measured for different piezoelectric composite types.

FTIR spectroscopy using an Agilent ATR FTIR is executed to quantitatively analyze the presence of the crystalline phase, which dominates the piezoelectricity of PVDF-TrFE polymer [136]. Infrared spectra in a wavenumber range of 750-1550 cm^{-1} are obtained using an Agilent

spectrometer. Figure 6.5 shows absorption peaks at 763 cm^{-1} and 952 cm^{-1} representing non-polar α phase, while peaks at 841 cm^{-1} (CF_2 symmetric stretching), 1172 cm^{-1} and 1280 cm^{-1} (CF_2 symmetric stretching), originate due to β phase presence. Additionally, the peak at 1401 cm^{-1} is due to CH_2 wagging vibration. The peaks at 880 cm^{-1} and 1172 cm^{-1} correspond to the a-axis, 841 cm^{-1} and 1280 cm^{-1} peaks indicate the polar b-axis and 1401 cm^{-1} peak is associated with the c-axis of the polymer chains [137-139]. As listed in Table 6.2, it is evident that adding nanofillers increases the β phase with d_{33} enhancement, and a maximum polar phase of 78.5 % is achieved with 60 wt.% BT fillers.

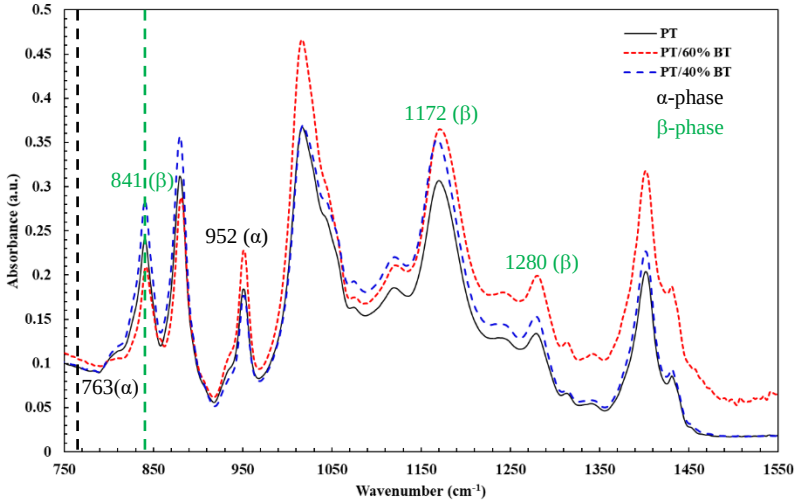

Figure 6.5 FTIR absorbance spectra for PVDF-TrFE (PT) polymer with 40% and 60% BT.

6.6 IDT Electrode Deposition based on Screen Printing

A screen-printing technique is used to deposit the conductive material (filling the empty channel in the positive mold with electrodes). A stencil with an IDT pattern is designed and developed using a 2PP printer, which acts as a mask where the conductive material is transferred onto the positive mold, except in areas made impermeable to the ink by a blocking mesh. The

printing parameters used for developing a stencil are the same as the master mold printing. Figures 6.6 (a) and (b) show the CAD model of a stencil with IDT pattern and 2PP printed stencil. The electrodes are made of conductive poly(3,4-ethylenedioxythiophene)-poly(styrenesulfonate) (PEDOT: PSS) 5% screen printable ink (Sigma-Aldrich, St. Louis, MO, USA). IDT pattern made of conductive PEDOT: PSS ink is screen printed without discontinuity with a minor spread of ink due to the foamy nature of PVDF-TrFE and is well bonded to the base substrate, as shown in Figure 6.6 (c). Figure 6.6 (d) shows the stencil condition after screen printing and cleaned using water, which can be reused.

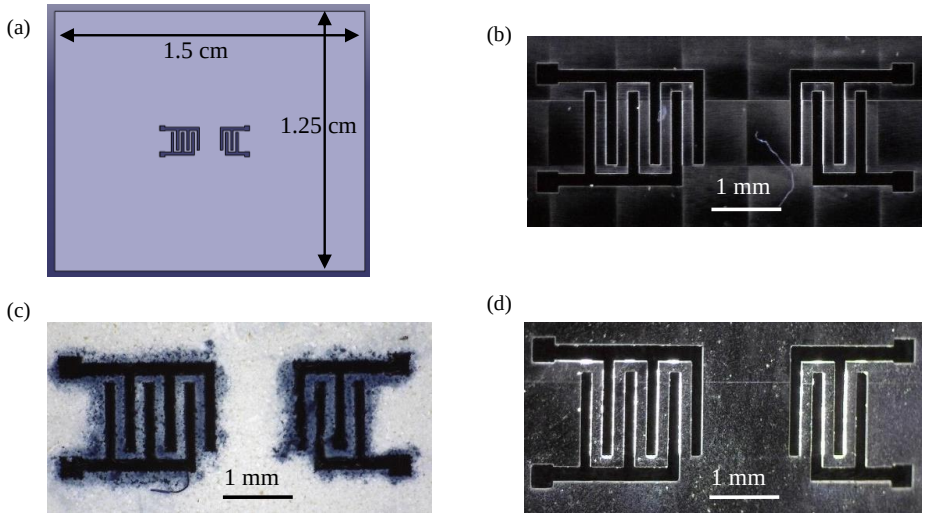

Figure 6.6 (a) CAD model of stencil with empty IDT pattern; (b) 2PP printed stencil; (c) electrode channel filled with conductive material and (d) stencil after electrode filling.

6.7 Summary and Conclusion

In summary, this chapter presents the successful development of a piezoelectric acoustic sensor based on PVDF-TrFE and BTO nanofillers with surface-embedded electrodes. The sensor fabrication utilized a novel reverse replication process employing a 2PP printed master mold and

stencil pattern. The impact of nanofiller addition to the polymer matrix is investigated through surface morphology, chemical characterization, mechanical, and piezoelectric property measurement. Notably, PVDF-TrFE with 60 wt.% BTO achieved a maximum piezoelectric strain coefficient (d_{33}) of 36.5 pC/N, accompanied by a 78.5% active crystalline phase.

Although design 2 with embedded electrodes has been achieved, researchers should exercise caution when selecting the material that needs to be reverse replicated, particularly regarding the porosity, as this method purely relies on room temperature curing without the application of external temperature. Additionally, dense electrode material, such as liquid metal or high conductive paste, can also be a great candidate, as selected PEDOT: PSS tends to thin out over time along with solvent evaporation. This suggested method is also suitable for the electrode spacing range between 10-50 μm.

7 Sensor Signal Response of Developed Sensors

This chapter will showcase the measured S_{21} parameter response for different electrode location cases with the reasoning and summary behind the shift in fundamental frequency response.

7.1 Microdispensing Surface IDTs

Frequency analysis is carried through a Hioki IM3570 impedance analyzer under the Butterworth-Van Dyke (BVD) model approach to examine the strain detection capability of the fabricated SAW device [127]. The impedance analyzer leads are made in contact with the sensor IDT terminals attached to a flat and 30° curved steel surface, as shown in Figure 7.1 (a). Sensor performance under flat and bent conditions is investigated by tracking the resonance peak in a frequency range from 500 kHz to 5 MHz, which provides useful information in detecting mechanical strains that occur in the host structure. Impedance (Z) and admittance (Y) responses of the developed PVDF and PVDF/CNTs sensor attached to a flat and 30° angle host structure is represented in Figure 7.1 (b) through (d), and each sensor demonstrates a unique resonant peak response respective to substrate properties. It is noticed that when strain occurs in the host structure, there is an evident shift in frequency and peak intensity proportional to the change in propagated wave characteristics, which substantiates the strain detection capability of the developed sensor. A frequency shift from 3.88 MHz to 3.97 MHz for PVDF and 4.01 MHz to 3.93 MHz for PVDF/CNTs sensor is observed. It is also noticed that the frequency response obtained from the sensor contains some additional parasitic effects that occurred due to the cabling and reference impedance of the measurement setup, which skewed the resonant peak.

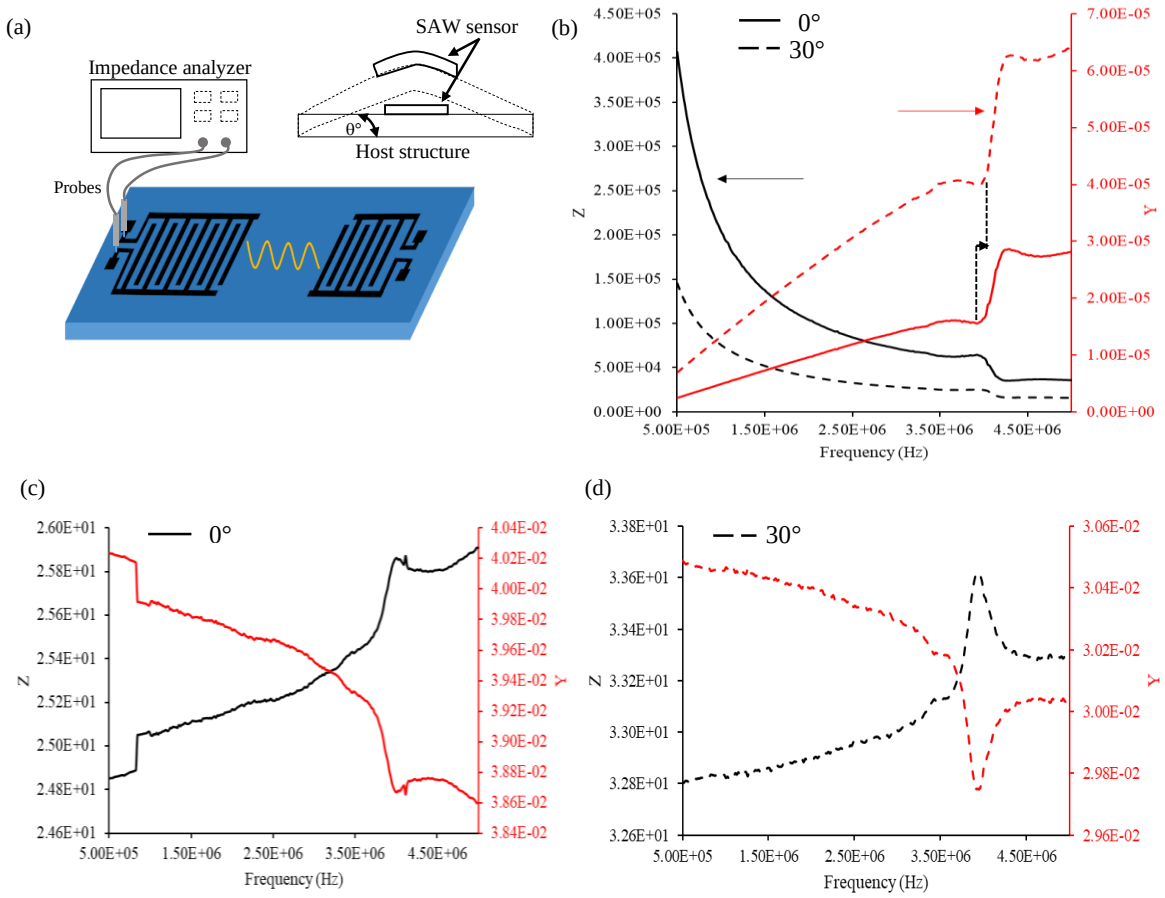

Figure 7.1 (a) Measurement test setup with SAW sensor attached to host structure at an angle θ°; (b) Impedance (Z)/ admittance (Y) response of PVDF sensor; impedance (Z)/ admittance response of PVDF/CNTs sensor at an angle (c) 0° and (d) 30°.

7.2 Surface Electrode with 2PP Stencil Concept

Digital image correlation (DIC), an optical strain measurement technique, is performed to show quantitative displacement that occurred in the Y-direction. The area under the sensor, as shown in Figure 7.2, especially the region under the IDT and delay line, is selected as a region of interest. Figure 7.2 (b) shows the averaged strain concentration values under a designated area with different bent angles.

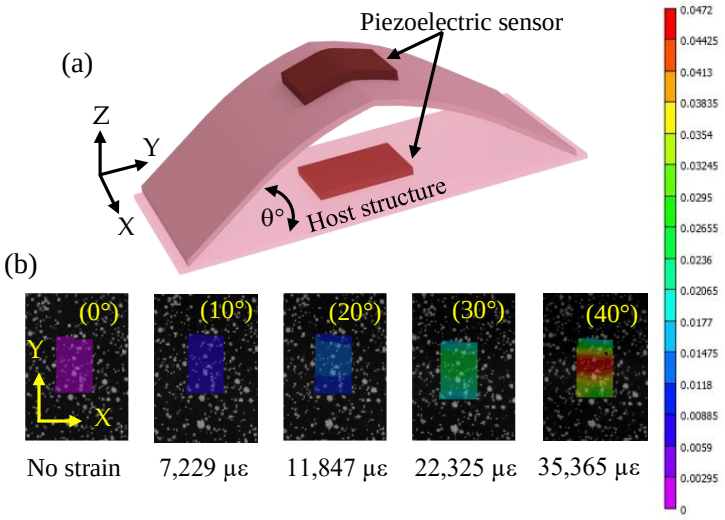

Figure 7.2 (a) VNA and DIC setup with a piezoelectric sensor attached to the host structure bent at angle θ° and (b) DIC images of displacement in Y direction with an average strain measured in the selected area.

The electro-acoustic frequency response behavior of the sensor (design 1) is studied using a Keysight N5227B vector network analyzer and two (ECP 18-GSG-1250-DP) probes. The sensor response at flat and different bent angles, as shown in Figure 7.2 (a), is measured in a frequency range from 44 MHz to 54 MHz, where the resonance peak provides information about the strain that occurred in the host structure. An evident shift in frequency peak is obtained, as shown in Figure 7.3, which validates the strain detection capability of the developed sensor. Due to the cabling effect and impedance mismatch, the center frequency peak is not detected, which needs to be investigated further along with sensitivity analysis.

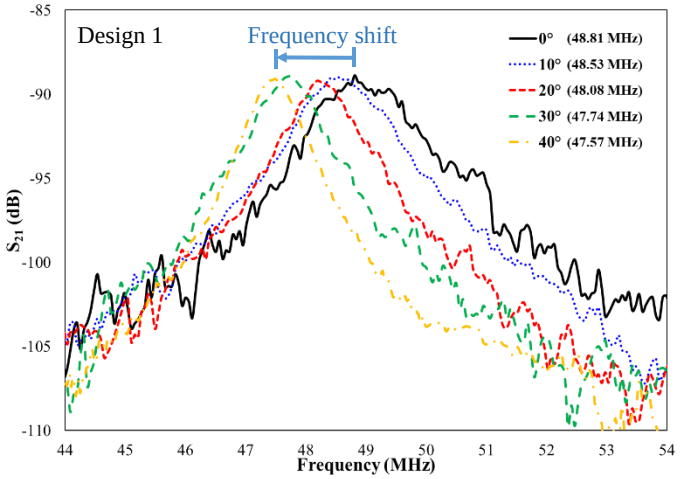

Figure 7.3 Scattering parameter response of piezoelectric sensor showing the frequency shift corresponding to different bent angles.

7.3 Sensor Response for Half-embedded Electrode Using Screen Printing

Frequency response analysis is carried out using a spectrum vector analyzer (Siglent SVA 1032X) to evaluate the strain detection capability of the fabricated piezoelectric sensor with embedded electrodes. The network analyzer GGB probes (ECP 18-GSG-1250-DP) are connected to the IDT terminals of the sensor attached to a flat and 30° curved steel surface (host structure), as shown in Figure 7.4 (c). The probes are calibrated using a CS-10 calibration substrate, and sensor response is measured in the frequency range from 80 MHz to 130 MHz, providing information on mechanical strains that occurred in the host structure. A 10 dBm RF signal is provided as an input to the sensor with a reference impedance of 50 Ω to analyze the scattering parameter (S_{21}). The frequency response depends on the IDT pattern, electromagnetics of the material, and the velocity of the acoustic wave generated. The S_{21} response of the developed sensor measured at a flat and angled condition is represented in Figures 7.4 (a) and (b).

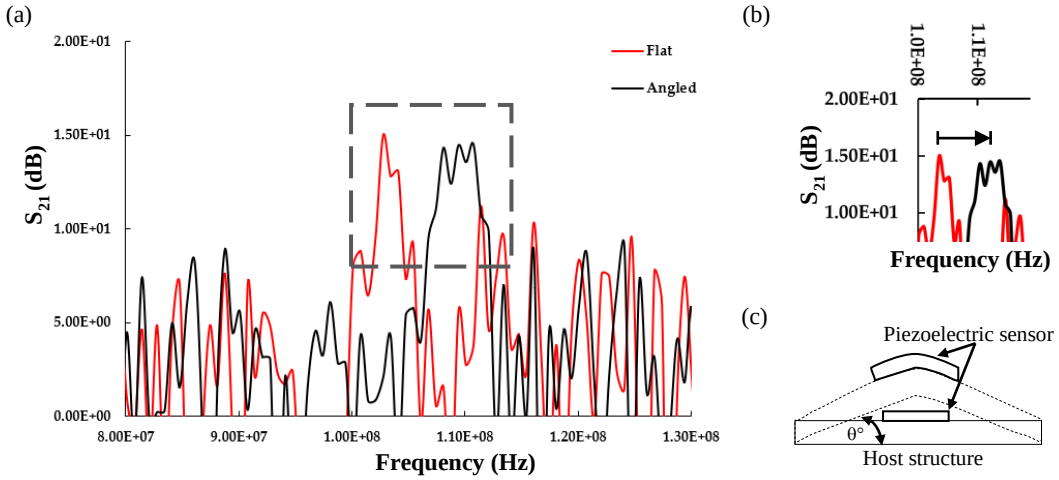

Figure 7.4 (a) Frequency response of piezoelectric sensor measured in both flat and bent (30°) condition; (b) zoomed-in response shows the frequency shift details and (c) strain validation setup with a sensor attached to host structure at an angle θ°.

When a strain occurs in the host structure, there is a perceptible frequency shift and peak intensity relational to the change in wave characteristics, which validates the strain detection capability of the developed piezoelectric sensor. A harmonic frequency shift is detected from 103 MHz to 109 MHz for the PVDF-TrFE/BTO sensor with higher piezoelectric and mechanical properties. Some parasitic effects are noticed due to electromagnetic coupling in probe setup and impedance mismatch, which leads to missing fundamental peak detection.

7.4 Summary and Conclusion

It is imperative to address the hurdles encountered when utilizing the VNA and impedance analyzer for measuring S-parameters and impedance values, particularly concerning cabling issues, impedance mismatch, and limitations in the high-frequency range. Cabling issues, such as signal loss, reflections, and electromagnetic interference, can significantly impact the accuracy of measurements. These issues arise due to the inherent properties of the transmission lines used to connect the VNA to the DUT. As signals propagate through the cables, they experience losses due

to resistance, capacitance, and inductance, leading to attenuated signals and distorted measurements. Moreover, reflections at cable terminations and discontinuities can cause signal echoes, interfering with the original measurement signal and introducing possible errors.

Impedance mismatch between the measurement setup and the DUT is another critical factor influencing measurement accuracy. When the impedance of the measurement system does not match that of the device being tested, signal reflections occur at the interface between the two, resulting in inaccurate impedance measurements. This phenomenon is particularly pronounced in RF and microwave systems, where precise impedance matching is essential for accurate signal transmission and measurement. Furthermore, while VNAs are powerful instruments for a high and wide range of frequency sweep measurements, they may not be accurate for sensors operating in the lower MHz range. At higher frequencies, noise levels in the measurement system increase, potentially overshadowing the weaker signals generated by the developed sensor. This noise can arise from various sources, including amplifier noise and environmental interference. As a result, the signal-to-noise ratio (SNR) decreases, making it challenging to discern the true signal from the noise floor.

Addressing these challenges requires careful consideration of the measurement setup, including cable routing and termination, impedance matching techniques, and noise reduction strategies. Additionally, calibration procedures, such as open-short-load (OSL) calibration and through-reflect-line (TRL) calibration, can help mitigate errors introduced by cabling and impedance mismatch. By understanding and addressing these challenges, one can ensure the accuracy and reliability of RF measurements.

In summary, despite the initial challenge of not detecting the fundamental resonant peak, strain detection relied solely on the frequency shift, which was validated as the n^{th} mode of the resonant

peak, one such example is shown in Figure 7.5. Therefore, tracking the peak achieved using the VNA setup is deemed sufficient to validate the mechanical strain detection capability. However, it is advisable to utilize a low-frequency VNA to mitigate noise below 10 MHz and enhance the signal strength, even though the sensor response might be slightly weaker.

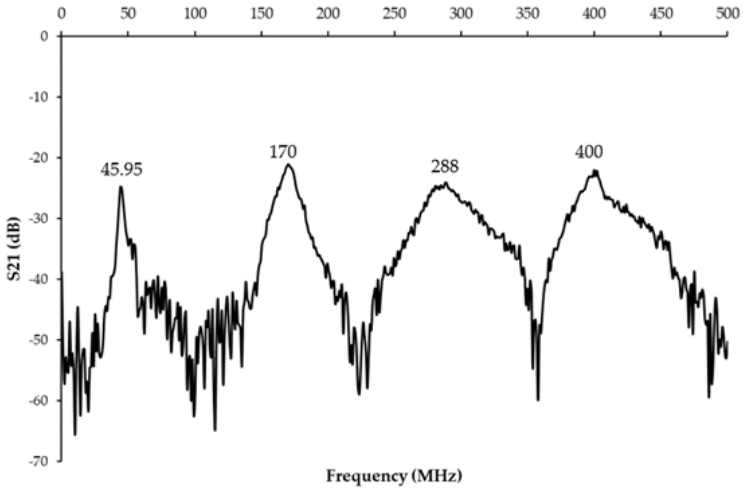

Figure 7.5 Representative frequency plot showcasing multiple modes of harmonic peaks.

In this research, employing a VNA with a low-frequency sweep range and implementing noise filtering after baseline correction, we were able to reveal the fundamental frequency peak. However, it is noteworthy that the signal strength of this peak was relatively low compared to the noise level and harmonic peak observed with other VNAs. Despite this challenge, the careful selection of equipment and application of noise reduction techniques enabled the identification of the fundamental frequency peak, contributing to the validation of our strain detection methodology.

So far, the investigation has focused on developing substrate materials for acoustic wave-based sensors and designing and fabricating IDTs using various AM techniques. Efforts have primarily

centered on exploring materials that enhance piezoelectric properties while ensuring printability using AM methods. Furthermore, the focus shifts towards investigating different IDT designs, integral components of wave-based sensors, to enhance sensitivity in mechanical strain detection across larger or focused areas, as detailed in Chapter 8.

On the other hand, the experimental procedures involved in developing Design 3, which entails sensors with electrodes embedded completely within the structure, posed significant challenges. Initially, attempts were made to employ a vacuum technique for electrode embedding. However, due to the porous nature of the polymer materials, such as PVDF and its co-polymer PVDF-TrFE, and the room temperature curing process, the substrate proved unable to withstand the electrode pattern, as it remained soft. This issue may not persist with samples cured using temperature or UV processes, prompting our focus on developing materials suitable for UV-based AM techniques, as discussed in Chapter 9.

8 Numerical Modeling of IDT Layout Optimization

This chapter will examine the other integral component of the developed sensor: IDT, which is responsible for converting input signals into mechanical waves or vice versa on the other end of the sensing layout.

8.1 Background and Overview

To date, different IDT layouts have been explored for multidisciplinary projects [140-145], however, a better interpretation of sensor behavior exhibiting different IDT layouts embedded inside the substrate (Design 3 in Chapter 5) has not yet been explored to understand the efficiency towards the mechanical strain sensitivity. This work aims to investigate the performance of two-port piezoelectric sensors with different embedded layouts. The numerical analysis includes scattering parameters and voltage response in frequency and time domains. Compared to surface-deposited IDTs, embedding the electrode demonstrates an enhancement in sensitivity due to the higher piezoelectric coupling [132, 146, 147], which also protects the IDT structure from the external environment. The sensitivity of each IDT layout towards mechanical strains is quantified using an initial strain model with varying mechanical strain concentrations. Based on the considerations, it is hypothesized that the performance of two-port piezoelectric sensors, in specific to IDT layout selection can be decided with sensitivity, coupling (k^2), and quality factor (Q) values. Among different layouts, circular design will demonstrate higher sensitivity and offer superior sensing capability over larger areas with multi-axial sensing. Additionally, the embedded electrode layouts will outperform conventional bi-directional designs due to improved piezoelectric coupling and environmental protection.

Based on the investigated results, a high-performance sensor with a unique IDT design can be developed by combining the benefits of each type through advanced AM techniques that expand the range of applications. The primary goal of the acoustic sensor with embedded electrodes is to

be sensitive to the applied mechanical strain exhibiting better coupling and figure of merits. The effectiveness of each layout type is decided based on the sensitivity, k^2, and Q. To validate the piezoelectric sensor's performance with different IDT layouts embedded inside the substrate, the sensor behavior, particularly the scattering parameter and output voltage response, is analyzed in both frequency and time domains [148].

The electrode design must be properly constructed to provide optimal sensor performance because several parameters predict the wave characteristics, such as wavelength, layout type, and delay line. IDT layouts such as focused, circular, and slanted designs are modeled for input IDTs, as shown in Figure 8.1 (b-g), to examine their performance with electrodes embedded inside the substrate. Output electrodes are fabricated of a bi-directional design, which receives the propagated acoustic waves. Focused IDT (FIDT) patterns on acoustic sensors are used mainly to generate waves with high intensity at a focused point. Their performance depends on the degree of arc, focal length, and spacing between IDTs. Among these, the frequency response is not affected by the change in focal length [140], and operating frequency can be dictated based on the electrode spacing. The degree of arc has a crucial influence on the generated waves' focusing characteristics and is essential to identify the optimal degree of arc correlated towards device sensitivity through simulated data [144]. In this work, FIDT performance with 30°, 45°, and 60° arcs with a 1.25 mm focal length is designed, simulated, and compared. Furthermore, circular IDT designs with electrodes next to each other (spiral) and a holographic style are designed and simulated. The circular layout has the potential to generate waves in a larger area of the piezoelectric substrate and can be extended in multi-axial sensing. Lastly, the slanted type features a varying finger spacing across the electrode's length, enabling the sensor to operate in a wide frequency range [149]. All the layouts are designed with a 2.5 mm delay line (distance between

input and output electrodes), 50 µm spacing, 6 input pairs, 3 output pairs, and a 0.5 metallization ratio.

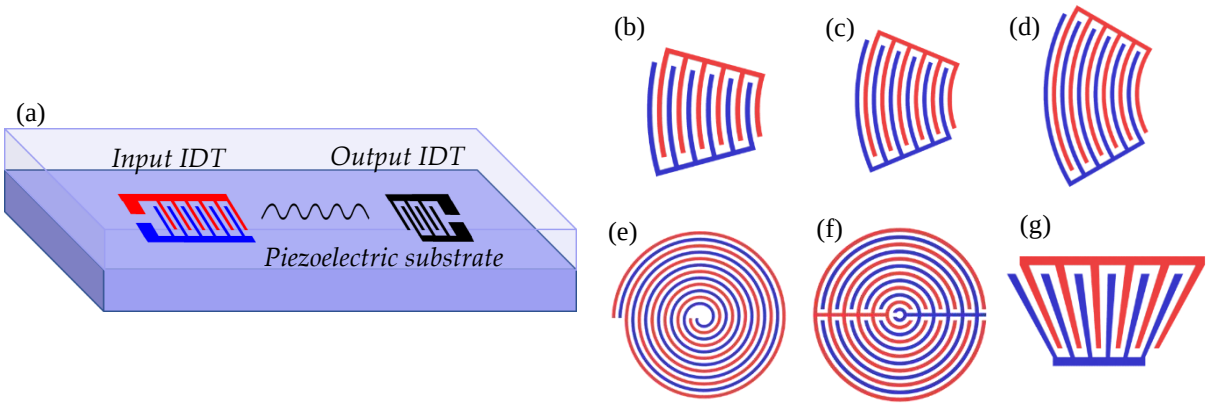

Figure 8.1 (a) Schematic representation of a two-port piezoelectric sensor with electrodes embedded in the middle of the substrate (the upper half of the substrate is made transparent to show the electrode location); different IDT layouts studied in this work – FIDTs degree of arc (b) 30°, (c) 45°, (d) 60°; circular pattern (e) spiral, (f) holographic; and (g) slanted.

8.2 Frequency and Time Domain Analysis

A frequency domain analysis is studied to simulate the scattering parameter (S_{21}), which indicates the operational frequency of the specific design as a function of frequency. The terminated terminal feature is utilized in COMSOL to evaluate the S-parameter represented in dB with a reference 50 Ω impedance [150]. Based on the experimental VNA measurement, the input electrode receives an input power of 10 mW, equivalent to 10 dBm.

The obtained response for each layout case is measured in dB, representing the magnitude of power loss on the signal traveling between the input and output electrodes. Figure 8.2 (a-f) shows the distinct response for each electrode type, and for a slanted type, the frequency peak response for 100 µm is displayed among multiple resonant peaks.

To study the amplitude of voltage response from the output electrode, the time domain is executed using a transient analysis with an input sinusoidal response at the resonant frequency and a magnitude of 1V lasting 18 cycles (time depends on the resonant frequency of each layout). The voltage signal is applied to the input IDT using the voltage terminal feature to evaluate the voltage response as a function of time. Different wave modes are generated with the input voltage and will be separated after traveling a specified distance due to the traveling velocity difference. The voltage amplitude is obtained from the output positive for a specific wave mode, which converts the received mechanical waves into a voltage response. The scattering parameter and output signal response are summarized in Table 8.1.

Table 8.1 Summary of sensor's frequency and time-domain analysis with different embedded IDT layouts.

IDT layouts	**Type/ spacing**	**Frequency peak, MHz**	**IL, dB**	**Output signal, µV**
Focused	30°	3.96	-134	39.7
	45°	4.14	-140	43.2
	60°	3.8	-136	41.8
Circular	Spiral	3.92	-139	43.4
	Holographic	3.65	-141	26.9
Slanted	50~100 µm	4.18/1.54	-154/-139	52.7/10.5
Bi-directional	-	3.96	-135	38.7

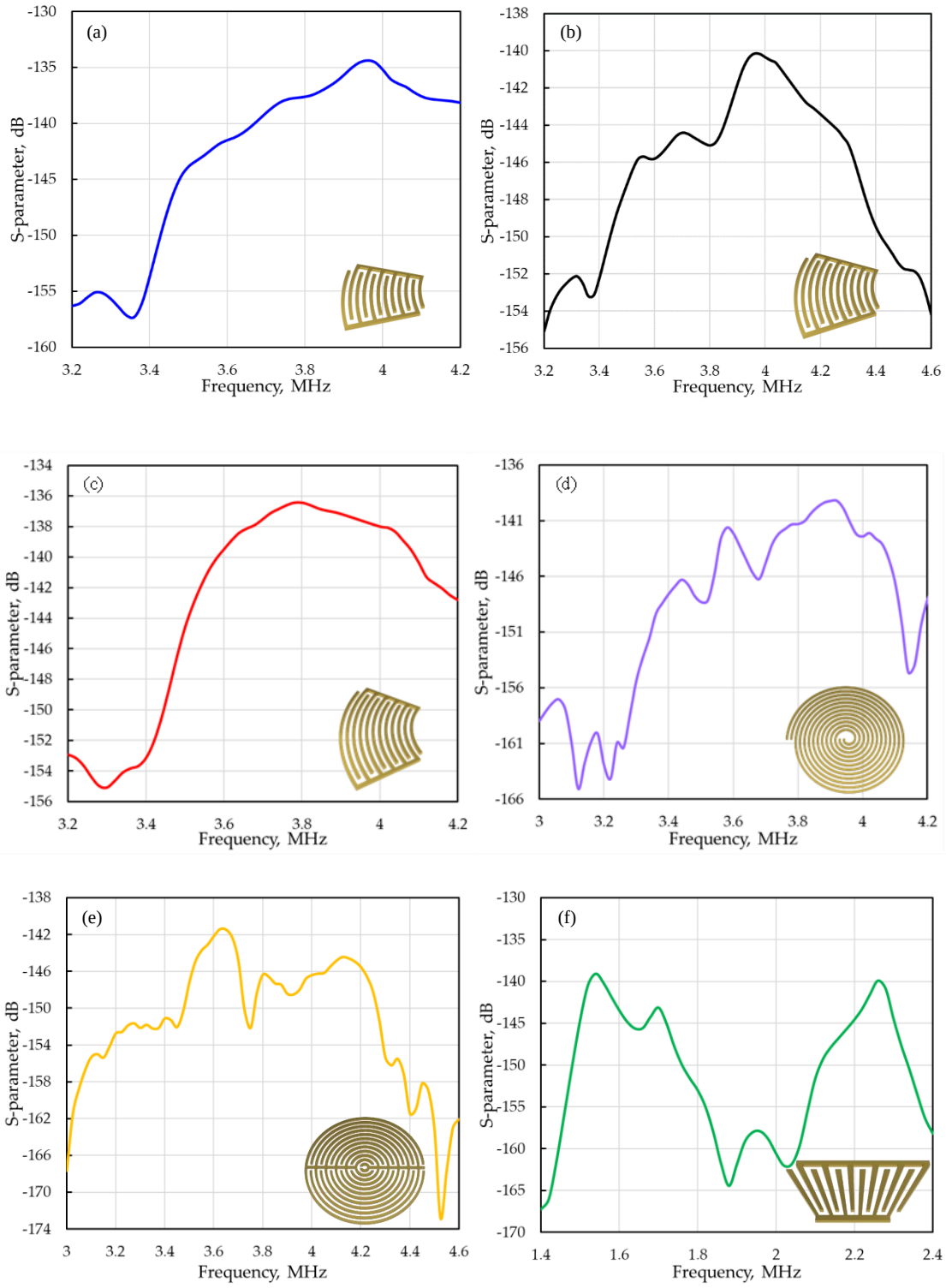

Figure 8.2 Scattering parameter response as a function of frequency of different IDT layouts: FIDTs degree of arc (a) 30°, (b) 45°, (c) 60°; circular pattern (d) spiral, (e) holographic; and (f) slanted with 100 µm spacing.

Among the different layouts, FIDT with 45° degree of arc and spiral showcases a higher output signal along with better scattering characteristics. In general, too large or small degree of arc shows an unfocused or unstable response [151], which supports the response attained through the simulation for FIDT layout. The slanted design shows a range of resonant peaks desirable for a wide frequency operation and is still the same as the bi-directional design, where the waves are dispersed based on slant angle. The slanted type's maximum and minimum response value is included for comparison. Overall, the optimal layout selection process requires a balanced combination of device performance, which includes sensitivity towards applied mechanical strains and figure of merit calculation based on the extracted data.

8.3 Different IDT Layouts Performance for Applied Mechanical Strains

For the mechanical strain analysis, initial strain conditions are applied on the sensor placed under no strain to 20,000 με with 5,000 με increments. The strain and ambient phenomenon are accounted as static load, while the input voltage signal is a harmonic load. The S-parameter is replaced and represented with root mean squared (RMS) displacements based on the COMSOL numerical tool. Mechanical strain is applied in the longitudinal direction, where an increase in strain value will increase the spacing between the IDTs and wave velocity, resulting in changes in wave characteristics. Figure 8.3 (a-f) indicates the shifts in resonant frequency due to changes in wave velocity and amplitude, which are utilized to execute the sensitivity of each layout towards applied longitudinal mechanical strains. Also, the shift in amplitude is greater with 20,000 με due to the higher strain applied, which can be another indicator of extreme strain monitoring. Among different layouts, FIDT 45° and spiral show higher sensitivity of 0.4311 ppm/με and 0.4478 ppm/με, associated with a change in frequency from the resonant peak, as listed in Table 8.2. A focused layout with 45° will be more suitable for jetting or strain detection applications with higher

amplitude waves at a specific point. Spiral layout utilization can be expanded by adding multiple output ports, which not only increase the area of detection but also enable efficient sensitivity. Overall, these two layouts along with the slanted, will be integrated to form a 3D shape layout that will enable IDT to sense in multiple directions.

Table 8.2 Sensitivity of sensor with different layouts towards mechanical strains.

IDT layouts	**Type/ spacing**	**Mechanical strain sensitivity, ppm/με**
Focused	30°	0.427
	45°	0.431
	60°	0.425
Circular	Spiral	0.447
	Holographic	0.416
Slanted	50 ~100 μm	0.411/0.407
Bi-directional	-	0.260

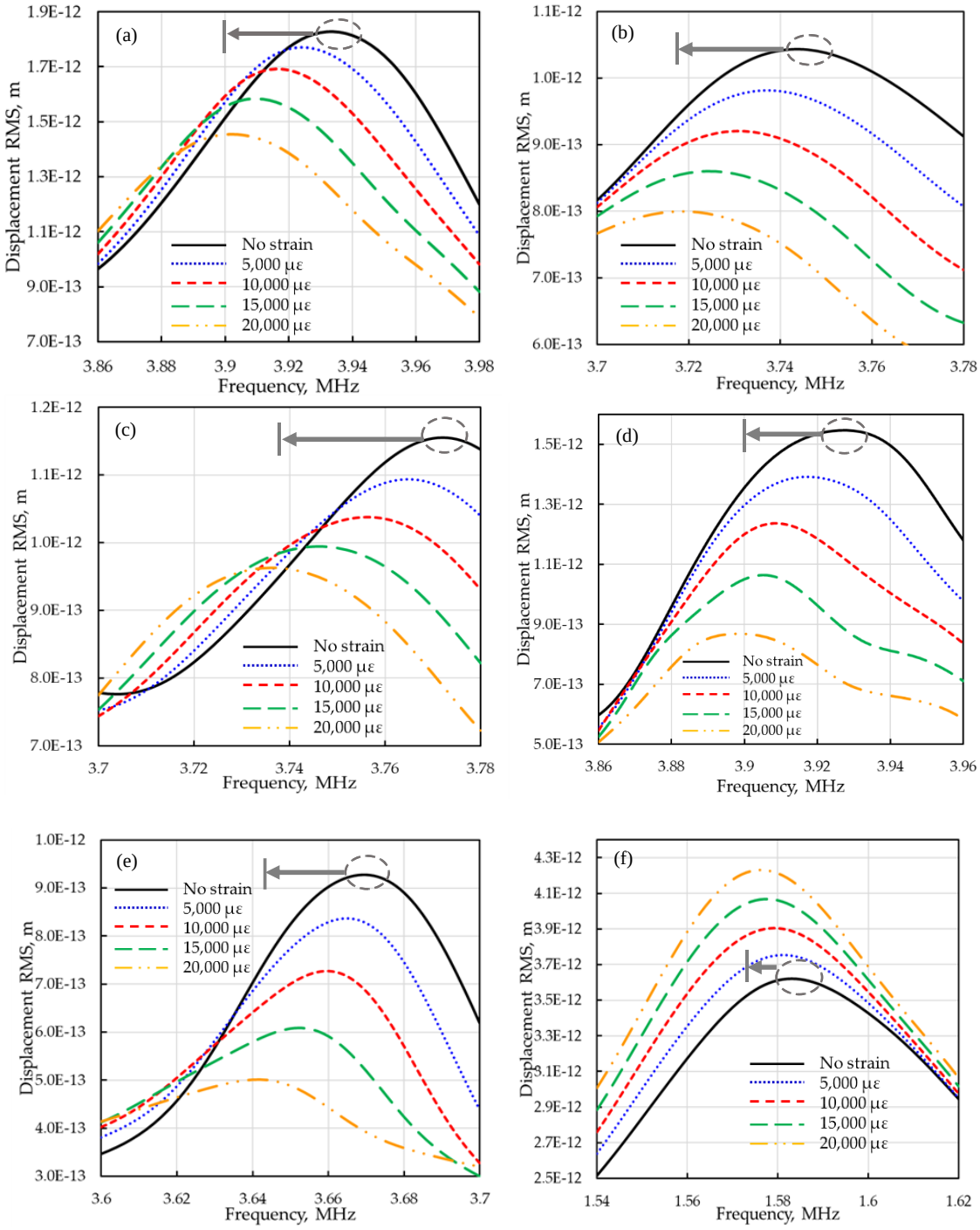

Figure 8.3 Numerical strain analysis showing a shift in resonant peak as a function of mechanical strain for different IDT layouts; FIDTs (a) 30°, (b) 45°, (c) 60°; circular pattern (d) spiral, (e) holographic; and (f) slanted with 100 μm spacing.

8.4 Figure of Merit Study

Examining the figure of merit, which is a combination of the coupling coefficient (k^2) and quality factor in addition to the sensitivity, would be ideal in the IDT layout selection process, as the electrodes are embedded inside the substrate [152]. The k^2 indicates a piezoelectric material's effectiveness in converting an electrical signal into a mechanical wave and vice versa. The quality factor is a dimensionless parameter representing the rate of energy loss relative to the sensor's stored energy. Both the factors are combined as a figure of merit and are calculated based on the expression [153], which involves resonance (f_r) and anti-resonance (f_a) frequency peak from the impedance response derived from S-parameter, as shown in equations 8.1 and 8.2,

$$k^2\ (\%) = \frac{\pi}{2}\left(\frac{f_r}{f_a}\right)\tan\left[\frac{\pi}{2}\left(\frac{f_a - f_r}{f_a}\right)\right] * 100 \tag{8.1}$$

$$Q = \left|\frac{f_0}{f_a - f_r}\right| \tag{8.2}$$

By comparing the simulation data, as listed in Table 8.3, it is evident that FIDT with 45° degree of arc indicates higher FOM along with sensitivity.

Table 8.3 Figure of merit comparison between different IDT layouts.

IDT layouts	**Type/ spacing**	**k^2 (%)**	**Quality factor (Q)**	**FOM (Q × k^2)**
Focused	30°	10.84	24.75	2.683
	45°	13.70	20	2.740
	60°	8.32	31.67	2.633
Circular	Spiral	8.04	32.67	2.628
	Holographic	15.17	18.25	2.769
Slanted	50~100 µm	27.36/ 3.65	11/ 69.67	3.01/ 2.54

However, to expand layout selection into multi-axial mechanical strain measurement with higher sensing area, circular shapes would be the best candidate by implementing multiple output electrodes that can be integrated all together into an antenna. Additionally, a piezoelectric sensor with different electrode layouts embedded inside shows overall better performance than a conventional bi-directional design and can be implemented in respective fields based on the application.

8.5 Summary and Conclusion

This work presents the investigation of wave-based piezoelectric sensor performance with different electrode layouts. The wave characteristics with different embedded electrode layouts are studied in both time and frequency domains. Among the different layouts, focused design with 45° degree of arc and spiral design shows a higher sensitivity of 0.431 ppm/με and 0.4478 ppm/με to the mechanical strains, respectively. A FOM is obtained based on the simulated data to illustrate the effectiveness of the layouts, in addition to the sensitivity. Lastly, a circular layout would be an ideal candidate for sensing mechanical strains in a larger area with multiple output ports. In the future, this concept can be further integrated with the IDT design developed for sensing multi-axial mechanical strains that can be printed using high-resolution additive manufacturing techniques.

9 Photocurable Material Suitable for AM Technology

This chapter will cover the development of PVDF resin, suitable for UV curing based 3D printing techniques. It explores the development of capacitive-based pressure sensors and piezoelectric-based force sensors, ultimately leading to the development of wireless strain sensors.

9.1 Background and Overview

So far, traditional methods such as compression molding, spin coating, and solvent casting have been employed for manufacturing piezoelectric composite material [47, 154, 155]. However, these traditional methods are time-consuming, limiting design flexibility, and mostly suitable for large-scale structures with a complex fabrication process that underscores the need for alternative approaches.

In contrast, AM technology presents a promising solution with its layer-by-layer stacking approach, enabling the creation of intricate three-dimensional (3D) structures with unparalleled ease and efficiency. This capability holds immense potential for the fabrication of multifunctional materials with complex geometries, thereby revolutionizing sensors, energy harvesters, and actuator devices [156-159]. Although attempts have been made to 3D print PVDF-based sensing devices using micro-dispensing [160, 161] and fused deposition techniques [162, 163], challenges persist in printing complex out-of-plane patterns, producing uniform filaments and manufacturing an array of sensor materials in a time-efficient manner. Among different AM techniques, ultraviolet (UV)-based 3D printing overcomes the aforementioned fabrication challenges. SLA, a well-known UV-based 3D printing technique, can produce high-quality macro-sized 3D structures. Yet, this method uses a laser beam, which possesses a low printing rate and is not suitable for rapid production [164]. In this study, a liquid crystal display (LCD) based printing method is employed as this is economical and can print an entire layer at once with effective resolution. Despite advancements in printing technology, the availability of resin material amenable to UV-based 3D

printing processes remains a pressing challenge, highlighting the need for developing an optimized material exhibiting flexibility and piezoelectric properties.

In this particular study, boron nitride nanotubes (BNNTs), a promising nanofiller, known for its high thermal and chemical stability, mechanical strength, and good biocompatibility. This nanofiller offers the potential to significantly enhance the piezoelectric properties of polymer composites, making them one of the ideal for highly sensitive force-sensitive applications [165-167]. Although the BNNT's piezoelectric nature has been explored through analytical and simulation studies [168-170], experimental research on incorporating BNNTs into polymer composites, especially for 3D printing smart sensors, remains in the nascent stage.

Addressing the imperative requirements, this work presents a comprehensive investigation into the structural, thermal, rheological, mechanical, and piezoelectric properties of a newly developed sensor resin material based on PVDF. Additionally, the effect of incorporating BNNTs as a nanofiller is examined, focusing on enhancing the nanocomposite's piezoelectric sensor response. Leveraging an LCD 3D printer, the study also investigates the micro-scale printability of the developed sensor material [171]. Additionally, this work also explores the development of a capacitive-based sensor using the newly developed material. This involves embedding electrodes within the infill channels and validating pressure measurements.

9.2 Sample Preparation and Development Procedure

The process of developing a polymer resin involves blending the base polymer with additives that enable UV-curability, suitable for the selected 3D printing process. The primary component of the developed resin was PVDF, a base polymer (Sigma Aldrich, St. Louis, MO, USA), with an average particle size of 3-10 µm, molecular weight (Mw) ~534,000 g/mol and density of 1.74 g/mL. Additionally, hexamethylene glycol diacrylate (HDODA) monomer with a density of 1.01 g/mL, Bisacylphosphine oxides (BAPOs) photoinitiator (Sigma Aldrich, St. Louis, MO, USA),

and Sudan 1 UV absorber (Thermo Fisher Scientific, Waltham, MA, USA) were uniformly mixed with diethyl fumarate (DEF) solvent (Sigma Aldrich, St. Louis, MO, USA). The proportion of the constituents was investigated, varying between 20 and 40% by weight of the base polymer and between 35 and 55% by weight of the monomer, both in steps of 5 wt. % proportionally. The quantities of the UV absorber, photoinitiator, and solvent were fixed at 0.1%, 1.9%, and 23% by weight, respectively. Additionally, 2 wt. % of boron nitride nanotubes (BNNTs) with an assay of over 80% (Sigma Aldrich, St. Louis, MO, USA) were incorporated as received without further purification to develop a nanocomposite, owing to its higher piezoelectricity and fine electric field tunability. To fabricate the piezoelectric resin, PVDF with respective wt. % proportions were mixed using a centrifugal planetary THINKY ARM-310 mixer (Laguna Hills, CA, USA) at 2000 rpm for an average duration of 20 min, ensuring thorough mixing for the selected combinations without any agglomeration or air bubbles. Table 9.1 presents the sample combinations used throughout various tests. The polymer and nanocomposite resin samples contain additives such as monomers, UV absorbers, and photoinitiators.

Table 9.1 Piezoelectric resin preparation compositions without and with nanofillers.

Sample	**Resin, wt. %**	**BNNTs, wt. %**
Polymer resin	100	-
Nanocomposite resin	98	2

The piezoelectric-based sensor was fabricated using the Phrozen Sonic Mini 8K LCD 3D printer, which boasts a resolution of up to 1152 ppi and exceptional stability while printing, as depicted in Figure 9.1. To assess the UV-curing behavior of the developed piezoelectric resin, an

array of square coupons (5 mm x 5 mm x 1 mm) was modeled and sliced using the Phrozen 3D software.

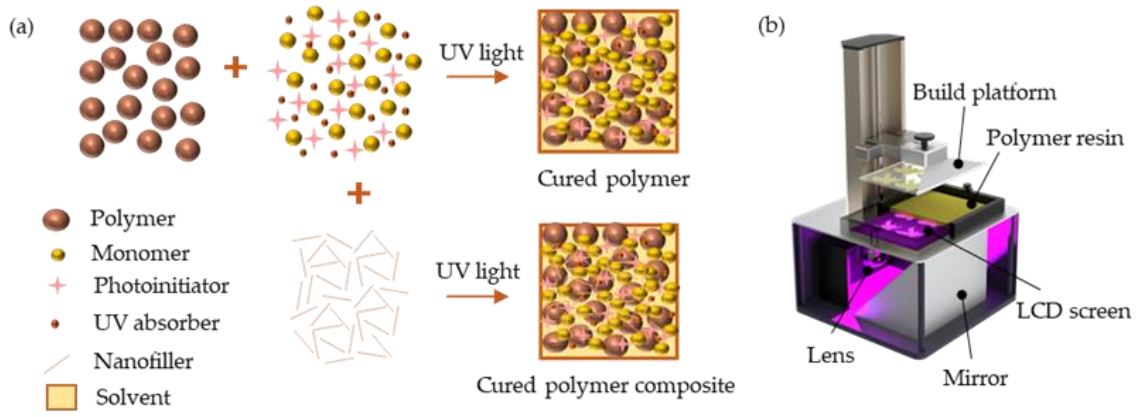

Figure 9.1 (a) Schematic representation for UV curability of polymer dissolved in DEF solvent and (b) LCD 3D printing setup.

Given the customized nature of the developed resin, optimal printing parameters were determined through iterative trials, with a focus on critical factors such as delamination between layers, build platform adhesion, and exposure time for polymerization. Table 9.2 lists the parameters used for printing both the developed polymer and nanocomposite resins. After printing, the coupons underwent 5 min rinse in DEF and then in isopropanol (IPA) to eliminate any residual uncured resin.

Table 9.2 Printing parameters of polymer and nanocomposite resins using an LCD printer.

Print parameter	**Value**
Layer height, mm	0.05
Bottom layer count	6

Normal Exposure time, s	30
Bottom exposure time, s	55
Lift distance, mm	6
Lift speed, mm/min	60
Retract speed, mm/min	150

9.3 Properties of Developed Piezoelectric Resin

In the following pages, the structural, rheological, and thermal properties of the developed resin are presented. Additionally, the mechanical, and piezoelectric properties of the 3D printed sensor material are discussed. Considering better printability and longevity among different polymer combinations, resin with 35 wt. % PVDF was selected for nanofiller addition.

The FTIR spectra analysis of the developed resin with varying polymer content provides information about the crystalline structure, which is crucial for determining the piezoelectric property. Among different polar and non-polar crystallographic phases of PVDF, the β phase is the most essential form due to its excellent piezoelectric behavior. In the polar β phase, the polymer chains exhibit an ordered carbon backbone structure with fluorine and hydrogen atoms on each side, enhancing the material's piezoelectric property. Transmittance peaks at 762 cm^{-1} (CF_2 bending and rocking), 872 cm^{-1} (C-F stretching) and 1062 cm^{-1} (C-C-C bonding) representing the non-polar α-phase, while peaks at 846 cm^{-1} (CF_2 stretching and CH_2 rocking), 1179 cm^{-1} (C-C bonding, monomer's C-O stretching vibration), 1406 cm^{-1} (CH_2 wagging, monomer's C=C)and 1423 cm^{-1} (CH_2 bending) signify the polar β phase presence in PVDF polymer [121, 150, 172, 173], as shown in Figure 9.2 (a). Moreover, peaks at 1636 cm^{-1} (C=C bond), 1719 cm^{-1} (C=O stretching vibration), 2864 cm^{-1} (=C-H stretching vibration), and 2938 cm^{-1} (CH_2 symmetrical) indicate the presence of monomer in the developed polymer resin [174]. Overall, an increment in

the polar peak at 835 cm^{-1} was noticed with an increase in PVDF polymer content, which was validated further by quantifying the polar phase fraction. Furthermore, spectra of the sample containing BNNTs revealed a unique peak at 810 and 1361 cm^{-1} corresponding to in-plane and out-of-plane stretching vibrations of the B-N bond [175], as shown in Figure 9.2 (b).

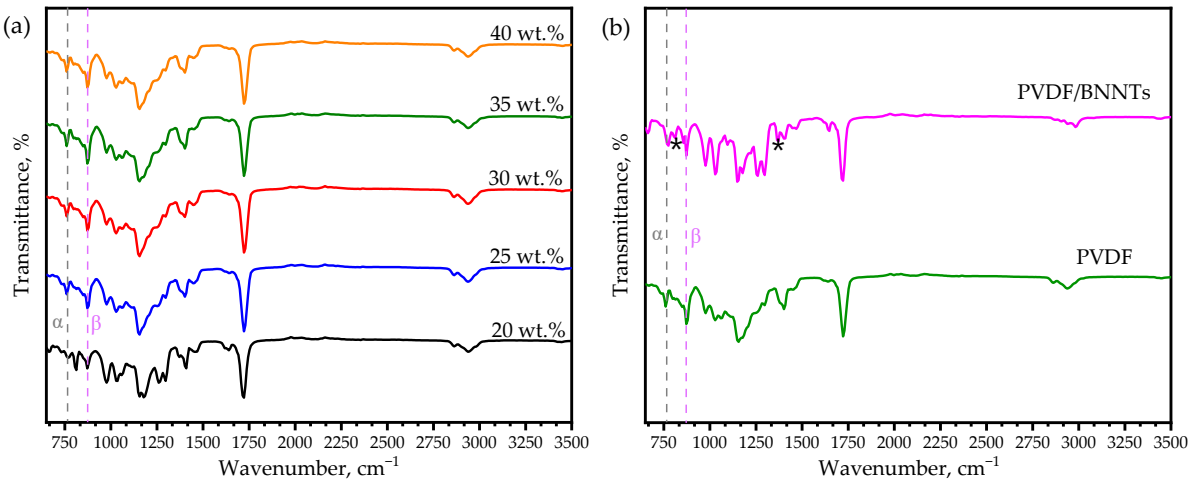

Figure 9.2 FTIR transmittance spectra (a) Resins with different PVDF wt.% and (b) BNNT fillers with 35 wt.% PVDF polymer, with unique peaks marked (*) corresponding to B-N bond.

Based on Beer-Lambert Law, the relative fraction of the beta phase was quantified. The calculated polar phase fraction for different composition types is listed in Table 9.3, with a maximum of 64.89% polar phase achieved with nanofiller addition. The XRD diffraction peaks were analyzed to investigate the crystal phases of the polymer and the impact of the nanofiller on overall crystallization, as shown in Figure 9.3.

Table 9.3 Calculated relative polar phase fraction in developed polymer-based resin.

Sample, wt. %	**F (β), %**
PVDF 20	53.86
PVDF 25	56.08
PVDF 30	57.21
PVDF 35	60.01
PVDF 40	61.08
PVDF 35/ BNNTs 2	64.89

The diffraction peaks at 2θ = 17.8°, 18.4°, 20°, 26.62°, and 38.6°, shown in Figure 3a, were attributed to the diffractions of (100), (020), (110), (021) and (040) crystal planes of PVDF polymer [176, 177], respectively, with an increment in intensity corresponding to high polymer content. Peaks near 26.4° and 44.3° in Figure 9.3 (b) were associated with BN crystal planes, exhibiting a drop in intensity ascribed to the nucleation effect of PVDF crystallization, which was also quantified using thermal analysis [178]. Additionally, an increase in intensity was observed for the 20.5° (110/ 200) polar phase plane, which supported the higher β phase presence with developed resin.

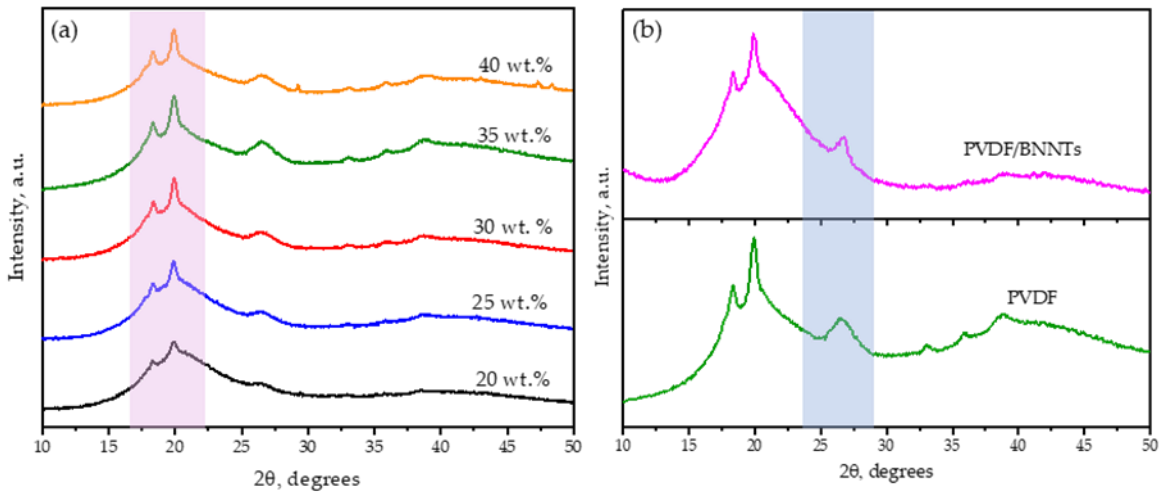

Figure 9.3 XRD diffraction patterns of (a) resins with different PVDF wt.% and (b) different fillers with 35 wt.% PVDF.

The UV-visible absorption spectra of the developed PVDF photo resin is shown in Figure 9.4. The high absorption peak at 420 nm is caused by the initiator, indicating a UV-curable region.

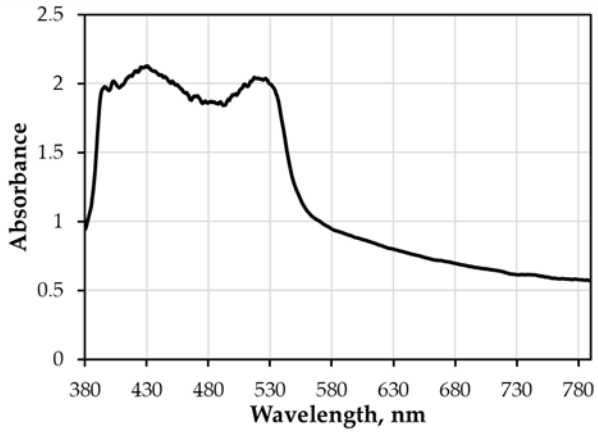

Figure 9.4 UV-visible spectra of developed PVDF resin.

The DSC thermograms depicting samples with an increase in PVDF content and nanofiller addition are displayed in Figure 9.5.

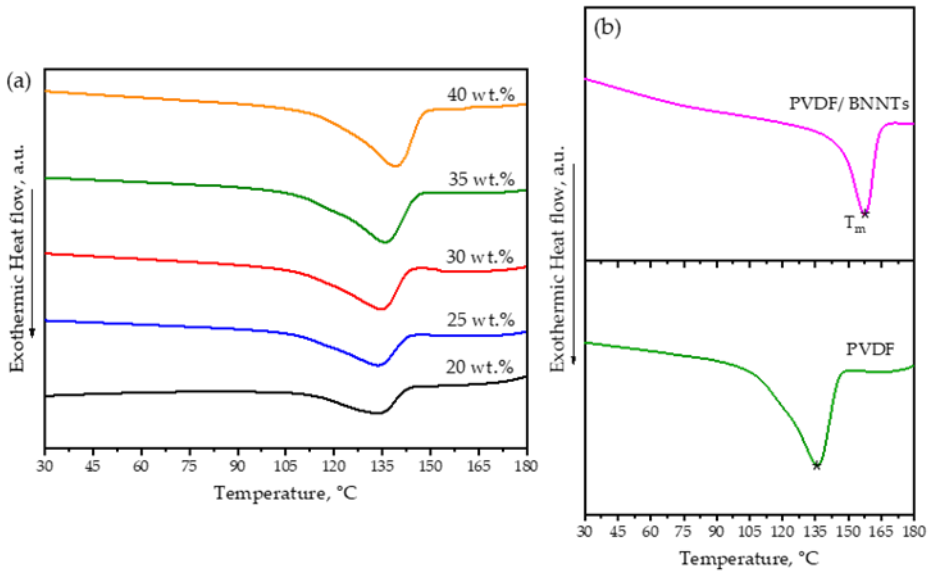

Figure 9.5 Heat flow curves as a function of temperature (a) different wt. % of PVDF polymer and (b) comparison of PVDF to BNNT addition, with melting peak marked (*)

Thermal analysis plays a crucial role in assessing the thermal stability and reliability of sensor materials across a wide temperature range. Thermal parameters, including melting temperature (T_m) and melting enthalpy (ΔH_m), are summarized in Table 9.4, based on the measured thermograms, while the crystallinity content (X_c) was calculated using the equation 9.1,

$$X_c = \frac{\Delta H_m}{\Delta H_m^*} \times 100\% \tag{9.1}$$

where ΔH_m^* is the measured melting enthalpy corresponding to the pure crystalline PVDF (32.11 J/g).

Table 9.4 Melting and crystallinity parameters of polymer-based resin combinations obtained through DSC measurements.

Sample, wt. %	**T_m, °C**	**ΔH_m, J/g**	**X_c, %**
PVDF 20	133.36	9.79	30.49

PVDF 25	133.88	12.02	37.43
PVDF 30	134.33	13.73	42.76
PVDF 35	135.57	15.20	47.34
PVDF 40	138.71	15.78	49.14
PVDF 35/ BNNTs 2	157.60	7.32	23.79

Overall, the results indicated that as the PVDF content increased, the melting temperature, enthalpy, and crystallinity content increased. The observed rise in T_m, ΔH_m, and X_c can be attributed to an increase in the crystalline phase alongside the PVDF content. The crystalline phase typically requires a significant amount of energy to change phase when compared to an amorphous phase. Notably, an increase of 5.35 °C in T_m and 5.99 J/g in ΔH_m was observed when the maximum and minimum amount of polymer wt.% were investigated in this study. Upon the introduction of the BNNT nanofiller, as shown in Figure 9.5 (b), the Tm exhibited a significant increase compared to the PVDF polymer. The presence of BNNT affected the ΔH_m by creating a nucleation site, thus providing insufficient area for crystal formation and alignment. Finally, it is essential to note that the thermogram profiles were single-peaked, indicative of a homogenous composite that melts uniformly during the heating process.

For custom-developed resins with different polymer content, the investigation of rheological behavior plays a crucial role in the selected 3D printing process. Understanding the viscosity of combinations with different PVDF wt. % content under conditions that emulate the shear rate of LCD printing is of paramount importance. Unlike extrusion-based AM techniques that involve high shear forces, vat-based processes like LCD printing result in significantly lower shear forces as the printed material remains relatively static on the building platform, which is displaced at a

low speed to prevent agitation that may affect the curing process and accuracy of the printed component. However, despite being categorized as a low-shear manufacturing process, LCD 3D printing still involves movement and flow within the vat, influenced by the rheological behavior of the material.

To assess viscosity, measurements were recorded over a shear rate ranging from 1 to 100 s^{-1} for all combinations. Figure 9.6 (a) illustrates the pseudoplastic or shear-thinning flow behavior of various PVDF wt. % under a 1-100 s^{-1} shear rate sweep. As the PVDF content increases, a notable trend emerges wherein the shear thinning behavior becomes more pronounced. The samples with 20 wt. % PVDF exhibit Newtonian behavior, with viscosity independent of the applied shear rate, whereas higher PVDF wt. % combinations show a drastic decrease in viscosity as the shear rate increases. This shear-thinning behavior is advantageous during the printing process, as viscosity directly correlates with flowability and self-leveling, crucial properties when evaluating the developed resin.

To compare viscosities as the PVDF wt. % increases, measurements were recorded at a shear rate of 100 s^{-1} to simulate shear loading on geometries with small and complex features. Figure 9.6 (b) depicts the resulting viscosities, clearly illustrating an exponential increase in viscosity as the PVDF wt. % rises. Even though the sample with higher PVDF content exhibited a high polar phase, poor endurance was demonstrated, leading to increased instances of building platform detachment and warping over time.

Introducing BNNT fillers into the polymer matrix resulted in 49% increase in viscosity compared to polymer resin with 35 wt. % PVDF, as shown in Figure 9.6 (b). Nevertheless, the resin with nanofillers exhibited lower viscosity than the resin with 40 wt. % PVDF, remained

within the printable range while enhancing overall piezoelectric performance, as discussed in the following sections.

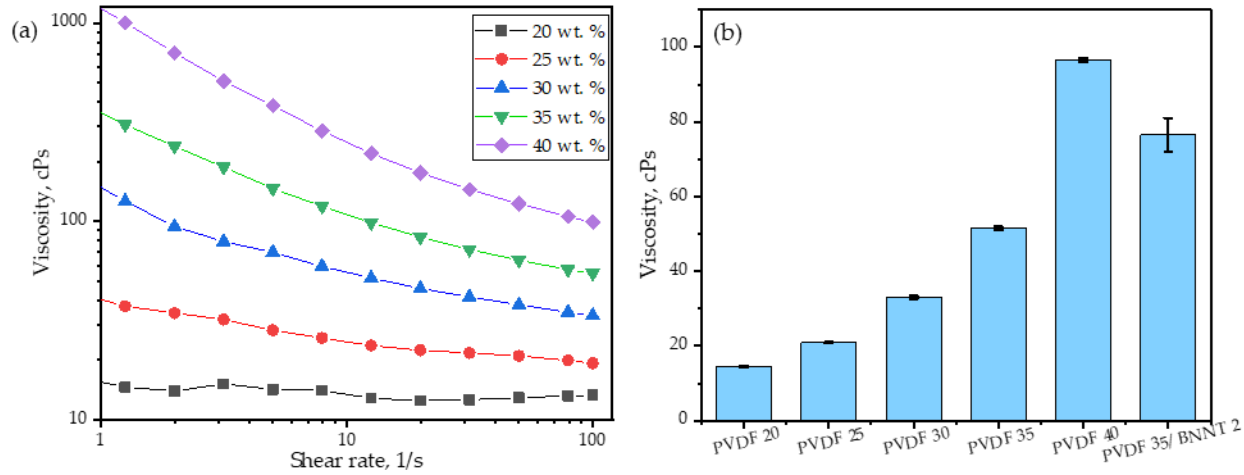

Figure 9.6 The viscosity resin with different PVDF wt. % measured at (a) varying shear rate and (b) fixed shear rate of 100 s^{-1}.

The surface morphology and homogeneity of additives with the PVDF polymer were investigated by examining 3D printed structures with varying PVDF content (20-40 wt. %) using a FEI Quanta 650 scanning electron microscope (SEM). SEM images were captured at 20 kV, as shown in Figure 9.7 (a-e), revealing the surface quality of the printed samples, with an observed increase in polymer content mixed with other added constituents. Specifically, a combination with 40 wt. % PVDF exhibited a reunion phenomenon (highlighted with a circular marker in Figure 34e) and increased warping tendency after printing, leading to easy delamination between layers and compromising structural integrity. It was noted that a maximum range of 35 wt. % PVDF demonstrated beneficial printability and mechanical strength. The polymer softening behavior while printing samples beyond 35 wt. % was also observed in the material's modulus, as discussed in Section 3.6.

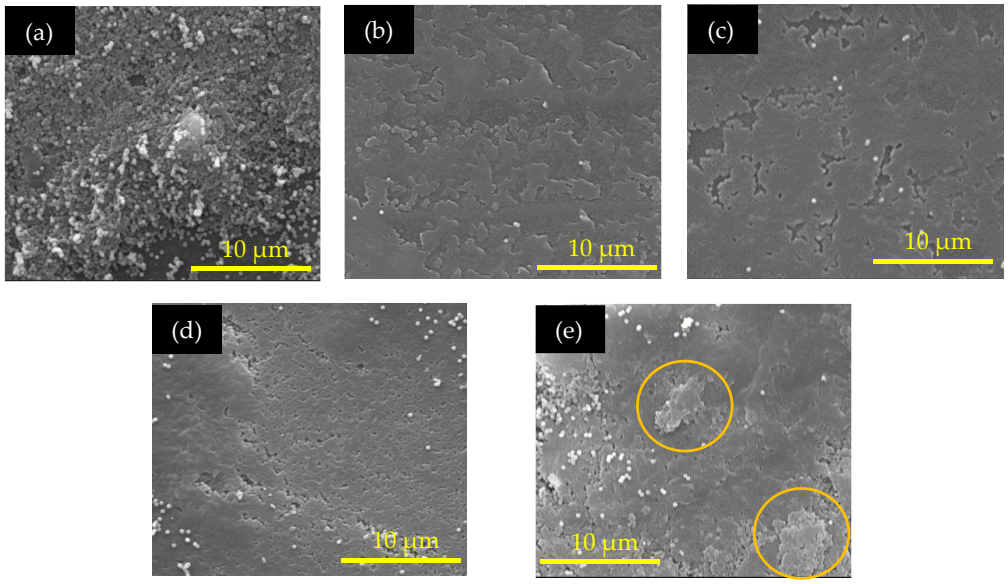

Figure 9.7 SEM images of resin with different PVDF wt.% (a) 20, (b) 25, (c) 30, (d) 35 and (e) 40.

The developed resins demonstrated compatibility with UV-based AM techniques, facilitating the fabrication of high-resolution micro-scale structures with complex shapes. Samples made of the developed polymer and nanocomposite resins were printed using an LCD printer for resolution inspection. Figure 9.8 (a) shows a printed eagle symbol, showcasing high resolution and shape fidelity, particularly evident in intricate features such as the beak and claws, as shown in the zoomed-in images. However, the powder-based polymer resin resulted in a rough surface, necessitating refinement in the cleaning procedure before utilization. The residues on the surface, formed over time after solvent evaporation, were quickly rinsed with deionized water (DI) and blown dry with a handheld blower. Furthermore, the LCD printer proved beneficial not only for printing macro-scale structures but also for producing micro-scale structures with high resolution. SEM inspection of micro-scale scaffold lattice structure, with dimensions of 200 µm width and 1

mm thickness (50 µm thick each layer), was conducted for both polymer and nanocomposite resin materials, as shown in Figure 9.8 (b) and (c). Additionally, the arithmetic mean height (S_a) of the 3D printed samples was measured using the Filmetrics Profilm3D profilometer to obtain the surface roughness parameter. The surface of the nanocomposite was rough ($S_a = 10.54 \pm 0.68$ µm) and flexible, when compared to the polymer sample ($S_a = 7.68 \pm 0.60$ µm) due to the presence of BNNTs. This inspection confirmed the compatibility of the developed resin for UV-based 3D printing with better-stacked layers, offering a scalable approach to manufacturing nanocomposite sensors with high resolution and structural integrity.

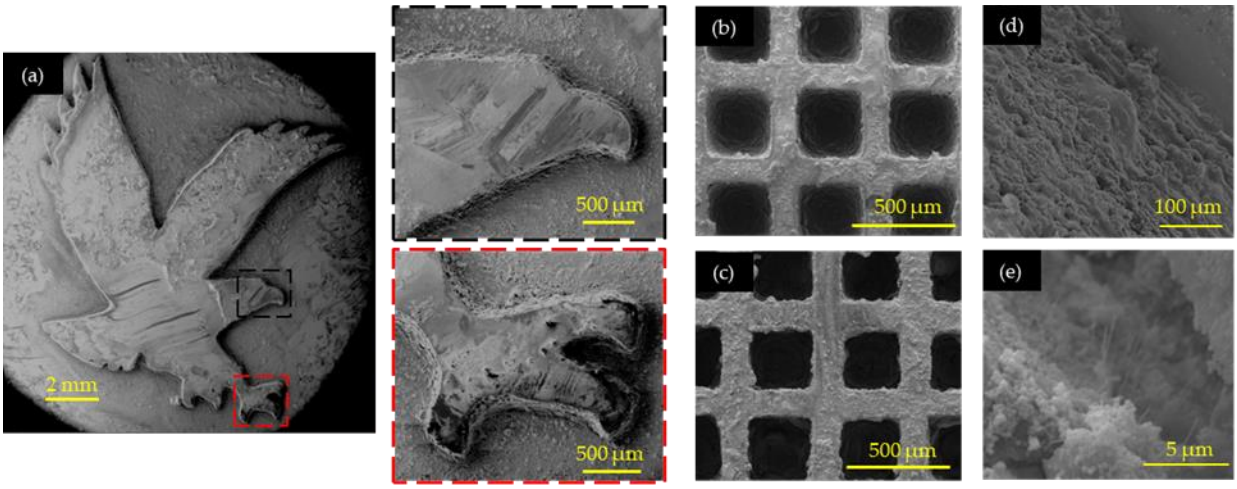

Figure 9.8 Printability of developed resins in micro-scale levels (a) eagle structure in zoomed in images of beak and claws; lattice structures with 200 µm width printed using (b) 35 wt. % PVDF polymer resin, (c) PVDF/ BNNTs nanocomposite resin, (d) zoomed in layer-by-layer printed nanocomposite structure and (e) zoomed in picture of BNNT nanofillers.

To examine the modulus of the 3D printed polymer-based materials, nanoindenter analysis was employed to conduct single indentations and study the viscoelastic response, represented by the reduced modulus (E_r) and the complex modulus (E^*, a vector sum of storage and loss modulus), respectively. Figure 9.9 (a) illustrates the measured moduli alongside indentation hardness values

for PVDF combinations ranging from 20-40 wt. %. Young's modulus of the measured values was calculated based on the equation 9.2,

$$\frac{1}{E_r} = \frac{1-\nu^2}{E} + \frac{1-\nu_i^2}{E_i} \tag{9.2}$$

where E and ν are the Young's modulus and Poisson's ratio of the material being indented (assumed polymer's ν = 0.3), and E_i and ν_i are the elastic modulus and Poisson's ratio of the diamond indenter tip (E_i = 1.14 GPa and ν_i= 0.07).

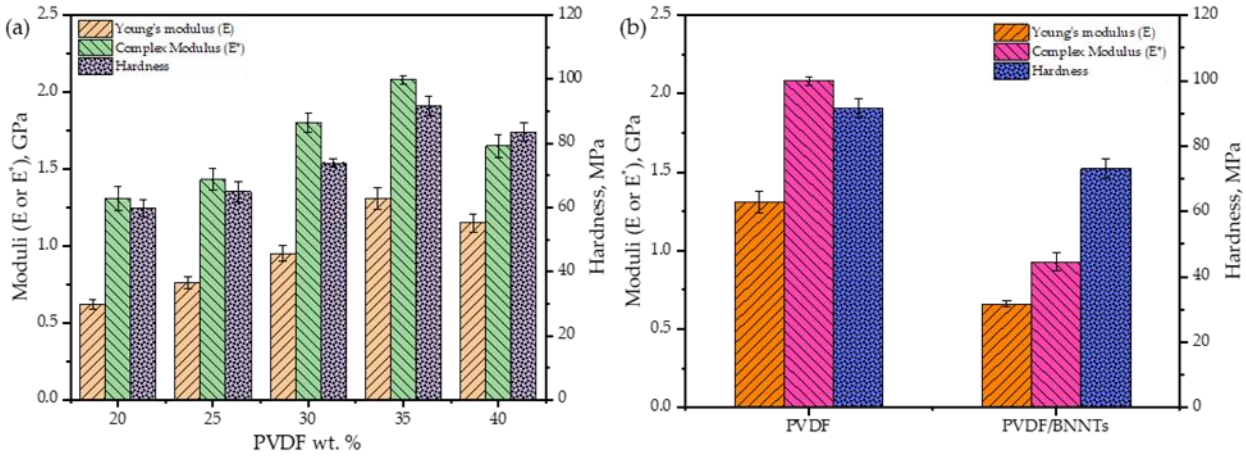

Figure 9.9 Nanoindenter results demonstrating Young's and complex moduli for resins with (a) different PVDF wt.% and (b) added BNNTs nanofiller.

Based on the measured values, the modulus tends to increase with an increase in polymer content, and at 40 wt. %, the modulus dropped due to the flexible and reunion behavior of the polymer combination, as depicted in Figure 9.9 (a). A similar trend was noticed with the addition of BNNTs to the polymer, as shown in Figure 9.9 (b). This phenomenon could be ascribed to the selected UV curing process and loss of crystals, contrary to the increase in modulus observed in casting processes involving temperature and stretching [179]. Despite the low Young's modulus with BNNTs addition, the printed nanocomposite exhibited sturdiness and compliance, suitable

for conformal structures, as noticed in Section 3.5 regarding printability. Moreover, adding beyond 2 wt. % of BNNTs would result in agglomeration to a certain extent and hinder the adhesion between nanofillers and additives, compromising the structural integrity of the 3D printed samples [179, 180].

Material property measurements such as d_{33}, $\varepsilon_{r,}$ and g_{33} play a pivotal role in assessing the performance of piezoelectric sensors. The d_{33} value, indicative of the piezoelectric charge coefficient along the thickness direction within the crystal structure of both the polymer and the nanocomposite, quantifies the charge generated per unit force applied in the thickness direction. Maximizing the piezoelectric response of PVDF polymer occurs when it exhibits a higher β phase, facilitating the alignment of polar groups along the polymer chains. The incorporation of BNNTs serves as a nucleation site for polymer crystallization, resulting in the generation of coupled electric dipole in response to deformation, promoting stress transfer efficiency and enhancing polarization, thus strengthening the piezoelectric response.

The alignment of dipoles in the developed polymer and nanocomposite substrates, crucial for activating piezoelectricity, was achieved through polarization. Utilizing corona poling, a non-contact polarization technique involving the application of a high voltage of 2 kV for 30 min, facilitated this alignment process. The measured d_{33} values with varying PVDF content in the developed resin post-polarization can be seen in Table 9.5. It was evident that the property demonstrated an increase alongside the rise in crystalline content, mirroring the trend observed in the polar phase.

Table 9.5 Measured piezoelectric strain coefficient of 3D printed resin with different PVDF content after polarization.

PVDF Sample, wt.%	**d_{33}, pC/N**
20	3.40 ± 0.15
25	4.33 ± 0.19
30	5.67 ± 0.36
35	7.34 ± 0.20
40	8.14 ± 0.17

Analysis of the measured and calculated piezoelectric properties at 100 Hz, as presented in Table 9.6, reveals a maximum yield of 12.2 pC/N for d_{33} and 114.06 mVm/N for g_{33} upon filler addition to the base polymer. However, it is noteworthy that the achieved d_{33} value is lower than 16-20 pC/N typically reported in the literature [181, 182]. The difference can be attributed to the current composite containing only 35 wt. % polymer and 2 wt. % nanofiller, while the remaining additives lacked piezoelectric properties. This tradeoff between piezoelectric property and printability enabled the fabrication of functional sensors through UV-based 3D printing. Furthermore, dielectric constant measurements at various frequencies demonstrate a 42.62% increase with BNNTs addition. However, a general decrease in ε_r value from 12.08 (at 100 Hz) to 8.1 (at 1 MHz) was observed with frequency increment due to the drop in space charge polarization effect, as shown in Figure 9.10.

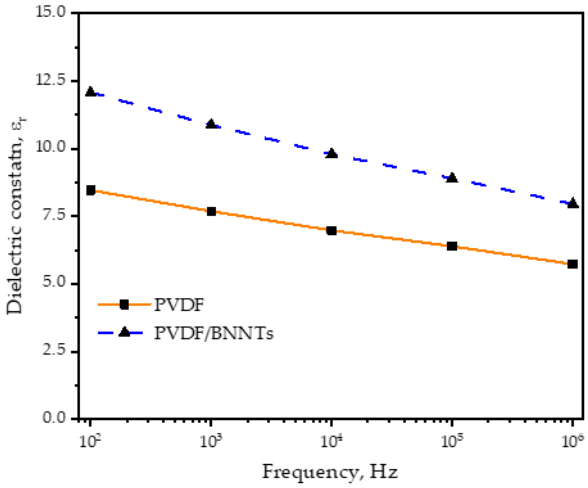

Figure 9.10 Frequency dependent dielectric constant of PVDF resin mixed with BNNT nanofillers.

Table 9.6 Effect of adding fillers in piezoelectric properties measured at 100 Hz.

Sample, wt.%	**d_{33}, pC/N**	**ε_r**	**g_{33}, mVm/N**
PVDF 35	7.34 ± 0.20	8.47 ± 0.01	97.85 ± 0.11
PVDF 35/BNNTs 2	12.20 ± 0.83	12.08 ± 0.02	114.06 ± 0.43

9.4 Force Sensor Application based on the Developed Resin

The piezoelectric responses of 3D printed polymer and nanocomposite sensors were investigated using a platen probe and digital signal oscilloscope setup, as depicted in Figure 9.11 (a). Voltage responses were analyzed at 20 and 50 Hz with applied longitudinal forces of 0.4 and 0.6 N, as shown in Figure 9.11 (b) and (c). The voltage output, indicating average peak-to-peak voltage, exhibited large positive peaks corresponding to applied stress at impact and negative values indicating damping at release.

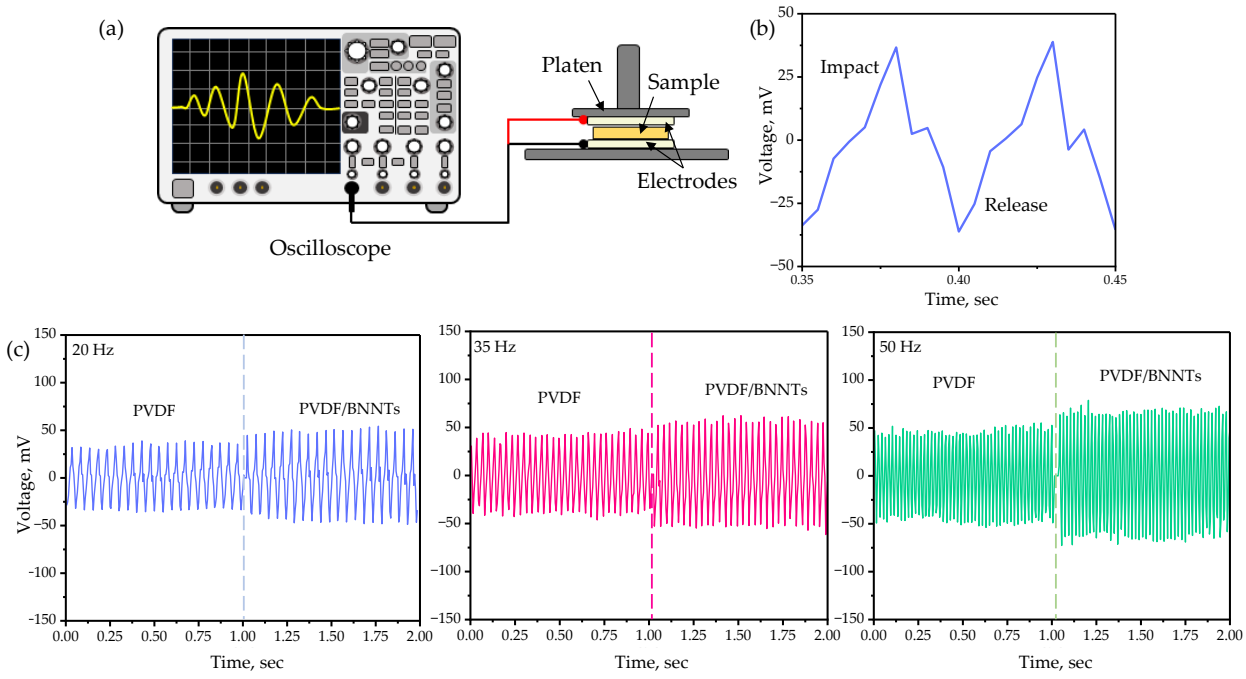

Figure 9.11 (a) Setup for measuring output voltage response; (b) peak-to-peak impact release voltage curve. Piezoelectric response of developed polymer composites measured at (c) 20 Hz, 35 Hz and 50 Hz.

Table 9.7 summarizes the average voltage values, demonstrating the piezoelectric nature of the developed polymer. It is evident that incorporating BNNTs into the polymer matrix shows an increase in sensor response of up to 27.3%, making it suitable for high piezoelectric response sensors.

Table 9.7 Piezoelectric sensor voltage response measured at different frequencies.

Sample	**Voltage, mV**		
	20 Hz	**35 Hz**	**50 Hz**
PVDF 35	33.09 ± 4.43	38.58 ± 3.25	41.75 ± 4.93
PVDF 35/ BNNTs 2	49.24 ± 5.17	54.23 ± 2.92	62.68 ± 6.36

9.5 Capacitive-based Sensor made of the Developed Resin

The capacitive sensor is fabricated using a Phrozen Sonic Mini 8K LCD-based 3D printer exhibiting high XY print resolution of up to 22 µm. A sensor design with an empty electrode channel representing a parallel plate capacitor concept is designed and modeled. After the model is sliced using the Chitubox, the sensor array is printed using the developed photocurable piezoelectric resin, as shown in Figure 9.12.

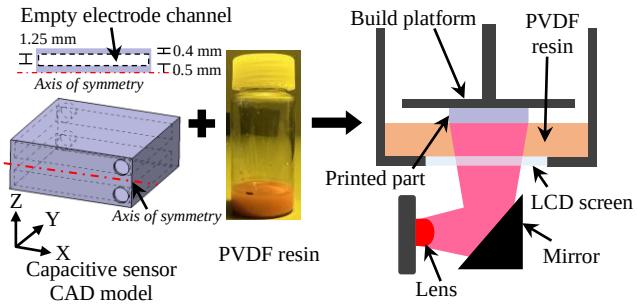

Figure 9.12 Experimental UV-assisted LCD printing setup for sensor development.

As it is a custom-made novel piezoelectric resin, the printing parameters are optimized after multiple trials, which mainly evades factors such as over-polymerization, delamination between layers, and build platform adhesion.

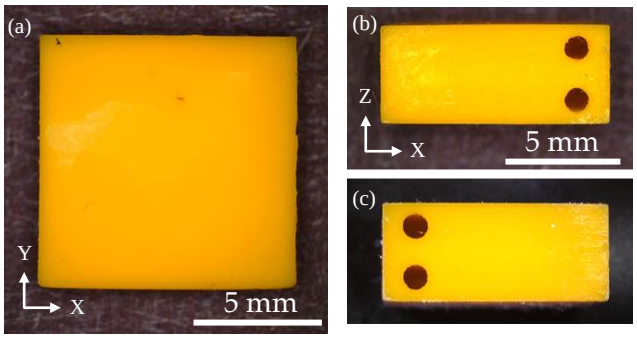

Figure 9.13 LCD printed PVDF capacitive sensor with hollow embedded electrode channels: (a) top, (b) front, and (c) back view.

Figure 9.13 shows a successful sensor print with a 1 mm thick dielectric layer and 1.25 mm empty electrode channel by following the optimized printing parameters listed in Table 9.2. The fabricated sensor with drain holes is rinsed in isopropanol and blow-dried to remove uncured resin from the empty channels.

Electrode filling through an injection process is a common approach to produce embedded electrodes due to its simplicity and ability to replicate the pre-defined channel using a 3D printing process exhibiting better resolution and smoother sidewalls inside the encapsulated substrate. The electrodes are filled using a HYREL 30M (HYREL 3D, Norcross, GA, USA) printer equipped with a dispensing gauge needle, where commercially available conductive PE 873 silver ink (Dupont, Wilmington, DE, USA) is manually loaded into the 10 ml syringe. In this process, the needle injects the conductive ink into the inlet holes of the printed capacitive sensor at a rate of 0.02 mL/min and is cured at room temperature, as shown in Figure 9.14.

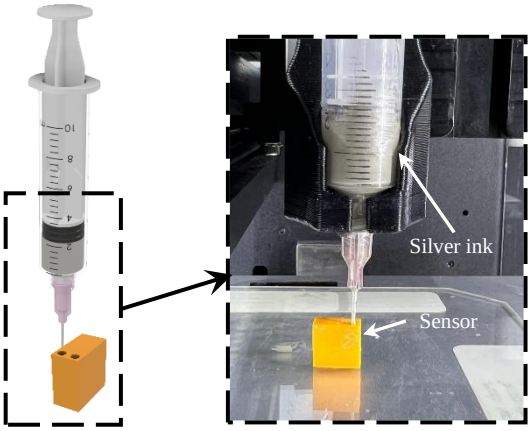

Figure 9.14 Electrode filling using injection-based 3D printing technique.

As the printed PVDF resin is not transparent, the sensor substrate is examined using a Skyscan 1275 Desktop X-ray micro-CT-scanner from Bruker after it is filled with the electrode material. 40 kV X-ray energy is used to scan the sample at different angles. Figure 9.15 (a and b) shows the CT-scan images of the capacitive sensor without and with highly conductive electrode material after curing, confirming that the channel is filled evenly using the injection approach. Wires are installed for direct capacitance measurement, and the inlet ports are sealed by applying a droplet of PVDF resin and cured for 30 sec under UV light exposure, as shown in Figure 9.15 (c).

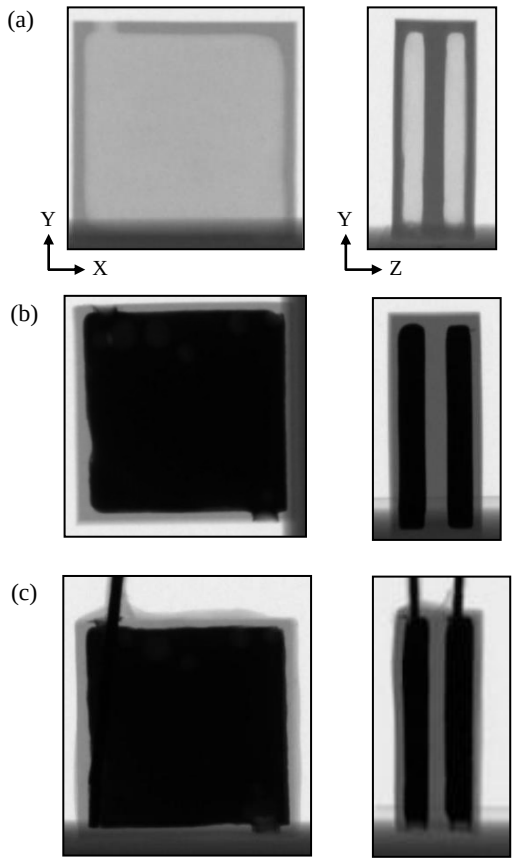

Figure 9.15 CT scan inspection of electrode channels: (a) before, (b) after filling using injection process in front and side view, and (c) with wire installed after capacitance measurement.

9.6 Static Pressure Detection Validation

The sensor response to change in pressure is analyzed with different applied mass conditions to validate the pressure detection capability of the developed sensor. The change in capacitance with different applied masses is measured using a high-precision LCR 6020 meter with a 128-sample average at 1 kHz. Figure 9.16 (a) illustrates the measured change in capacitance as a function of applied pressure at room temperature. Moreover, a real-time sensing capability is also tested with increased mass applied to the sensor over time, as shown in Figure 9.16 (b). Overall, the result reveals that the change in capacitance is increased with a decrease in distance between

the electrodes, confirming the general capacitance equation. It is also noticed that the developed sensor reacts immediately to the change in applied pressure with a slight relaxation time to settle into a constant value at each step.

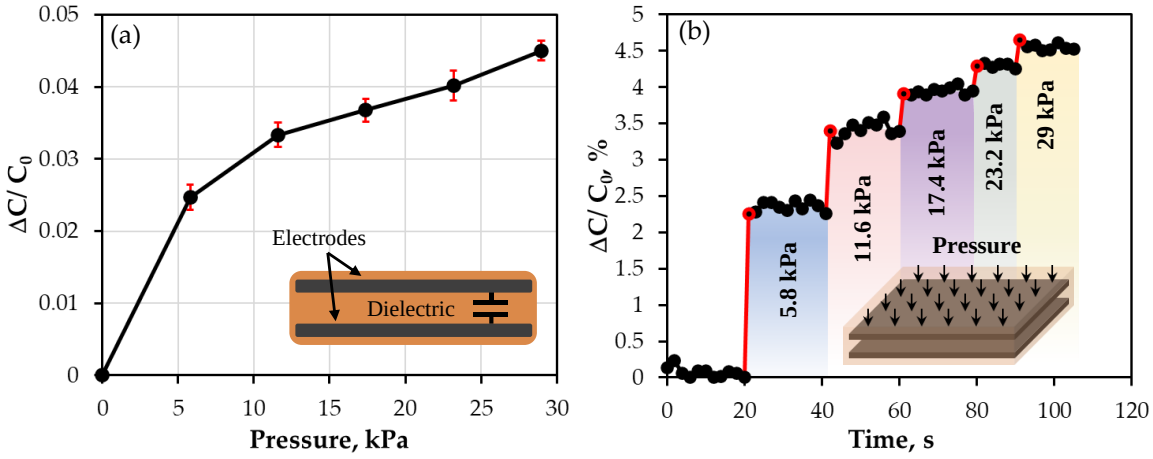

Figure 9.16 Real-time capacitance change response with applied pressure steps at room temperature.

9.7 Wireless Feasibility of Developed PVDF resin

One notable aimed application of the developed resin material is the creation of millimeter-wave (mmWave) cylindrical resonators for in situ real-time monitoring of mechanical strains and temperature in 3D printed host structures. Among different parameters, the dielectric constant of the sensor material is crucial in wireless sensing, particularly for sensors embedded within the host structure. Additionally, to enhance the bonding strength, microstructures are introduced on the sensor's surface [183]. The conceptual schematic of this design is illustrated in Figure 9.17.

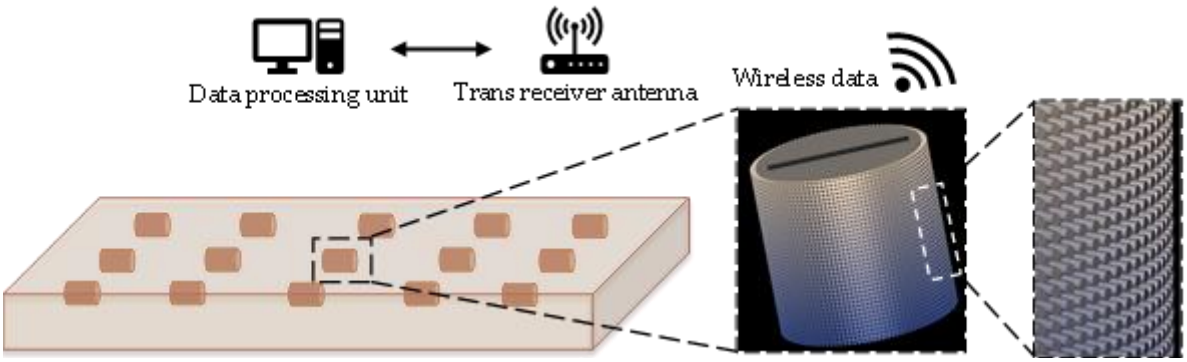

Figure 9.17 Schematic of 3D printed host structure with embedded wireless sensors for anomaly detection and in situ monitoring approach.

AM is an ideal method for producing the sensor with microstructures in a single-step process. The developed piezoelectric material, with its desirable properties, is also an excellent candidate for mass production while exhibiting flexibility. To evaluate the permittivity at the higher frequencies (> 10 GHz), the 3D printed resin material undergoes coplanar waveguide (CPW) measurement. CPW measurement is a technique used to characterize the dielectric properties of materials at microwave frequencies. It involves placing the material under test between two conductors and measuring the resulting S-parameters.

Given the polymer's high signal loss at GHz ranges, the measured signal is inconsistent and very lossy, as shown in Figure 9.18, limiting its applicability in high-frequency scenarios. This issue can be mitigated by using ceramic materials, either 3D printed or commercially available films, which are suitable for strain and temperature measurements at high frequencies. The CPW measurements results indicate that while the resin material may not be ideal for high-frequency applications due to signal loss, it does provide valuable insights into its dielectric properties, guiding further piezo-composite material improvements.

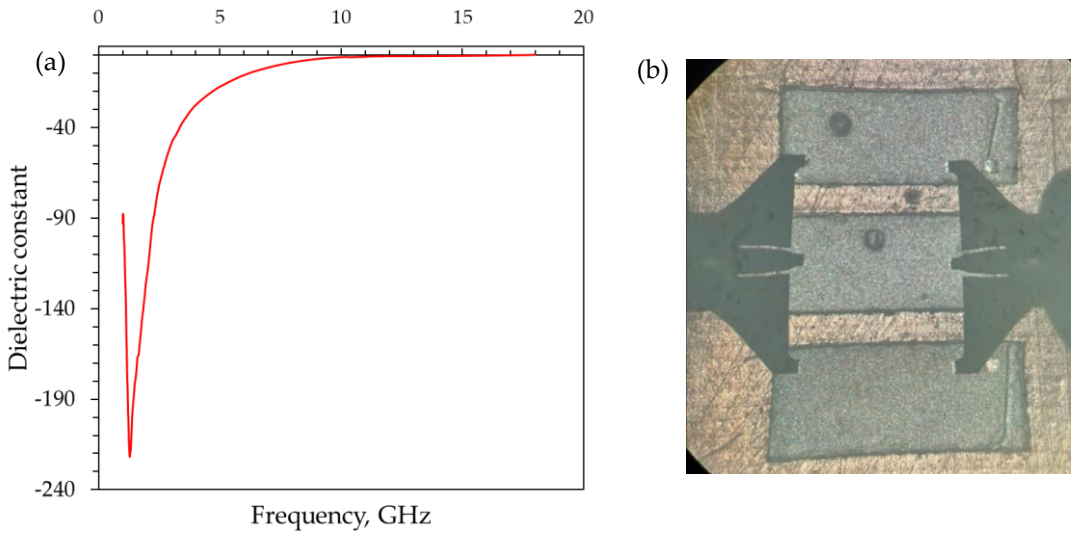

Figure 9.18 (a) Dielectric constant of polymer measured at GHz frequency range and (b) CPW measurement layout on 3D printed polymer material.

Despite the challenges with high-frequency applications, the developed resin material exhibits a dielectric constant of 5.6, making it suitable for MHz range sensor applications. Additionally, its ability to print intricate microstructures in a single -step process without material limitations offers a significant advantage for various sensing applications. The overall idea is to create a wireless array of sensors embedded inside the host structure with optimized design using HFSS modeling and material exhibiting higher dielectric properties. The collected data will be monitored in situ by utilizing effective machine learning approaches.

9.8 Summary and Conclusion

This study highlights the transformative potential of AM technology in the realm of polymer nanocomposite sensors, aimed to enhance the piezoelectric properties and response. By investigating the structural, optical, thermal, rheological, mechanical, and piezoelectric characteristics of a novel sensor resin material based on PVDF and selected nanofiller, this research addresses a gap in the development of UV-based 3D printable sensor devices.

Utilizing an LCD based printer, the findings demonstrate the successful micro-scale printability of the synthesized material, particularly towards the development of capacitance, force and wireless strain sensors. For the capacitance sensor, the electrode filling technique with effective ex-situ CT-scan analysis is executed showcasing evenly filled embedded electrodes. The capacitive sensor response is validated as a function of applied pressure and time. Results show an increase in capacitance with applied pressure that correlates with the constitutive capacitance equation.

Regarding the highly sensitive force sensor, PVDF/ BNNTs nanocomposite yielded a maximum β fraction of 64.89%, with 12.20 pC/N (d_{33}), 114.06 mVm/N (g_{33}) and 12.20 (ε_r). Additionally, the observed increase in piezoelectric voltage response by up to 27.28% highlights the efficacy of this approach in advancing micro-scaled sensor technology. The findings outlined in this work will provide valuable insights for the utilization of polymer-based resins in sensors and energy harvester fields. Additionally, the exploration of a wireless sensor with microstructures to enhance the adhesive performance operating at GHz frequency range for a completely embedded cylindrical resonator case is also discussed from the material integration perspective.

10 Versatile Multifunctional Behavior

This section explores the acoustic wave-based sensor's uniqueness in detecting not only mechanical strains as discussed earlier but also for chemical, gas or Volatile organic compounds (VOC) detection.

10.1 Background and Overview

The ever increasing demand for a gas-sensing microdevice in the detection of toxic and hazardous environmental gases necessitates the development of a piezoelectric sensor for real-time monitoring applications in the biomedical and industrial sectors [184, 185]. Acoustic wave-based sensor utilizes the propagation of acoustic waves to detect the presence and concentration of the analyte. These sensors are extensively used for detecting physical quantities such as strain, pressure, and temperature [47, 104, 107, 186]. Particularly, the selected sensor type showcases high sensitivity towards surface perturbation, such as molecular adsorption and change in viscoelastic properties that amend the wave characteristics propagating in the piezoelectric substrate as compared to the input signal's parameter.

To date, SAW microdevices are coated with a suitable sensing material, such as metal oxides or metals, to sense the targeted gas effectively [101, 187]. Among different metal oxides, zinc oxide (ZnO) is widely used as a gas sensing material for detecting carbon dioxide (CO_2), ammonia (NH_3), ethanol (CH_2CH_2OH) and nitrogen dioxide (NO_2) gases due to its superior physiochemical properties, long-term stability, and quick response time [188-191]. Various thin film deposition techniques have been utilized, including spray pyrolysis, spin coating and vapor deposition. Spray pyrolysis involves spraying a ZnO precursor solution onto heated substrate, where the method undergoes thermal decomposition to form a thin film [192]. Although effective, this method requires high temperatures that can damage the selected polymer based sensitive substrate and offers limited precision in controlling film thickness and uniformity. Spin coating involves a ZnO

solution onto a spinning substrate to distribute the material evenly [193]. While efficient for large, flat surfaces, this method struggles to achieve a uniform thickness on complex geometries and is restricted to low-viscosity solutions. Achieving consistent films on a non-flat surface is challenging, and there is a significant material wastage. Vapor deposition, including techniques like chemical vapor deposition (CVD) and physical vapor deposition (PVD), provide high quality films with excellent control over thickness and composition. However, these methods require expensive equipment and complex procedure, making them less accessible for cost-effective, small-scale applications [194, 195]. Electrospray, on the other hand, offers several advantages for ZnO deposition, especially when targeting small, confined areas with high quality films. This technique allows for precise control over the deposition process, enabling uniform and thin films even on complex geometries. Electrospray operates at room temperature, avoiding thermal damage to substrates, and is economical and scalable, making it ideal for research applications requiring high quality ZnO films in targeted areas. Additionally, major mechanical attributes to be considered are the surface area and thickness of the metal oxide layer, as it dictates the adsorption efficiency.

After selecting the deposition method and materials, it is advantageous to validate the sensor performance of the acoustic wave-based sensor for ethanol detection using numerical tools before proceeding to experimental work. Numerical analysis offers a deeper understanding of sensor's behavior and performance, potentially saving time and resources by optimizing design parameters beforehand. The following section will discuss the methodology of SAW based numerical ethanol detection in detail.

10.2 Numerical Setup for VOC Detection

The physics by which change in gas concentration affects the wave velocity is by changing the sensing layer material density, acting like a mass loading effect, as shown in Figure 10.1. The mass

loading effect is also named as added mass in the Multiphysics tool. The relation with density involves directly with the adsorption of intended VOC or gas to be detected, as shown in following equations,

$$\rho = \rho_{ZnO} + \rho_{ethanol.ZnO} \tag{10.1}$$

$$\rho_{ethanol.ZnO} = K * M * C \tag{10.2}$$

$$C = C_0 * 10^{-6} * P/RT \tag{10.3}$$

where K is the partition coefficient, M is the molar mass of ethanol, C is the concentration in mol/m^3, C_0 is the concentration of the VOC in ppm, P is the operating pressure, R is the gas constant and T is the operating temperature. Table 10.1 lists the change in density of the ZnO layer when exposed to different ethanol concentrations. The change in density is calculated based of the following constant values, such as, molar mass (46.068 g/mol), temperature (298.15 K), gas constant (8.3143 J. mol^{-1}. K), partition coefficient (3.602) and pressure (14.695 Psi). These values are plugged into the numerical tool and the frequency response with a change in density directly proportional to the concentration of ethanol presence is simulated.

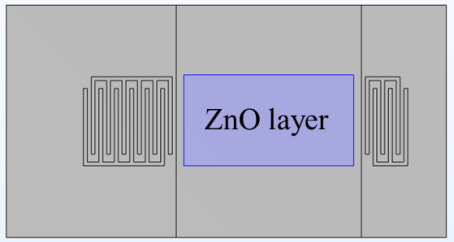

Figure 10.1 Schematic representation of sensing layer addition to the conventional type wave-based sensor.

Table 10.1 Mass loading effect influencing the density of sensing layer with corresponding change in ethanol gas concentration.

Concentration, ppm	**Density, kg/m^3**	**Change in density**
0	5610.00	0
100	5610.75	0.75
200	5611.51	1.51
300	5612.26	2.26
400	5613.01	3.01
500	5613.77	3.77

To evaluate the sensitivity of the simulated sensor, the slope of the calibration plot is validated between 0 to 500 ppm. It is shown that the sensitivity is 0.66 Hz/ ppm with a linear increase with increase in ethanol concentration.

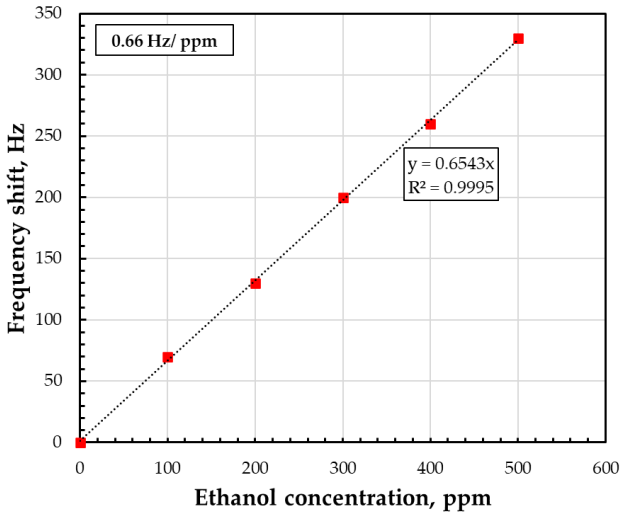

Figure 10.2 Resonant frequency shift vs ethanol gas concentration for wave-based sensor with sensitivity value.

From literature it has been shown that sensitivity enhances to sense this gas at elevated temperature, but the selected polymer material will not be suitable for high temperature. The other relation to sensitivity is the amount of surface area being exposed to specific gas. The sensing mechanism relies on the interaction between the analyte and ionic oxygen species. This interaction leads to the ionization of the oxygen species, which subsequently releases electron back into the conduction band of ZnO. Again, the reason for choosing ZnO is due to the fast response, low detection limit, high selectivity, and reliable performance at a low manufacturing cost and all at room temperature. The following section will explore the experimental process of sensor development with ZnO sensing layer.

10.3 Semiconductor Thin Film Deposition using Electrospray Method

The process of creating a gas sensor involves several meticulous steps, starting with the deposition of ZnO nanoparticles onto a PVDF film using the selected electrospray technique and at the end print fine electrode pattern, as shown in Figure 10.3.

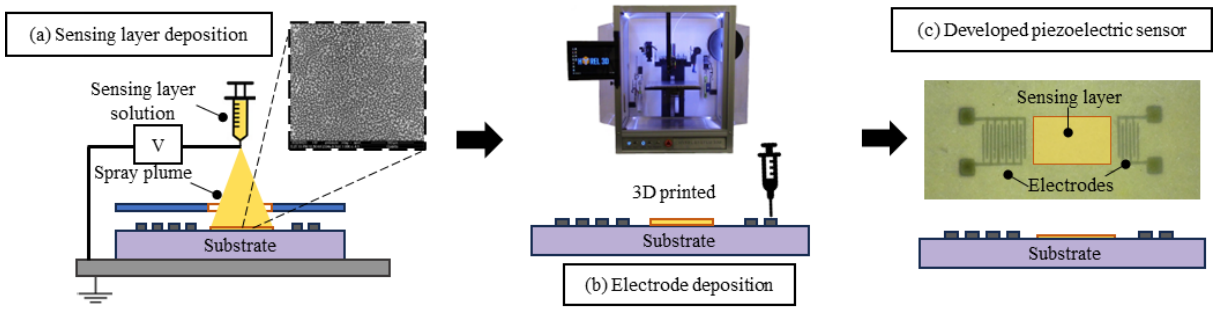

Figure 10.3 Schematic of developed wave-based gas sensor development: (a) sensing layer deposition using electrospray process. The zoom-in microscope image shows ZnO nanoparticles distribution, (b) electrode design deposition using 3D printing method and (c) the complete piezoelectric sensor with sensing layer suitable for gas detection.

To enhance the hydrophilicity of the PVDF film, air plasma treatment is applied prior to the deposition of nanoparticles. Air plasma treatment modifies a polymer surface by introducing polar functional groups, which increase surface energy and make the surface hydrophilic. Figure 10.4 shows the contact angle measurement before (73.7°) and after air plasma (49.8°), which portrays a hydrophilic enhancement suitable for electrospray technique.

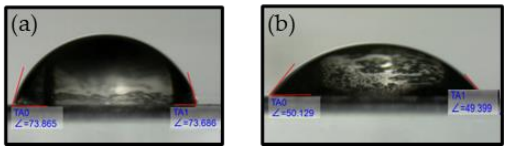

Figure 10.4 Contact angle measurement of water on a polymer substrate (a) before and (b) after air plasma.

Electrospray is a versatile technique used for depositing nanoparticles onto substrate by dispersing a liquid solution through a high electric field. An electrospray apparatus operates by applying a high voltage to a liquid passing through a capillary nozzle. The liquid at the nozzle's tip is subjected to an electrostatic force created by the electric field between the nozzle and a collector. This electrostatic force counterbalances the surface tension of the liquid, shaping it into a distinctive conical formation known as a Taylor cone, as shown in Figure 10.5 (a) [196]. When the applied electric field becomes strong enough, it surpasses the surface tension, leading to the ejection of a liquid jet from the cone's apex towards the collector. Initially, this jet travels in a straight line but subsequently disintegrates into small, charged droplets or particles, dispersed by Coulomb repulsion [197].

One of the primary challenges in electro spraying is achieving a stable Taylor cone, which is crucial for uniform particle deposition. Factors such as flow rate, applied voltage and solution properties need to be carefully controlled to avoid issues like clogging, inconsistent spray patterns,

and non-uniform deposition. In this gas development process, a confined area is created using tape to ensure that only the desired region of the PVDF film is coated with ZnO particles.

Studies have shown several key patterns in electrospray behavior. As the voltage increases, the length of the stable jet grows longer, while the spray angle becomes narrower. Similarly, a higher flow rate results in extended stable jet and a reduced spray angle. Additionally, increasing the voltage boosts the intensity of the electric field and the charge density on the liquid's surface. This higher charge density enhances Coulomb repulsion within the ejected liquid, aiding in the breakup of the jet into finer droplets [198, 199]. These observations underscore the importance of balancing voltage, flow rate, and electrospray dynamics for optimizing the process across various applications. Based on these, the main parameters for the selected electrospray process, including flow rate, applied voltage, and exposure time are optimized through various parametric sweeps. The distribution of ZnO particles is inspected after each electrospray session using a microscope to ensure uniformity and coverage.

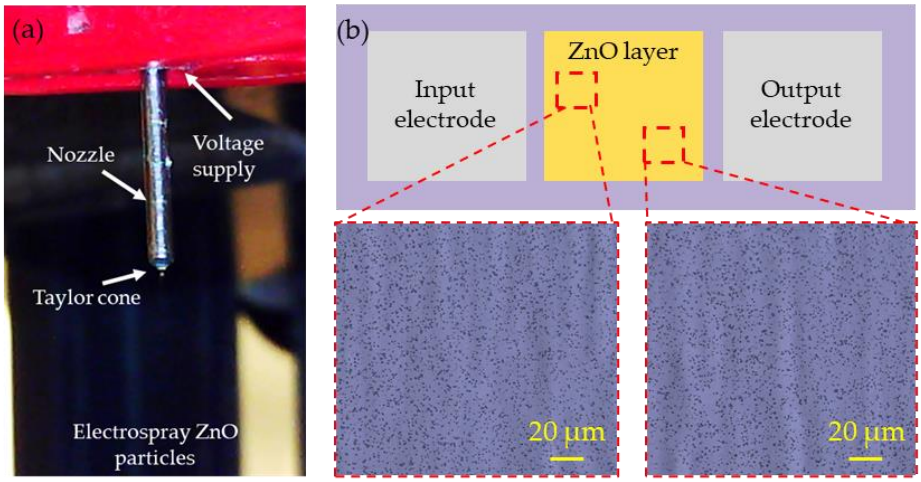

Figure 10.5 (a) The optical image illustrating the actual setup of ZnO nanoparticles electrospray process and (b) microscope images of the sensing layer with sprayed particles.

For the executed electrospray process, the optimal parameters are determined to be a voltage supply between 8-10 kV and a flow rate of 0.012 mL/min, with the needle positioned at 85 mm from the sample surface. Each sample underwent a total of 3 min of electrospraying, divided into three cycles. Each cycle included a 1 min electrospray period followed by a 3 min drying period. This approached ensured uniform distribution and proper adhesion of the ZnO nanoparticles onto the PVDF film, as shown in Figure 10.5 (b). Additionally, it has been observed that the voltage supply needs to be adjusted dynamically in the whole process between the mentioned range to maintain a consistent cone shape. This need for adjustment arises due to changes in the surrounding conditions such as electrostatic intervention and not being under enclosed glove box, which can affect the stability of the spray. One specific challenge is the formation of a thin conductive layer after each spray cycle, which can alter the electrostatic environment. Consequently, continuous monitoring and real-time adjustment of voltage are essential to ensure a stable and effective electrospray operation.

Following the deposition of ZnO sensing layer, electrode deposition is carried out using a HYREL 3D printer. Conductive silver paste is dispensed through a syringe setup with a Gauge 34 (outer diameter: 0.2 mm and inner diameter: 0.08 mm) to create a fine IDT electrode pattern. The critical parameters for printing the IDT electrodes include the print speed (2.6 mm/ sec) and X and Y direction motion, which are controlled via G-code inputs to the printer (Appendix). After several trials, successful IDT patterns (150 µm width) are achieved without discontinuity and are well bonded to the base substrate and around the sensing layer developed, as shown in Figure 10.6. However, the non-pressure-controlled nature of this method results in some challenges as opposed to pressure-controlled method (nScrypt) used in Chapter 4. A small blobs or islands of silver paste tend to form, particularly at corners and edges. Additionally, when the printer moves in one

direction and returns along the same path, it adds a second layer of conductive material due to the built-up pressure on the needle, resulting in thicker IDT than theoretically intended.

Figure 10.6 Microscope images of 3D printed input and output with ZnO sensing layer marked.

Once the IDT electrodes and the ZnO sensing layers are deposited, the sensor is ready for measurement. The developed sensor is designed to detect ethanol, a specific VOC. The optimization and fabrication processes, including the electrospray and electrode printing techniques, ensure that the sensor is functional and capable of responding to specific chemical stimuli. The selection of sensing layer material can be tailored based on the targeted gas.

10.4 Gas Detection Validation

For the gas testing, a custom gas chamber setup is used. This setup includes provision for connecting RF probes, allowing for simultaneous collection of response data with variations in gas supply. The gas chamber is equipped with a mass flow regulator connected to a cylinder that supplies ethanol gas. Split valves are included to control the gas flow, and a vacuum pump is connected to create an airtight seal and prevent gas leaks over time, as shown in Figure 10.7. This setup ensures accurate and reliable measurement of the sensor's response to ethanol VOC.

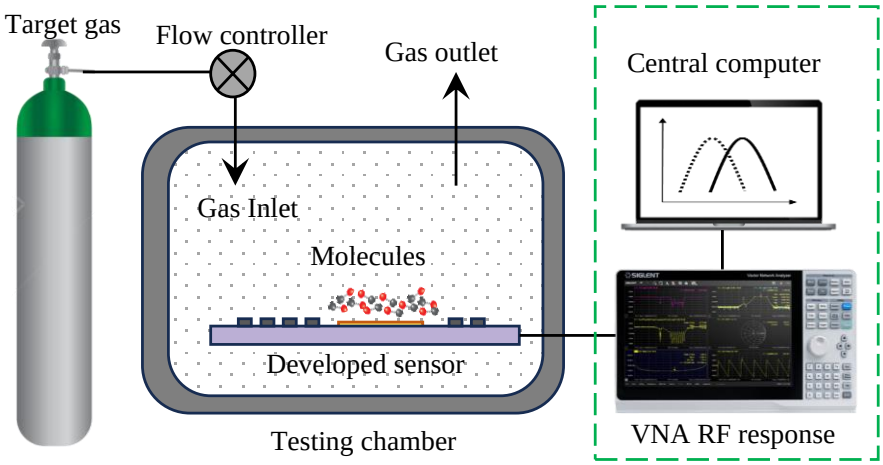

Figure 10.7 Schematic illustration of the gas sensing test system, consisting of test chamber with a piezoelectric sensor mounted inside. The inset depicts the data collection and processing devices, which provides useful real-time detection information.

The sensor's performance is evaluated by measuring the changes in resonant frequency and impedance in the presence of ethanol gas. These measurements are crucial for understanding the sensor's sensitivity and selectivity. The data collected from the Bode VNA 100, both s-parameter (S_{11} and S_{21}), provide insights into the sensor's behavior under different gas concentrations, enabling the optimization of the sensor design for improved performance. Figure 10.8 shows the frequency response for the sensor under no-gas and gas-in conditions. The introduction of ethanol gas (a maximum of 350 ppm) with a constant flow rate of 0.3 L/min into the chamber is observed to cause a noticeable shift in frequency (194 kHz) and peak intensity, which is directly proportional to the change in resistance, reflecting alternations in wave characteristics, as shown in Figure 10.8. Additionally, the sensitivity of the developed sensor for different VOC concentration is plotted, as shown in Figure 10.8 (c). The sensor exhibits 0.5 kHz/ ppm sensitivity to the ethanol VOC. This phenomenon not only confirms the sensor’s ability to detect ethanol but also underscores its

advantageous multifunctional capabilities, enhancing the overall utility of the developed sensor through this research.

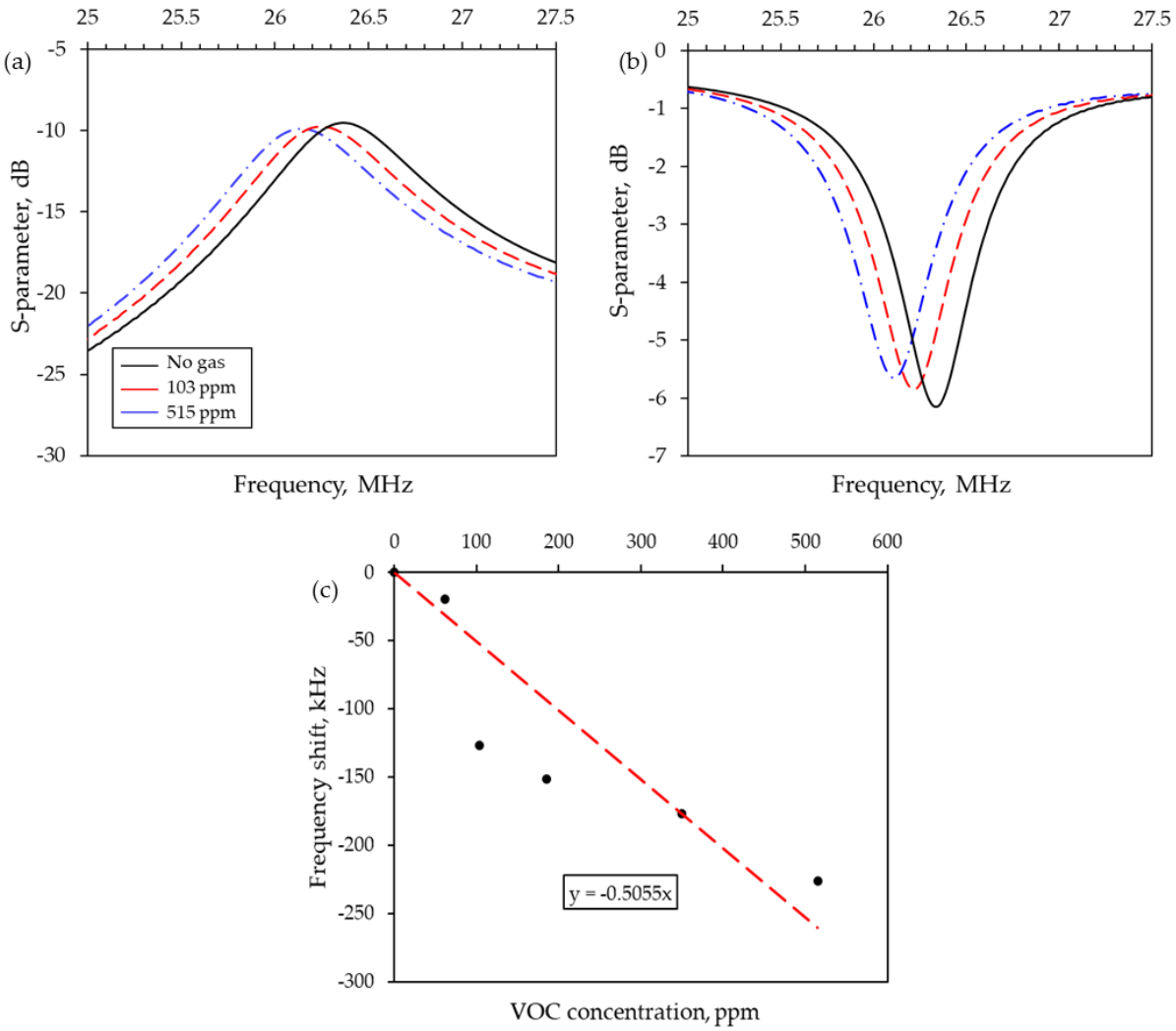

Figure 10.8 Experimental frequency response of the developed gas sensor without and with ethanol supplied inside the test chamber (a) S_{21}, (b) S_{11} with frequency peak amplitude and (c) sensitivity plot.

In summary, the combination of advanced fabrication techniques, such as electrospray and 3D printing, with precise measurement and testing setups, ensures the development of high-

performance gas sensors. These sensors have significant potential for various applications, including environmental monitoring, industrial and human safety in space.

10.5 Microstructure Implementation for Sensitivity Enhancement

Even though the above-performed technique provides a homogenous coating with better sensor performance, attaining a thick volume of sensing material is challenging and expensive. In order to confirm, whether adding a microstructural concept will enhance the sensitivity by adding more surface area, tests need to be conducted. A detailed study of the sensor performance with microstructure is crucial to ensure elements added to the sensing layer will not degrade its performance. But before moving to gas sensing step, it is beneficial to study whether the sensor response will be affected by adding microstructures to the sensing layer, which then be coated with ZnO particles.

The conventional methods for fabrication of microstructures in the sensing layer, such as photo structuring, etching, and molding [146, 200, 201], are a monotonous multi-step process that lacks resolution and requires immense processing time. AM technology have advanced to the point where micro- and nano-scale structures fabrication is feasible with minimized material utilization and reduced mass production costs [202, 203]. This section is geared towards a novel sensor development with microstructure printed directly to the piezoelectric substrate using the 2PP principle [204]. This eliminates the need for a laborious molding process, which is the current bottleneck in the field.

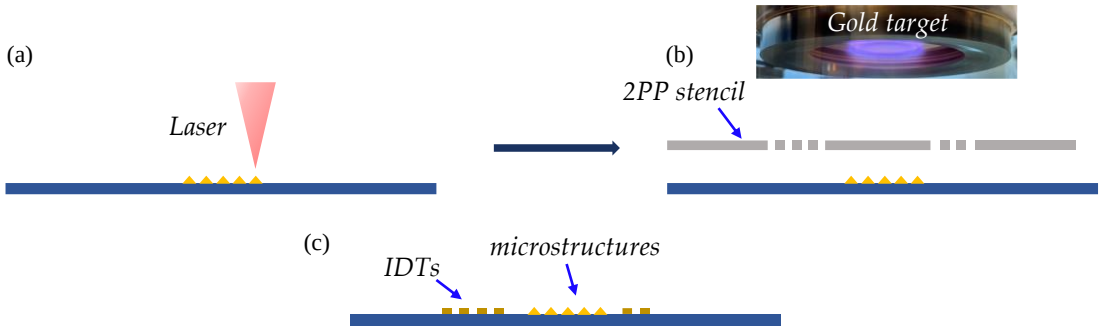

Figure 10.9 The fabrication process of a piezoelectric sensor with microstructures, (a) 2PP printing of microstructures on PVDF film, (b) electrode deposition using 2PP printed stencil and (c) developed sensor.

A suitable combination of the piezoelectric substrate, IDT, and microstructure coated with sensing material is essential for a sensitive micro-device development. PVDF, a well-known polymer for its excellent piezoelectric property, is selected as a substrate material due to its compliance to flexible micro-MEMS device fabrication. Gold electrodes are deposited on the substrate's surface using a 2PP printed stencil with an IDT pattern, which eliminates the clean room requirement. Figure 10.9 indicates the overall sensor fabrication steps, including microstructure patterning and electrode deposition.

10.5.1 Microstructure Designs

Adding microstructures to the sensing layer plays a vital role in sensor performance, as they increase the adsorption rate with an increase in surface area. Different microstructure shapes such as cone, pyramid, dome, and conical frustum, are selected based on their ability to be coated with a metal oxide thin film that enables a sensing mechanism. It is essential to study the influence of microstructure implementation on sensing performance before coating with metal oxides. A microstructure 4x7 grid with 50 µm height and 100 µm spacing is selected, increasing the surface area to a maximum of 39.36 %, as listed in Table 10.2.

Table 10.2 Microstructures dimensions and surface area enhancement.

Micro-shapes	**Dimensions Diameter, µm**	**% Increase in Surface area**
Cone	200	27.42
Pyramid	200	39.36
Dome	200	27.54
Conical frustum	200 (bottom)/ 50 (top)	32.95

10.5.2 Frequency and Time Domain Analysis

The simulation setup and workflow for both frequency and time domain analysis are similar to the previous tests, except the addition of microstructures in the delay line region. The distinct response received for each microstructure design is obtained from the output IDT in the transmission lines, as shown in Figure 10.10 (a) and (b).

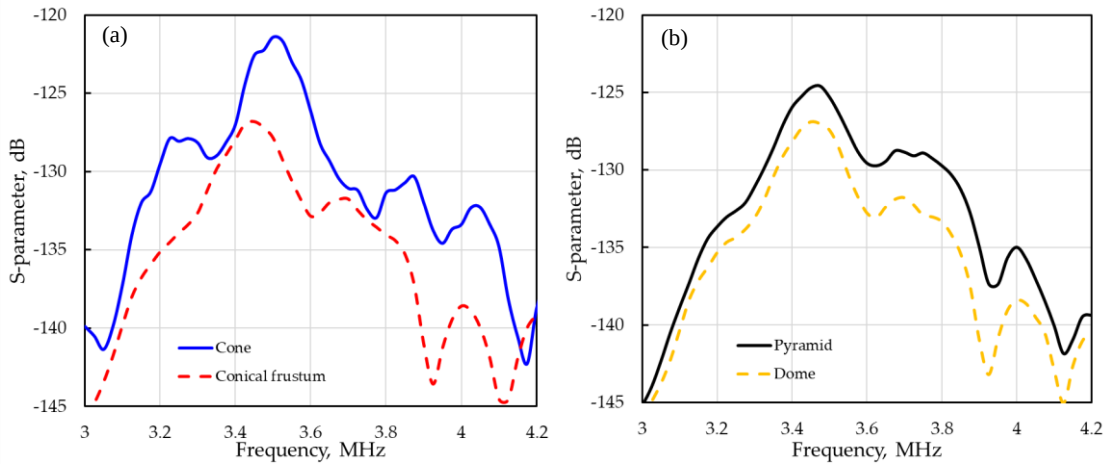

Figure 10.10 Scattering parameter as a function of frequency for different micro-shapes (a) cone/ conical frustum and (b) pyramid and dome.

The voltage amplitude is obtained from the output electrode, which converts the received mechanical wave into a voltage response, as shown in Figure 10.11 (a-d). Simulated results of the SAW sensor with microstructures are summarized in Table 10.3. Based on the numerical results, a 5-10% degradation of sensor response is noticed, in which the pyramid and cone exhibit better performance with an increase in surface area, which supports the microstructure concept. Sensors with pyramid and cone shaped microstructure grids are fabricated, and the response is validated with experimental results.

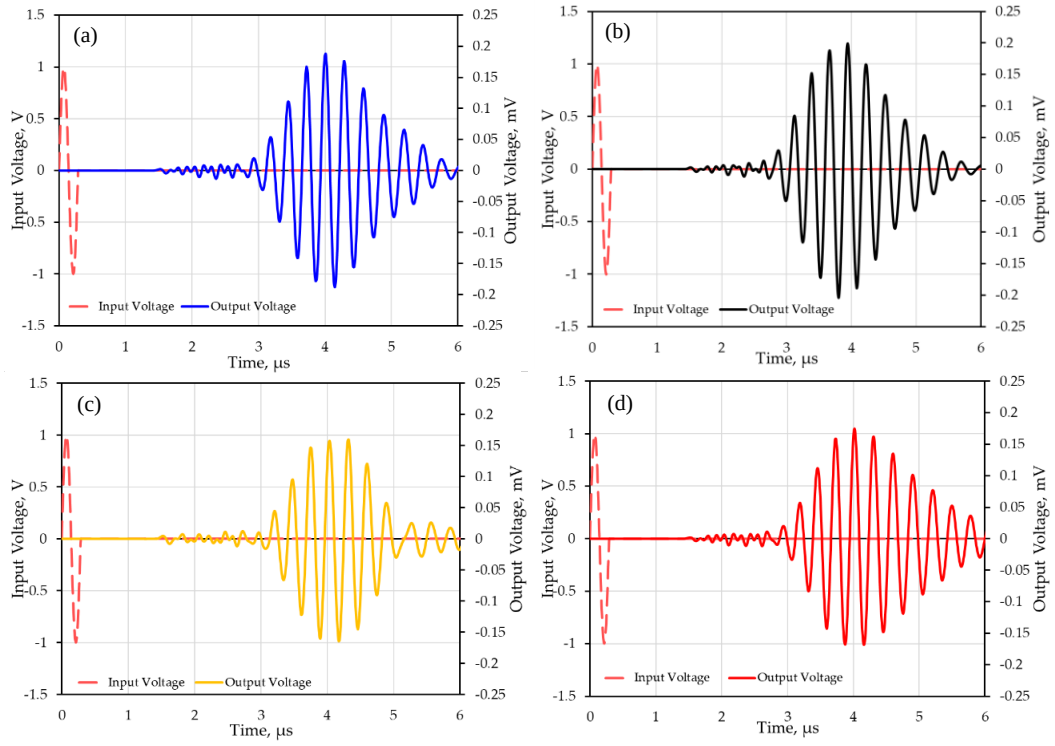

Figure 10.11 Voltage responses as a function of time for different micro-shapes (a) cones, (b) pyramid, (c) dome and (d) conical frustum.

Table 10.3 Summary of sensor's frequency and time-domain analysis response with different microstructure shapes.

Micro-shapes	**Frequency peak, MHz**	**IL, dB**	**Time delay, µs**	**Output Signal, mV**
Conventional*	3.5	-120.16	3.68	0.228
Cone	3.5	-121.41	3.72	0.188
Pyramid	3.475	-124.58	3.71	0.201
Dome	3.45	-126.90	3.75	0.164
Conical frustum	3.45	-126.81	3.74	0.175

* Conventional type represents the sensor without microstructures in the sensing layer.

10.5.3 Microstructures Printing using 2PP Process

The microstructures design made of high viscous negative photoresist (IP-S, Nanoscribe, Karlsruhe, Germany) is printed using a 2PP printer (Photonic Professional GT2, Nanoscribe GmBH, Karlsruhe, Germany) equipped with a 780 nm femtosecond laser. IP-S resin and a 0.8 numerical aperture (NA) lens are utilized to increase the voxel size with quicker microstructure modeling. The printing parameters used for IP-S microstructures are 1 µm slicing distance, 0.5 µm hatching distance, 100 mm/sec base scan speed, and 60% laser power. The base layer count is also increased to avoid the floating of printed parts detached from the print bed.

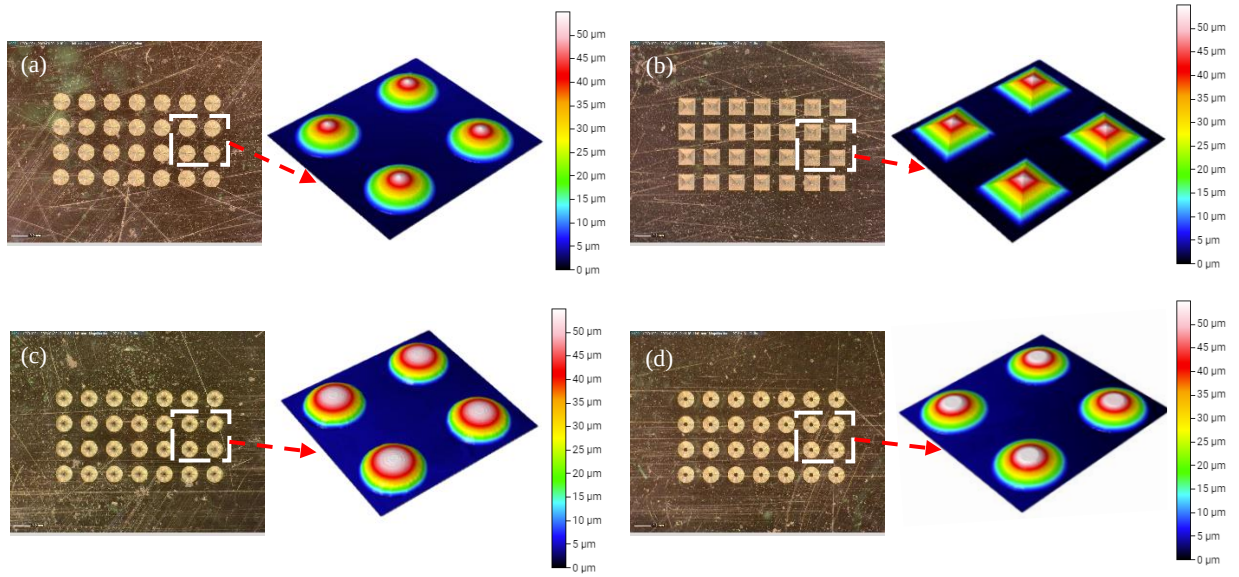

Figure 10.12 2PP printed microstructures on PVDF film with scanned profiles (a) Cone, (b) pyramid, (c) dome and (d) conical frustum.

To increase the adhesion between the microstructure and the PVDF film, the film is salinized, rendering the substrate surface hydrophobic and leading to a chemical bond between polymerized 2PP IP-S resin and substrate. The salinization process includes submerging the PVDF film in a mix of 15 mL acetone with 75 µL of 3-(trimethoxysilyl) propyl methacrylate for 1~2 hours and washed with acetone followed by a deionized water rinse and blow-dried. To validate the printed microstructures' resolution, the printed parts are examined using a Filmetrics 3D profilometer with a spatial sampling of 0.176 µm. For better conductivity, samples are sputtered with gold, and images are captured using a 50x objective with a 10 µm and 70 µm back scan and scan length, respectively, as shown in Figure 10.12.

Table 10.4 Piezoelectric and dielectric properties of PVDF film

Material	**t, μm**	**d33, pC/N**	**ε_r**	**g33, mVm/N**
PVDF	56	25.8	11	265

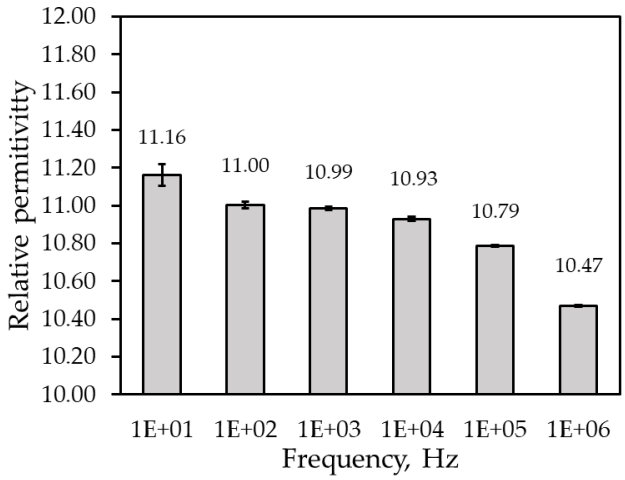

Figure 10.13 Frequency dependent of commercial PVDF's dielectric constant.

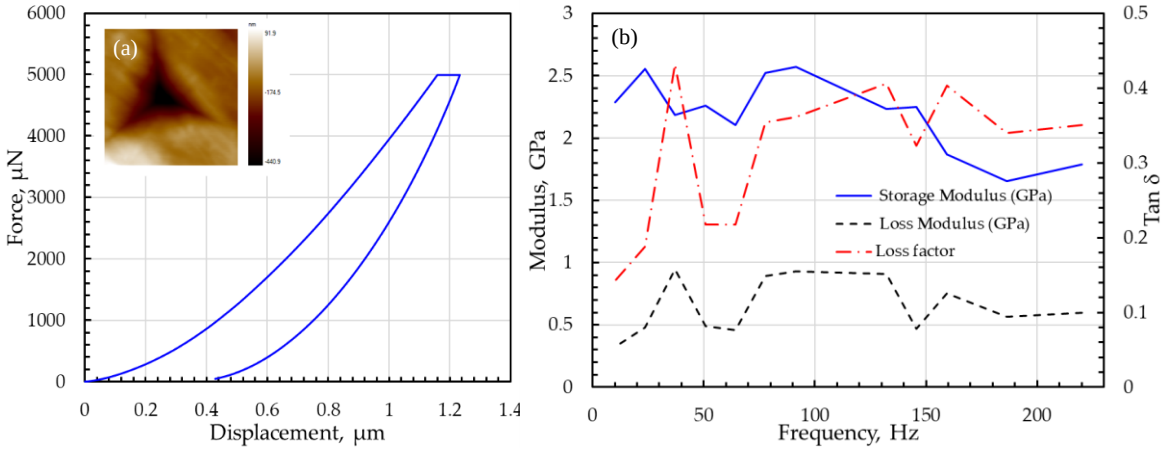

Figure 10.14 Force vs. displacement curve of PVDF film test with Berkovich tip impression and (b) nanoDMA frequency sweep demonstrating modulus and loss factor.

Piezoelectric properties are essential attributes that dictate a material's efficiency for sensing the targeted measurement. Material properties, such as piezoelectric strain coefficient (d), dielectric constant (ε), and piezoelectric voltage constant (g), are involved in the constitutive equation. The piezoelectric strain coefficient (d_{33}) is measured in the thickness direction using a YE2730 A piezometer. Permittivity is an essential property that enables the substrate to hold a charge for an extended period and is calculated using the standard parallel plate equation. The measured and calculated piezoelectric properties of the PVDF film are listed in Table 10.4. From Figure 10.13, it can be noticed that permittivity decreases with an increase in frequency due to polarization drop. PVDF material's modulus, hardness, and dynamic viscoelastic properties, such as young's modulus (E), storage (E'), loss modulus (E"), and loss factor, are measured at a load of 5mN using a Hysitron TI-980 Tribo Indenter equipped with 100 nm radius Berkovich diamond indenter probe. Figure 10.14 (a) indicates the measured reduced modulus of 2.18 ± 0.06 GPa, which is converted to young's modulus of 1.95 ± 0.06 GPa using Poisson's ratio of 0.3 and a hardness of 229.69 ± 10.32 MPa. Figure 10.14 (b) indicates the viscoelastic behavior of PVDF film under a frequency sweep from 10 Hz to 220 Hz, indicating storage modulus fluctuating within the deviation range with varying frequency and respective loss modulus and factor.

10.5.4 Stencil-based IDT Deposition

Gold sputter coater is used to deposit the conductive gold electrode under a vacuum by utilizing a stencil placed on top of the substrate covering the area of printed microstructures. The stencil with IDT pattern is designed and printed using a 2PP printer made of IP-Q resin equipped with a 0.3 numerical aperture (NA) lens, which acts as a mask between the sputter target and PVDF film, as shown in Figure 10.15 (a). The printing parameters used for the IP-Q stencil are 5 µm slicing distance, 1 µm hatching distance, 100 mm/sec base scan speed, and 90% laser power. Based on

the numerical results, IDTs are deposited only on the film with pyramid and cone-shaped microstructures. Figure 10.15 (b) and (c) show well-bonded deposited IDT patterns without any discontinuity using the stencil and microstructures placed between them. A slight shadow effect near the microstructures is also noticed, which can be avoided when depositing thin metal oxide film coated with feasible sputtering techniques.

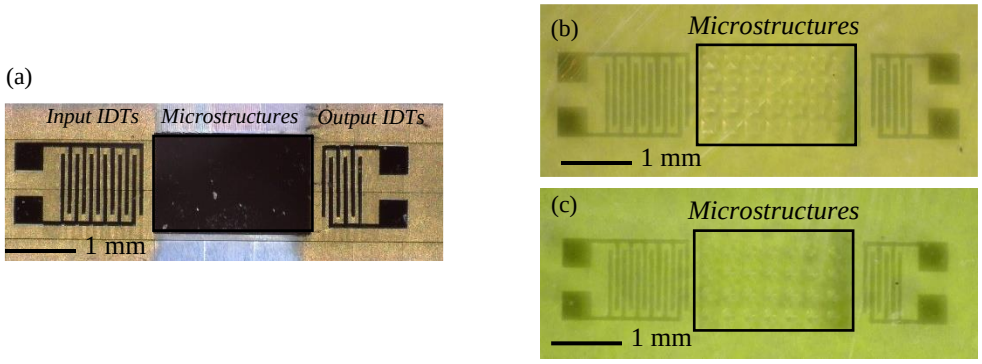

Figure 10.15 (a) 2PP printed stencil after gold sputtering; sensor with microstructures, where IDTs are sputtered with gold electrodes on (b) pyramid and (c) cone sensor type.

10.5.5 Experimental Validation for the Developed Sensor with Microstructures

The frequency response of the developed sensor with micro-structures (pyramid and cone) is measured using a network analyzer (N5227B) and two (40A-GSG-600-DP) pico-probes. The probes are calibrated using a CS-9 substrate, and a 10 dBm signal is given as an input with 50 Ω reference impedance.

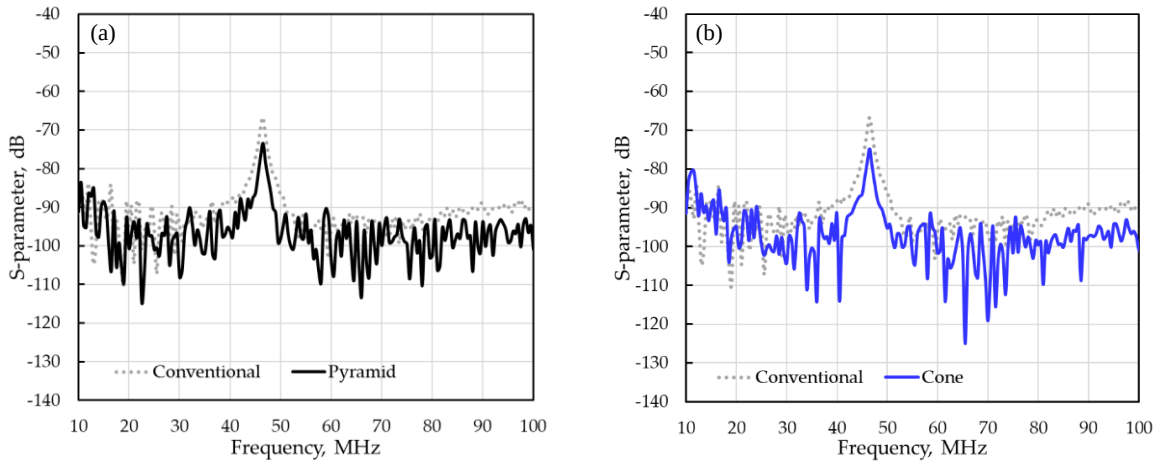

Figure 10.16 Scattering parameter VNA response of sensor with and without microstructure (conventional) (a) pyramid and (b) cone.

The sensor response is measured in the frequency range from 10 MHz to 100 MHz, providing frequency information, as shown in Figure 10.16 (a) and (b). The results reveal that there is no change in resonant frequency with the addition of microstructures to the sensing layer and a ~10% increase in insertion loss from -66.62 dB to -74.85 dB (cone) and -73.43 dB (pyramid), which supports the microstructures implementation. In summary, the wave characteristics didn't change or degrade upon including micro-structures into the sensor's sensing layer, which expands the application range by adding more sensing surface area. A harmonic resonant peak at 46.5 MHz is detected due to the ground probe interference with the piezoelectric substrate, which needs further investigation.

10.6 Summary and Conclusion

In summary, the performance of wave-based sensor for ethanol VOC detection in an environment with a concentration range between 10-500 ppm is numerically studied. For experimental validation of VOC detection, a custom-made gas chamber is utilized. The electrospray method is successfully characterized with optimal parameters utilized to achieve a

homogenous distribution of ZnO nanoparticles, acting as a sensing layer between the electrode pattern. A fine electrode pattern is achieved through a 3D printing process without discontinuity. Experimental gas testing with RF probe testing reveals an evident frequency shift in the presence of ethanol gas that validates the multifunctionality of the developed sensor. Additionally, to enhance the sensitivity, targeted towards enhancing the exposure region is achieved by introducing microstructures into the sensing layer. A piezoelectric sensor based on PVDF with electrodes and microstructures deposited on the surface is successfully developed through a novel 2PP high-resolution printer. The effect of adding different microstructure shapes in the sensing layer is numerically studied in both frequency and time domains. Pyramid and cone shapes are selected as ideal candidates for the gas sensing layer based on the numerical response. Sensor response with added microstructure is tested using VNA with RF probe setup, and the test results show no change in sensor resonant peak, which significantly supports the microstructure implementation concept that can be validated experimentally in the future.

11 Conclusions and Future Work

This chapter compiles the pivotal conclusion derived from this research and outlines pathways for future endeavors in the realm of additive manufacturing-based multifunctional sensor development. By covering a spectrum of topics, these findings provide clear guidance in the sensor field and refine the capabilities of these sensors.

11.1 Conclusions

This research presents a comprehensive investigation into the development of a flexible piezoelectric sensor using advanced AM techniques. The primary aim was to enhance the piezoelectric properties and enable the detection of mechanical strains and ethanol (selected VOC). The research successfully addresses its objectives by exploring innovative methodologies in sensor fabrication, optimizing material performance, configuring electrodes, and establishing multifunctional performance.

Through an extensive analysis of potential AM techniques, the study identifies and implements procedures that significantly reduce manufacturing complexity and facilitate rapid prototyping. These advancements mark a substantial improvement over traditional methods, achieving high-quality printing techniques that enhance the sensor performance. The incorporation of various filler materials into the piezoelectric substrate leads to notable improvements in electromechanical performance. The meticulous evaluation of different materials' impact on sensing efficacy ensures the optimal selection for maximum performance. Table 11.1 summarizes the piezoelectric properties achieved through this AM research that underscores the advancements made in material properties suitable for highly efficient sensors.

Table 11.1 Piezoelectric property achieved through this research by adding different fillers via different AM techniques.

Fabrication method	**Materials**	**d_{33}, pC/N**	**F (β)**
Direct ink writing	PVDF	14	-
	PVDF/ CNTs	43	-
2PP-based reverse replication	PVDF-TrFE	23.8	73.13
	PVDF-TrFE/ BTs	36.5	78.52
Vat polymerization	PVDF	7.35	-
	PVDF/ BNNTs	13	64.89
Hot press method	PVDF/ CNTs	42	76.91
Melt extrusion (commercial)	PVDF	25	-

The numerical modeling and experimental validation of various electrode configurations demonstrate significant enhancements in sensor sensitivity and the figure of merits. The successful implementation of embedded electrodes highlights the potential of advanced techniques in optimizing sensor performance. Additionally, by integrating metal oxide-based functional materials into the sensing layer, the developed sensor can detect ethanol with different concentrations. The addition of microstructures expands the active sensing area, culminating in the creation of a novel multifunctional sensor capable of addressing diverse sensing requirements.

The developed sensor undergoes validation through RF signal measurement techniques across various environmental conditions. The confirmed sensitivity and reliability of the sensor across different AM techniques ensure robustness and practical applicability in real-time monitoring applications. These outcomes significantly advance the state-of-the-art in piezoelectric sensor technology. The innovative methodologies and configurations explored not only enhance sensor

performance but also broaden the scope of applications in aerospace, chemical, gas, and biological fields. The multifunctional capability of the sensor, particularly in VOC detection, underscores its potential for wide-ranging industrial and environmental monitoring applications. To encapsulate the key findings and overall contributions of this work, a summary figure (Figure 11.1) has been included to visually represent the main results and implications of the study.

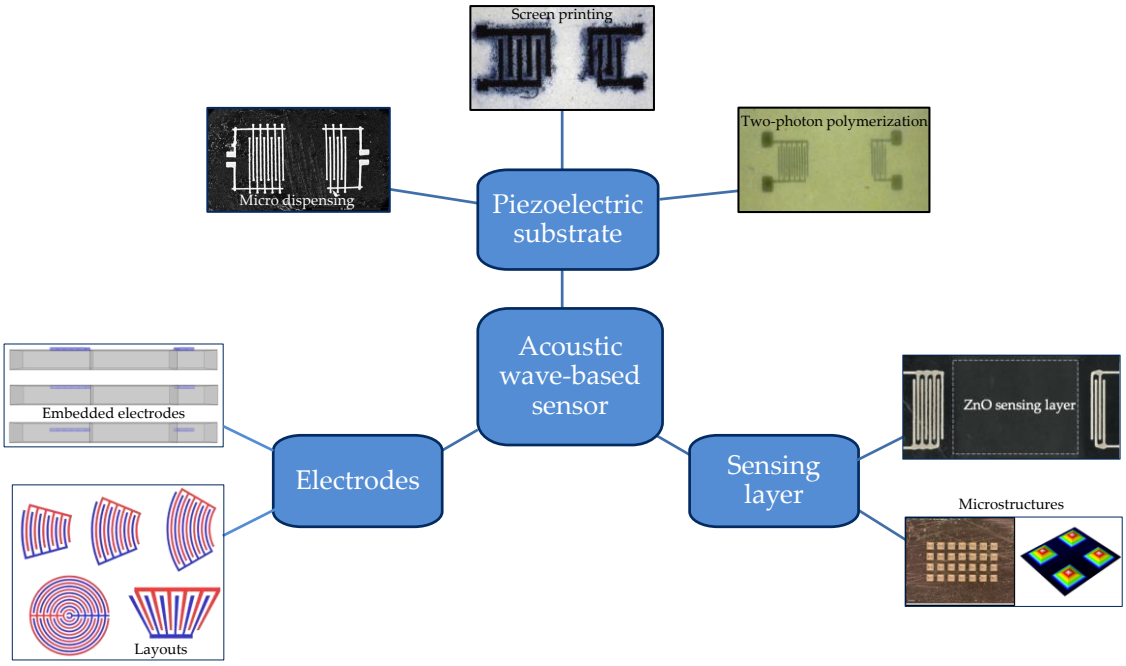

Figure 11.1 Summary of key findings on the multifunctional sensor development.

11.2 Future Work

While this research lays a solid foundation, several avenues for future research are identified to refine further and expand the capabilities of piezoelectric sensors. Future studies could explore new ceramic-filled polymer materials suitable for AM methods that may offer superior piezoelectric and wireless RF performance in high-frequency applications. These materials could significantly enhance the functional range and efficiency of the piezoelectric sensors in various

demanding environments. Dedicated work should be directed towards investigating the ferroelectric properties, thermal behavior, long-term stability, and durability of these materials under various operational conditions. Understanding these characteristics will be essential for developing sensors that are not only more efficient but also more reliable over extended periods. This could include testing under extreme temperature, pressures, and exposure to various chemicals and environmental factors.

Additionally, research on the miniaturization of the sensor and its integration into existing systems could lead to more compact and efficient designs. The development of wireless communication capabilities to enhance remote monitoring applications. This also includes the development of material suitable for the 2PP curing process and embedded electrode-filling techniques. Scaling up the manufacturing process to create an array of sensors while maintaining quality and performance consistency remains a significant challenge. This challenge can be addressed by developing scalable manufacturing techniques that ensure reproducibility and high yield. Automated manufacturing processes, coupled with real-time quality control systems, could play a crucial role in achieving this goal.

Future work should also focus on attaching the developed sensors to real-time structures and ensuring their compatibility with working conditions, including changes in humidity, temperature, and vibrations, which needs proper compensation not to influence sensor performance This is particularly important for aerospace applications, where major parameters include vibrational resonant modes that must avoid interference with the sensor operating frequency. Adhering to FAA standards in terms of sensor development and conducting a detailed study on adhesives or bonding agents, whether on the surface or embedded, will be beneficial. Moreover, the developed sensors will be highly suitable for UAVs with high potential for complete 3D printing. Such

integration could enhance the SHM and operational efficiency of the UAVs. On the other hand, the development of wearable sensors is playing a crucial role in bio and consumer products, offering new opportunities for health monitoring and user interaction.

Expanding the gas sensor work conducted in this research is essential. Extensive studies on the operational and detection limits of the developed sensors, as well their longevity, will provide valuable insights. This includes not only detecting mechanical strains but also VOCs, which is crucial for SHM. The sensor's lifetime and performance in detecting multifunctional measurand is a significant factor to consider in sensor development process.

Interdisciplinary collaboration in fields such as biomedical, and chemical science with machine learning data processing could lead to novel applications and innovations. For example, integrating piezoelectric sensor with machine learning algorithms could enable the development of smart sensors that can adapt to changing conditions and provide more accurate readings. In the biomedical field, sensors could be developed to monitor physiological parameters with high precision, offering new diagnostic and therapeutic tools. By advancing manufacturing techniques, optimizing material and electrode performance, and enhancing multifunctional capabilities, this work sets the stage for future developments and applications in diverse scientific and industrial domains.

12 PUBLICATIONS

Srinivasaraghavan Govindarajan, R., Ren, Z., Melendez, I., Boetcher, S., Madiyar, F., and Kim, D., "Polymer nanocomposites sensor with improved piezoelectric property through additive manufacturing," Sensors 2024, 24(9), 2694. (DOI: 10.3390/s24092694).

Sikulskyi, S., Srinivasaraghavan Govindarajan, R., S. Taylor, Ren, Z., Reed, N., and Kim, D., "Two-photon polymerized wetting morphologies for electrode micropatterning and enhanced microchannel filling," Additive Manufacturing, 2024 (DOI: 10.1016/j.addma.2024.104220).

Ren, Z., Yang, Z., Srinivasaraghavan Govindarajan, R., Madiyar, F., Cheng, M., Kim, D., and Jiang, Y., "Two-photon polymerization of butterfly wing scale inspired surfaces with anisotropic adhesion," ACS Applied Materials & Interfaces, 2024. (DOI: 10.1021/acsami.3c14765).

Madiyar, F., Ghate, S., Nielsen, K., Srinivasaraghavan Govindarajan, R., and Kim, D., "Light-enhanced micropyramidal sensors for Interleukin-6 impedance detection," IEEE Aerospace Conference, 2024 (DOI: 10.1109/AERO58975.2024.10521023).

Reed, N., Srinivasaraghavan Govindarajan, R., and Kim, D., "Characterization of adhesive microstructures for improved bonding in embedded sensors," AIAA SciTech Forum, p.0262, 2024. (DOI: 10.2514/6.2024-0262).

Srinivasaraghavan Govindarajan, R., Sikulskyi, S., Ren, Z., Stark, T., and Kim, D., "Characterization of photocurable IP-PDMS for soft micro systems fabricated by two-photon polymerization 3D printing," Polymers 15, no. 22: 4377, 2023. (DOI: 10.3390/polym15224377).

Srinivasaraghavan Govindarajan, R., Ren, Z., Madiyar, F., and Kim, D., "Additive manufacturing of photocurable PVDF-based capacitive sensor." Smart Materials, Adaptive Structures and Intelligent Systems. American Society of Mechanical Engineers, 2023. (DOI: 10.1115/SMASIS2023-111151).

Srinivasaraghavan Govindarajan, R., Madiyar, F., and Kim, D., "Wave-based sensor responses with embedded electrode layouts," Sensors and Smart Structures Technologies for Civil, Mechanical and Aerospace Systems 2023. Vol. 12486. SPIE, 2023. (DOI: 10.1117/12.2658076).

Srinivasaraghavan Govindarajan, R., Stark, T., Madiyar, F., and Kim, D., "On the performance of PVDF based piezoelectric sensor with microstructures," Sensors and Smart Structures Technologies for Civil, Mechanical and Aerospace Systems 2023. Vol. 12486. SPIE, 2023. (DOI: 10.1117/12.2658072).

Stark, T., Sikulskyi, S., Srinivasaraghavan Govindarajan, R., and Kim, D., "Hydrophilic surface morphology for intricate conductive coatings," In Surface Engineering and Forensics. Vol. 12490. SPIE, 2023. (DOI: 10.1117/12.2658143).

Sikulskyi, S., Ren, Z., Mekonnen, D., Holyoak, A., Srinivasaraghavan Govindarajan, R., and Kim, D., “Additively manufactured unimorph dielectric elastomer actuators: Materials, Design and Fabrication,” Frontiers in Robotics and AI, 2022. (DOI: 10.3398/frobt.2022.1034914).

Srinivasaraghavan Govindarajan, R., Madiyar, F., and Kim, D., “Flexible piezoelectric wave-based sensor: Numerical analysis and validation,” Smart Materials, Adaptive Structures and Intelligent Systems. American Society of Mechanical Engineers, 2022. (DOI: 10.1115/SMASIS2022-91069).

Sikulskyi, S., Ren, Z., Srinivasaraghavan Govindarajan, R., Stark, T., Madiyar, F., and Kim, D., "Additively manufactured unimorph dielectric elastomer actuators with ferroelectric particles for enhanced low-voltage actuation." Electroactive Polymer Actuators and Devices (EAPAD) XXIV. Vol. 12042. SPIE, 2022. (DOI: 10.1117/12.2613128).

Srinivasaraghavan Govindarajan, R., Stark, T., Sikulskyi, S., Madiyar, F., and Kim, D., “Piezoelectric strain sensor through reverse replication based two-photon polymerization,” Sensors and Smart Structures Technologies for Civil, Mechanical, and Aerospace Systems 2022. Vol. 12046. SPIE, 2022. (DOI: 10.1117/12.2630955).

Srinivasaraghavan Govindarajan, R., Rojas, E., and Kim, D., “Surface acoustic wave- based flexible piezocomposite strain sensor,” Crystals 11.12 (2021): 1576, 2021. (DOI: 10.3390/cryst11121576).

Srinivasaraghavan Govindarajan, R., Xu, X., Sikulskyi, S., Madiyar, F., and Kim, D., "Additive manufacturing of flexible nanocomposite SAW sensor for strain detection," Sensors and Smart Structures Technologies for Civil, Mechanical, and Aerospace Systems 2021. Vol. 11591. SPIE, 2021. (DOI: 10.1117/12.2582864).

Srinivasaraghavan Govindarajan, R., R. Eduardo, and Kim, D., "Strain sensing using flexible surface acoustic wave sensor." Sensors and Smart Structures Technologies for Civil, Mechanical, and Aerospace Systems 2020. Vol. 11379. SPIE, 2020. (DOI: 10.1117/12.2558651).

13 REFERENCES

[1] Ye, X.-W., Ni, Y.-Q., and Xia, Y. "Distributed strain sensor networks for in-construction monitoring and safety evaluation of a high-rise building," *International Journal of Distributed Sensor Networks* Vol. 8, No. 9, 2012, p. 685054. https://doi.org/10.1155/2012/685054.

[2] Chen, Z., Zhou, X., Wang, X., Dong, L., and Qian, Y. "Deployment of a Smart Structural Health Monitoring System for Long-Span Arch Bridges: A Review and a Case Study," *Sensors*; Vol. 17, No. 9, 2017. https://doi.org/10.3390/s17092151.

[3] Hassani, S., and Dackermann, U. "A Systematic Review of Advanced Sensor Technologies for Non-Destructive Testing and Structural Health Monitoring," *Sensors*; Vol. 23, No. 4, 2023. https://doi.org/10.3390/s23042204.

[4] Dutta, C., Kumar, J., Das, T. K., and Sagar, S. P. "Recent Advancements in the Development of Sensors for the Structural Health Monitoring (SHM) at High-Temperature Environment: A Review," *IEEE Sensors Journal* Vol. 21, No. 14, 2021, pp. 15904-15916. https://doi.org/10.1109/JSEN.2021.3075535.

[5] Zhang, J., Li, C., Gao, Y., Tan, J., Xuan, F., and Ling, X. "Flexible multimode antenna sensor with strain and humidity sensing capability for structural health monitoring," *Sensors and Actuators A: Physical* Vol. 347, 2022, p. 113960. https://doi.org/10.1016/j.sna.2022.113960.

[6] Annamdas, V. G. M., and Soh, C. K. "Load monitoring using a calibrated piezo diaphragm based impedance strain sensor and wireless sensor network in real time," *Smart Materials and Structures* Vol. 26, No. 4, 2017, p. 045036. https://doi.org/10.1088/1361-665X/aa5f40.

[7] Bisio, I., Garibotto, C., Grattarola, A., Lavagetto, F., Sciarrone, A., and Zerbino, M. "SHM With Low-Cost, Low-Energy and Low-Rate IoT Devices: Reducing Transmission Burden With Compressive Sensing," *IEEE Internet of Things Journal*, 2024, pp. 1-1. https://doi.org/10.1109/JIOT.2024.3390803.

[8] Giurgiutiu, V. "17 - Structural health monitoring (SHM) of aerospace composites," *Polymer Composites in the Aerospace Industry (Second Edition)*. Woodhead Publishing, 2020, pp. 491-558.

[9] Qing, X., Li, W., Wang, Y., and Sun, H. "Piezoelectric Transducer-Based Structural Health Monitoring for Aircraft Applications," *Sensors*; Vol. 19, No. 3, 2019. https://doi.org/10.3390/s19030545.

[10] Hoshyarmanesh, H., and Abbasi, A. "Structural health monitoring of rotary aerospace structures based on electromechanical impedance of integrated piezoelectric transducers," *Journal of Intelligent Material Systems and Structures* Vol. 29, No. 9, 2018, pp. 1799-1817. https://doi.org/10.1177/1045389X17754266.

[11] Ksica, F., Hadas, Z., and Hlinka, J. "Application of Piezoelectric Sensors for Structural Health Monitoring in Aerospace," *2018 5th IEEE International Workshop on Metrology for AeroSpace (MetroAeroSpace)*. 2018, pp. 596-601.

[12] Holford, K. M., Pullin, R., Evans, S. L., Eaton, M. J., Hensman, J., and Worden, K. "Acoustic emission for monitoring aircraft structures," *Proceedings of the Institution of Mechanical Engineers, Part G: Journal of Aerospace Engineering* Vol. 223, No. 5, 2009, pp. 525-532. https://doi.org/10.1243/09544100JAERO404.

[13] Galanopoulos, G., Milanoski, D., Eleftheroglou, N., Broer, A., Zarouchas, D., and Loutas, T. "Acoustic emission-based remaining useful life prognosis of aeronautical structures subjected to compressive fatigue loading," *Engineering Structures* Vol. 290, 2023, p. 116391. https://doi.org/10.1016/j.engstruct.2023.116391.

[14] Dagsever, F., Khodaei, Z. S., and Aliabadi, M. H. "Development of a cyber-physical SHM system for composite structures," *AIP Conference Proceedings* Vol. 2848, No. 1, 2023. https://doi.org/10.1063/5.0145026.

[15] Hassani, S., Dackermann, U., Mousavi, M., and Li, J. "A systematic review of data fusion techniques for optimized structural health monitoring," *Information Fusion* Vol. 103, 2024, p. 102136. https://doi.org/10.1016/j.inffus.2023.102136.

[16] Yang, Y., Xu, W., Gao, Z., Yu, Z., and Zhang, Y. "Research Progress of SHM System for Super High-Rise Buildings Based on Wireless Sensor Network and Cloud Platform," *Remote Sensing*; Vol. 15, No. 6, 2023. https://doi.org/10.3390/rs15061473.

[17] Ngeljaratan, L., Bas, E. E., and Moustafa, M. A. "Unmanned Aerial Vehicle-Based Structural Health Monitoring and Computer Vision-Aided Procedure for Seismic Safety Measures of Linear Infrastructures," *Sensors*; Vol. 24, No. 5, 2024. https://doi.org/10.3390/s24051450.

[18] Park, C. Y., Kim, J. H., and Jun, S.-M. "A structural health monitoring project for a composite unmanned aerial vehicle wing: overview and evaluation tests," *Structural Control and Health Monitoring* Vol. 19, No. 7, 2012, pp. 567-579. https://doi.org/10.1002/stc.1491.

[19] Choi, Y., Abbas, S. H., and Lee, J.-R. "Aircraft integrated structural health monitoring using lasers, piezoelectricity, and fiber optics," *Measurement* Vol. 125, 2018, pp. 294-302. https://doi.org/10.1016/j.measurement.2018.04.067.

[20] Haridas, A., and Speckmann, H. "Structural Health Monitoring (SHM) of Space Structures," *Materials Research Forum LLC*. Vol. 18, 2021, pp. 343-351.

[21] Mancini, S., Tumino, G., and Gaudenzi, P. "Structural Health Monitoring for Future Space Vehicles," *Journal of Intelligent Material Systems and Structures* Vol. 17, No. 7, 2006, pp. 577-585. https://doi.org/10.1177/1045389X06059077.

[22] Guo, H., Xiao, G., Mrad, N., and Yao, J. "Fiber Optic Sensors for Structural Health Monitoring of Air Platforms," *Sensors*; Vol. 11, No. 4, 2011, pp. 3687-3705. https://doi.org/10.3390/s110403687.

[23] Wang, H., Guo, J.-K., Mo, H., Zhou, X., and Han, Y. "Fiber Optic Sensing Technology and Vision Sensing Technology for Structural Health Monitoring," *Sensors*; Vol. 23, No. 9, 2023. https://doi.org/10.3390/s23094334.

[24] Park, S., Parmar, K., Shajari, S., and Sanati, M. "Polymeric carbon nanotube nanocomposite-based force sensors," *CIRP Annals* Vol. 65, No. 1, 2016, pp. 361-364. https://doi.org/10.1016/j.cirp.2016.04.078.

[25] Stowell, W., and Weise, R. "Application of thin film strain gages and thermocouples for measurement on aircraft engine parts," *19th Joint Propulsion Conference*. 1983, p. 1292.

[26] Lei, K. F., Lee, K.-F., and Lee, M.-Y. "Development of a flexible PDMS capacitive pressure sensor for plantar pressure measurement," *Microelectronic Engineering* Vol. 99, 2012, pp. 1-5. https://doi.org/10.1016/j.mee.2012.06.005.

[27] Pignanelli, J., Schlingman, K., Carmichael, T. B., Rondeau-Gagné, S., and Ahamed, M. J. "A comparative analysis of capacitive-based flexible PDMS pressure sensors," *Sensors and Actuators A: Physical* Vol. 285, 2019, pp. 427-436. https://doi.org/10.1016/j.sna.2018.11.014.

[28] Chen, L., Chen, X., Zhang, Z., Li, T., Zhao, T., Li, X., and Zhang, J. "PDMS-Based Capacitive Pressure Sensor for Flexible Transparent Electronics," *Journal of Sensors* Vol. 2019, 2019, p. 1418374. https://doi.org/10.1155/2019/1418374.

[29] Reddy, A., Narakathu, B., Atashbar, M., Rebros, M., Rebrosova, E., Bazuin, B., Joyce, M., Fleming, P., and Pekarovicova, A. "Printed capacitive based humidity sensors on flexible substrates," *Sensor Letters* Vol. 9, No. 2, 2011, pp. 869-871.

https://doi.org/10.1166/sl.2011.1633.

[30] Su, P.-G., Sun, Y.-L., and Lin, C.-C. "Humidity sensor based on PMMA simultaneously doped with two different salts," *Sensors and Actuators B: Chemical* Vol. 113, No. 2, 2006, pp. 883-886. https://doi.org/10.1016/j.snb.2005.03.052.

[31] Hu, W., Niu, X., Zhao, R., and Pei, Q. "Elastomeric transparent capacitive sensors based on an interpenetrating composite of silver nanowires and polyurethane," *Applied Physics Letters* Vol. 102, No. 8, 2013, p. 083303. https://doi.org/10.1063/1.4794143.

[32] Kim, Y., and Kim, J.-W. "Silver nanowire networks embedded in urethane acrylate for flexible capacitive touch sensor," *Applied Surface Science* Vol. 363, 2016, pp. 1-6. https://doi.org/10.1016/j.apsusc.2015.11.052.

[33] Yoo, K.-P., Lim, L.-T., Min, N.-K., Lee, M. J., Lee, C. J., and Park, C.-W. "Novel resistive-type humidity sensor based on multiwall carbon nanotube/polyimide composite films," *Sensors and Actuators B: Chemical* Vol. 145, No. 1, 2010, pp. 120-125. https://doi.org/10.1016/j.snb.2009.11.041.

[34] Han, T., Nag, A., Afsarimanesh, N., Akhter, F., Liu, H., Sapra, S., Mukhopadhyay, S., and Xu, Y. "Gold/Polyimide-Based Resistive Strain Sensors," *Electronics*; Vol. 8, No. 5, 2019. https://doi.org/10.3390/electronics8050565.

[35] Morais, R. M., Klem, M. d. S., Nogueira, G. L., Gomes, T. C., and Alves, N. "Low Cost Humidity Sensor Based on PANI/PEDOT:PSS Printed on Paper," *IEEE Sensors Journal* Vol. 18, No. 7, 2018, pp. 2647-2651. https://doi.org/10.1109/JSEN.2018.2803018.

[36] Krishnan, A., Das, S., and Bhattacharjee, M. "Flexible Piezoresistive Pressure and Temperature Sensor Module for Continuous Monitoring of Cardiac Health," *IEEE Journal on Flexible Electronics* Vol. 2, No. 5, 2023, pp. 350-357. https://doi.org/10.1109/JFLEX.2023.3243877.

[37] Ma, L., Lei, X., Guo, X., Wang, L., Li, S., Shu, T., Cheng, G. J., and Liu, F. "Carbon Black/Graphene Nanosheet Composites for Three-Dimensional Flexible Piezoresistive Sensors," *ACS Applied Nano Materials* Vol. 5, No. 5, 2022, pp. 7142-7149. https://doi.org/10.1021/acsanm.2c01081.

[38] Ciampaglia, A., Ciardiello, R., Cesano, F., Belingardi, G., and Brunella, V. "Multifunctional material design for strain sensing: Carbon black effect on mechanical and electrical properties of polyamides," *Composite Structures* Vol. 304, 2023, p. 116373. https://doi.org/10.1016/j.compstruct.2022.116373.

[39] Ba Hashwan, S. S., Khir, M. H. M., Nawi, I. M., Ahmad, M. R., Hanif, M., Zahoor, F., Al-Douri, Y., Algamili, A. S., Bature, U. I., Alabsi, S. S., Sabbea, M. O. B., and Junaid, M. "A review of piezoelectric MEMS sensors and actuators for gas detection application," *Discover Nano* Vol. 18, No. 1, 2023, p. 25. https://doi.org/10.1186/s11671-023-03779-8.

[40] Giurgiutiu, V. *Structural health monitoring: with piezoelectric wafer active sensors*: Elsevier, 2007.

[41] Zhang, S., Li, F., Yu, F., Jiang, X., Lee, H.-Y., Luo, J., and Shrout, T. R. "Recent Developments in Piezoelectric Crystals," *J. Korean Ceram. Soc* Vol. 55, No. 5, 2018, pp. 419-439. https://doi.org/10.4191/kcers.2018.55.5.12.

[42] Yin, J., Chen, S., Wong, V. K., and Yao, K. "Thermal Sprayed Lead-Free Piezoelectric Ceramic Coatings for Ultrasonic Structural Health Monitoring," *IEEE Transactions on Ultrasonics, Ferroelectrics, and Frequency Control* Vol. 69, No. 11, 2022, pp. 3070-3080. 10.1109/TUFFC.2022.3176488.

[43] Mitkus, R., Piechowiak, L., and Sinapius, M. "Characterization of UV Light Curable Piezoelectric 0-0-3 Composites Filled with Lead-Free Ceramics and Conductive Nanoparticles," *Journal of Composites Science*; Vol. 7, No. 2, 2023. https://doi.org/10.3390/jcs7020089.

[44] Guler, Z., Vazquez, I. R., and Jackson, N. "Multi-functional 0–3 composite polyimide films for microsystem applications," *Smart Materials and Structures* Vol. 32, No. 7, 2023, p. 075015. https://doi.org/10.1088/1361-665X/acdba2.

[45] Jo, E.-B., Lee, Y.-A., Cho, Y.-A., Günther, P. A., Gebhardt, S. E., Neubert, H., and Kim, H.-S. "The 0-3 Lead Zirconate-Titanate (PZT)/Polyvinyl-Butyral (PVB) Composite for Tactile Sensing," *Sensors*; Vol. 23, No. 3, 2023. https://doi.org/10.3390/s23031649.

[46] Panda, P. K., and Sahoo, B. "PZT to Lead Free Piezo Ceramics: A Review," *Ferroelectrics* Vol. 474, No. 1, 2015, pp. 128-143. https://doi.org/10.1080/00150193.2015.997146.

[47] Srinivasaraghavan Govindarajan, R., Rojas-Nastrucci, E., and Kim, D. "Surface Acoustic Wave-Based Flexible Piezocomposite Strain Sensor," *Crystals* Vol. 11, No. 12, 2021, p. 1576. https://doi.org/10.3390/cryst11121576.

[48] Sikulskyi, S., Zefu, R., Srinivasaraghavan Govindarajan, R., Mekonnen, D., Madiyar, F., and Kim, D. "Additively manufactured unimorph dielectric elastomer actuators with

ferroelectric particles for enhanced low-voltage actuation," *SPIE Smart Structures + Nondestructive Evaluation*. Vol. 12042, SPIE, 2022.

[49] Wada, S., Suzuki, S., Noma, T., Suzuki, T., Osada, M., Kakihana, M., Park, S.-E., Cross, L. E., and Shrout, T. R. "Enhanced piezoelectric property of barium titanate single crystals with engineered domain configurations," *Japanese journal of applied physics* Vol. 38, No. 9S, 1999, p. 5505.
https://doi.org/10.1063/1.1957130.

[50] Dong, Y., Zou, K., Liang, R., and Zhou, Z. "Review of BiScO3-PbTiO3 piezoelectric materials for high temperature applications: fundamental, progress, and perspective," *Progress in Materials Science* Vol. 132, 2023, p. 101026.
https://doi.org/10.1016/j.pmatsci.2022.101026.

[51] Sappati, K. K., and Bhadra, S. "Piezoelectric Polymer and Paper Substrates: A Review," *Sensors*; Vol. 18, No. 11, 2018.
https://doi.org/10.3390/s18113605.

[52] Bharti, V., Kaura, T., and Nath, R. "Improved piezoelectricity in solvent-cast PVC films," *IEEE Transactions on Dielectrics and Electrical Insulation* Vol. 2, No. 6, 1995, pp. 1106-1110.
https://doi.org/10.1109/TDEI.1995.8881940.

[53] Tuan Rahim, T. N. A., Abdullah, A. M., Md Akil, H., Mohamad, D., and Rajion, Z. A. "Preparation and characterization of a newly developed polyamide composite utilising an affordable 3D printer," *Journal of Reinforced Plastics and Composites* Vol. 34, No. 19, 2015, pp. 1628-1638.
https://doi.org/10.1177/0731684415594692.

[54] Zhang, X., Fan, W., and Liu, T. "Fused deposition modeling 3D printing of polyamide-based composites and its applications," *Composites Communications* Vol. 21, 2020, p. 100413.
https://doi.org/10.1016/j.coco.2020.100413.

[55] Dawoud, M., Taha, I., and Ebeid, S. J. "Strain sensing behaviour of 3D printed carbon black filled ABS," *Journal of Manufacturing Processes* Vol. 35, 2018, pp. 337-342.
https://doi.org/10.1016/j.jmapro.2018.08.012.

[56] Santos Oliveira, R., Batista da Silva, H., Cunha de Souza, C., Burger Veríssimo, W., Auxiliadora Costa Matos, M., Pedrosa Lisboa, T., and Camargo Matos, R. "Development of an electrochemical sensor utilizing recycled ABS filaments for 3D printing in the determination of diuron," *Microchemical Journal* Vol. 201, 2024, p. 110454.
https://doi.org/10.1016/j.microc.2024.110454.

[57] Srinivasaraghavan Govindarajan, R., Sikulskyi, S., Ren, Z., Stark, T., and Kim, D. "Characterization of Photocurable IP-PDMS for Soft Micro Systems Fabricated by Two-Photon Polymerization 3D Printing," *Polymers* Vol. 15, No. 22, 2023, p. 4377. https://doi.org/10.3390/polym15224377.

[58] Mamatha, S., Biswas, P., Ramavath, P., Das, D., and Johnson, R. "3D printing of complex shaped alumina parts," *Ceramics International* Vol. 44, No. 16, 2018, pp. 19278-19281. https://doi.org/10.1016/j.ceramint.2018.07.153.

[59] Chen, H., Pan, Y., Chen, B., Li, J., Gui, Z., Chen, J., Yan, H., Zeng, Y., and Chen, J. "Fabrication of porous aluminum ceramics beyond device resolution via stereolithography 3D printing," *Ceramics International* Vol. 49, No. 11, Part B, 2023, pp. 18463-18469. https://doi.org/10.1016/j.ceramint.2023.02.218.

[60] Zhang, J., Serra, M., Elizalde, S., Yarahmadi, M., Cabezas, L., Cabrera, J. M., Fargas, G., and Llanes, L. "Additive manufacturing of sensor prototype based on 3D-extrusion-printed zirconia ceramics," *Ceramics International* Vol. 50, No. 11, Part B, 2024, pp. 20088-20097. https://doi.org/10.1016/j.ceramint.2024.03.132.

[61] Boretti, A., and Castelletto, S. "A perspective on 3D printing of silicon carbide," *Journal of the European Ceramic Society* Vol. 44, No. 3, 2024, pp. 1351-1360. https://doi.org/10.1016/j.jeurceramsoc.2023.10.041.

[62] Al Rashid, A., Ahmed, W., Khalid, M. Y., and Koç, M. "Vat photopolymerization of polymers and polymer composites: Processes and applications," *Additive Manufacturing* Vol. 47, 2021, p. 102279. https://doi.org/10.1016/j.addma.2021.102279.

[63] Sikulskyi, S., Srinivasaraghavan Govindarajan, R., Stark, T., Ren, Z., Reed, N., and Kim, D. "Two-photon polymerized wetting morphologies for tunable external and internal electrode micropatterning," *Additive Manufacturing*, 2024, p. 104220. https://doi.org/10.1016/j.addma.2024.104220.

[64] Kumar, S., Singh, H., Singh, I., Bharti, S., Kumar, D., Siebert, G., and Koloor, S. S. R. "A comprehensive review of FDM printing in sensor applications: Advancements and future perspectives," *Journal of Manufacturing Processes* Vol. 113, 2024, pp. 152-170. https://doi.org/10.1016/j.jmapro.2024.01.030.

[65] Kechagias, J., Chaidas, D., Vidakis, N., Salonitis, K., and Vaxevanidis, N. M. "Key parameters controlling surface quality and dimensional accuracy: a critical review of FFF process," *Materials and Manufacturing Processes* Vol. 37, No. 9, 2022, pp. 963-984. https://doi.org/10.1080/10426914.2022.2032144.

[66] Tepylo, N., Huang, X., and Patnaik, P. C. "Laser-Based Additive Manufacturing Technologies for Aerospace Applications," *Advanced Engineering Materials* Vol. 21, No. 11, 2019, p. 1900617. https://doi.org/10.1002/adem.201900617.

[67] Bellitti, P., Borghetti, M., Cantù, E., Sardini, E., and Serpelloni, M. "Resistive Sensors for Smart Objects: Analysis on Printing Techniques," *IEEE Transactions on Instrumentation and Measurement* Vol. 71, 2022, pp. 1-15. https://doi.org/10.1109/TIM.2022.3181941.

[68] Zou, X., Wen, L., and Hu, B. "A Bulk Acoustic Wave Strain Sensor for Near-Field Passive Wireless Sensing," *Sensors*; Vol. 23, No. 8, 2023. https://doi.org/10.3390/s23083904.

[69] Mengue, P., Paulmier, B., Hage-Ali, S., Floer, C., M'Jahed, H., Shvetsov, A., Zhgoon, S., and Elmazria, O. "SAW-RFID temperature and strain sensors on metallic substrates," *2021 IEEE Sensors*. 2021, pp. 1-4.

[70] Meitzler, A., Tiersten, H., Warner, A., Berlincourt, D., Couqin, G., and Welsh III, F. "IEEE standard on piezoelectricity." Society, 1988.

[71] Parangusan, H., Ponnamma, D., and AlMaadeed, M. A. A. "Investigation on the effect of γ-irradiation on the dielectric and piezoelectric properties of stretchable PVDF/Fe–ZnO nanocomposites for self-powering devices," *Soft Matter* Vol. 14, No. 43, 2018, pp. 8803-8813. https://doi.org/10.1039/C8SM01655K.

[72] Cauda, V., Stassi, S., Bejtka, K., and Canavese, G. "Nanoconfinement: an Effective Way to Enhance PVDF Piezoelectric Properties," *ACS Applied Materials & Interfaces* Vol. 5, No. 13, 2013, pp. 6430-6437. https://doi.org/10.1021/am4016878.

[73] Soin, N., Boyer, D., Prashanthi, K., Sharma, S., Narasimulu, A. A., Luo, J., Shah, T. H., Siores, E., and Thundat, T. "Exclusive self-aligned β-phase PVDF films with abnormal piezoelectric coefficient prepared via phase inversion," *Chemical Communications* Vol. 51, No. 39, 2015, pp. 8257-8260. https://doi.org/10.1039/C5CC01688F.

[74] Babu, I., and de With, G. "Highly flexible piezoelectric 0–3 PZT–PDMS composites with high filler content," *Composites Science and Technology* Vol. 91, 2014, pp. 91-97. https://doi.org/10.1016/j.compscitech.2013.11.027.

[75] Ponraj, B., Bhimireddi, R., and Varma, K. B. R. "Effect of nano- and micron-sized K0.5Na0.5NbO3 fillers on the dielectric and piezoelectric properties of PVDF composites," *Journal of Advanced Ceramics* Vol. 5, No. 4, 2016, pp. 308-320. https://doi.org/10.1007/s40145-016-0204-2.

[76] Kumar, S. N., and Kumar, P. "Dielectric and Pyroelectric Properties of Ferroelectric SBN–PVDF Composites Prepared by Hot-Uniaxial Press," *International Journal of Applied Ceramic Technology* Vol. 10, 2013, pp. E11-E17. https://doi.org/10.1111/j.1744-7402.2012.02808.x.

[77] Fortunato, M., Bidsorkhi, H. C., Bellis, G. D., Sarto, F., and Sarto, M. S. "Piezoelectric response of graphene-filled PVDF nanocomposites through Piezoresponse Force Microscopy (PFM)," *2017 IEEE 17th International Conference on Nanotechnology (IEEE-NANO)*. 2017, pp. 125-129.

[78] Fortunato, M., Bidsorkhi, H. C., Chandraiahgari, C. R., Bellis, G. D., Sarto, F., and Sarto, M. S. "PFM Characterization of PVDF Nanocomposite Films With Enhanced Piezoelectric Response," *IEEE Transactions on Nanotechnology* Vol. 17, No. 5, 2018, pp. 955-961. https://doi.org/10.1109/TNANO.2018.2833201.

[79] Arlt, K., and Wegener, M. "PZT / P(VDF-HFP) 0–3 composites: Preparation, electrical poling and piezoelectric properties," *2008 13th International Symposium on Electrets*. 2008, pp. B0503-B0503.

[80] Srinivasaraghavan Govindarajan, R. "Flexible Strain Detection Using Surface Acoustic Waves: Fabrication and Tests." 2020.

[81] Li, R., Zhao, Z., Chen, Z., and Pei, J. "Novel BaTiO3/PVDF composites with enhanced electrical properties modified by calcined BaTiO3 ceramic powders," *Materials Express* Vol. 7, No. 6, 2017, pp. 536-540. https://doi.org/10.1166/mex.2017.1393.

[82] Li, J., Zhao, C., Xia, K., Liu, X., Li, D., and Han, J. "Enhanced piezoelectric output of the PVDF-TrFE/ZnO flexible piezoelectric nanogenerator by surface modification," *Applied Surface Science* Vol. 463, 2019, pp. 626-634. https://doi.org/10.1016/j.apsusc.2018.08.266.

[83] Ponnamma, D., Aljarod, O., Parangusan, H., and Ali Al-Maadeed, M. A. "Electrospun nanofibers of PVDF-HFP composites containing magnetic nickel ferrite for energy harvesting application," *Materials Chemistry and Physics* Vol. 239, 2020, p. 122257. https://doi.org/10.1016/j.matchemphys.2019.122257.

[84] Chamankar, N., Khajavi, R., Yousefi, A. A., Rashidi, A., and Golestanifard, F. "A flexible piezoelectric pressure sensor based on PVDF nanocomposite fibers doped with PZT particles for energy harvesting applications," *Ceramics International* Vol. 46, No. 12, 2020, pp. 19669-19681. https://doi.org/10.1016/j.ceramint.2020.03.210.

[85] Wu, C. M., and Chou, M. H. "Polymorphism, piezoelectricity and sound absorption of electrospun PVDF membranes with and without carbon nanotubes," *Composites Science and Technology* Vol. 127, 2016, pp. 127-133. https://doi.org/10.1016/j.compscitech.2016.03.001.

[86] Sahoo, R., Mishra, S., Ramadoss, A., Mohanty, S., Mahapatra, S., and Nayak, S. K. "An approach towards the fabrication of energy harvesting device using Ca-doped ZnO/ PVDF-TrFE composite film," *Polymer* Vol. 205, 2020, p. 122869. https://doi.org/10.1016/j.polymer.2020.122869.

[87] Bhunia, R., Das, S., Dalui, S., Hussain, S., Paul, R., Bhar, R., and Pal, A. K. "Flexible nano-ZnO/polyvinylidene difluoride piezoelectric composite films as energy harvester," *Applied Physics A* Vol. 122, No. 7, 2016, p. 637. https://doi.org/10.1007/s00339-016-0161-1.

[88] Kim, H., Torres, F., Villagran, D., Stewart, C., Lin, Y., and Tseng, T.-L. B. "3D Printing of BaTiO3/PVDF Composites with Electric In Situ Poling for Pressure Sensor Applications," *Macromolecular Materials and Engineering* Vol. 302, No. 11, 2017, p. 1700229. https://doi.org/10.1002/mame.201700229.

[89] Kirkpatrick, M. B., Tarbutton, J. A., Le, T., and Lee, C. "Characterization of 3D printed piezoelectric sensors: Determiniation of d33 piezoelectric coefficient for 3D printed polyvinylidene fluoride sensors," *2016 IEEE SENSORS*. 2016, pp. 1-3.

[90] Ikei, A., Wissman, J., Sampath, K., Yesner, G., and Qadri, S. N. "Tunable In Situ 3D-Printed PVDF-TrFE Piezoelectric Arrays," *Sensors*; Vol. 21, No. 15, 2021. https://doi.org/10.3390/s21155032.

[91] Kim, H., Torres, F., Wu, Y., Villagran, D., Lin, Y., and Tseng, T.-L. B. "Integrated 3D printing and corona poling process of PVDF piezoelectric films for pressure sensor application," *Smart Materials and Structures* Vol. 26, No. 8, 2017, p. 085027. https://doi.org/10.1088/1361-665X/aa738e.

[92] Bodkhe, S., Turcot, G., Gosselin, F. P., and Therriault, D. "One-Step Solvent Evaporation-Assisted 3D Printing of Piezoelectric PVDF Nanocomposite Structures," *ACS Applied Materials & Interfaces* Vol. 9, No. 24, 2017, pp. 20833-20842. https://doi.org/10.1021/acsami.7b04095.

[93] Kim, H., Johnson, J., Chavez, L. A., Garcia Rosales, C. A., Tseng, T.-L. B., and Lin, Y. "Enhanced dielectric properties of three phase dielectric MWCNTs/BaTiO3/PVDF nanocomposites for energy storage using fused deposition modeling 3D printing," *Ceramics International* Vol. 44, No. 8, 2018, pp. 9037-9044. https://doi.org/10.1016/j.ceramint.2018.02.107.

[94] Yuan, X., Yan, A., Lai, Z., Liu, Z., Yu, Z., Li, Z., Cao, Y., and Dong, S. "A poling-free PVDF nanocomposite via mechanically directional stress field for self-powered pressure sensor application," *Nano Energy* Vol. 98, 2022, p. 107340. https://doi.org/10.1016/j.nanoen.2022.107340.

[95] Li, F., Xiang, D., Chiang, S., Tittmann, B. R., and Searfass, C. "Wireless surface acoustic wave radio frequency identification (SAW-RFID) sensor system for temperature and strain measurements," *2011 IEEE International Ultrasonics Symposium*. IEEE, 2011, pp. 822-825.

[96] Hempel, J., Finke, D., Steiert, M., Zeiser, R., Berndt, M., Wilde, J., and Reindl, L. "SAW strain sensors-high precision strain sensitivity investigation on chip-level," *2013 IEEE International Ultrasonics Symposium (IUS)*. IEEE, 2013, pp. 1942-1945.

[97] Donohoe, B., Geraghty, D., and O'Donnell, G. E. "Wireless calibration of a surface acoustic wave resonator as a strain sensor," *IEEE Sensors Journal* Vol. 11, No. 4, 2010, pp. 1026-1032. https://doi.org/10.1109/JSEN.2010.2070492.

[98] Binder, A., Bruckner, G., Schobernig, N., and Schmitt, D. "Wireless Surface Acoustic Wave Pressure and Temperature Sensor With Unique Identification Based on ${\rm LiNbO} _ {3} $," *IEEE Sensors Journal* Vol. 13, No. 5, 2013, pp. 1801-1805. https://doi.org/10.1109/JSEN.2013.2241052.

[99] Della Lucia, F., Zambrozi Jr, P., Frazatto, F., Piazzetta, M., and Gobbi, A. "Design, fabrication and characterization of saw pressure sensors for extreme operation conditions," *Procedia Engineering* Vol. 87, 2014, pp. 540-543. https://doi.org/10.1016/j.proeng.2014.11.544.

[100] Greve, D. W., Chin, T.-L., Zheng, P., Ohodnicki, P., Baltrus, J., and Oppenheim, I. J. "Surface acoustic wave devices for harsh environment wireless sensing," *Sensors* Vol. 13, No. 6, 2013, pp. 6910-6935. https://doi.org/10.3390/s130606910.

[101] Devkota, J., Ohodnicki, P. R., and Greve, D. W. "SAW sensors for chemical vapors and gases," *Sensors* Vol. 17, No. 4, 2017, p. 801. https://doi.org/10.3390/s17040801.

[102] Feng, B., Jin, H., Fang, Z., Yu, Z., Dong, S., and Luo, J. "Flexible strain sensor based on ultra-thin quartz plate," *IEEE Sensors Journal*, 2021. https://doi.org/10.1109/JSEN.2021.3088473.

[103] Li, L., Peng, B., Zhu, J., He, Z., Yang, Y., and Zhang, W. "Strain Measurements With Langasite SAW Resonators at High Temperature," *IEEE Sensors Journal* Vol. 21, No. 4, 2020, pp. 4688-4695. https://doi.org/10.1109/JSEN.2020.3032477.

[104] Nicolay, P., Chambon, H., Bruckner, G., Gruber, C., Ballandras, S., Courjon, E., and Stadler, M. "A LN/Si-Based SAW Pressure Sensor," *Sensors* Vol. 18, No. 10, 2018, p. 3482.
https://doi.org/10.3390/s18103482.

[105] Reindl, L., Shrena, I., Kenshil, S., and Peter, R. "Wireless measurement of temperature using surface acoustic waves sensors," *IEEE International Frequency Control Symposium and PDA Exhibition Jointly with the 17th European Frequency and Time Forum, 2003. Proceedings of the 2003*. IEEE, 2003, pp. 935-941.

[106] Ren, J., Anurakparadorn, K., Gu, H., Zhao, M., and Wei, X. "Design of SAW sensor for longitudinal strain measurement with improved sensitivity," *Microsystem Technologies* Vol. 25, No. 1, 2019, pp. 351-359.
https://doi.org/10.1007/s00542-018-3970-7.

[107] Xu, H., Dong, S., Xuan, W., Farooq, U., Huang, S., Li, M., Wu, T., Jin, H., Wang, X., and Luo, J. "Flexible surface acoustic wave strain sensor based on single crystalline LiNbO3 thin film," *Applied Physics Letters* Vol. 112, No. 9, 2018, p. 093502.
https://doi.org/10.1063/1.5021663.

[108] Smith, W. R., Gerard, H. M., Collins, J. H., Reeder, T. M., and Shaw, H. J. "Analysis of interdigital surface wave transducers by use of an equivalent circuit model," *IEEE transactions on microwave theory and techniques* Vol. 17, No. 11, 1969, pp. 856-864.
https://doi.org/10.1109/TMTT.1969.1127075.

[109] Ro, R., Tung, H.-Y., and Wu, S.-J. "Design of two-track surface acoustic wave filters with width-controlled reflectors," *Japanese journal of applied physics* Vol. 43, No. 2R, 2004, p. 688.
https://doi.org/10.1143/JJAP.43.688.

[110] Krishnamurthy, S. *Wireless passive surface acoustic wave (SAW) sensing system*: Western Michigan University, 2007.

[111] Elsherbini, M., Elkordy, M., and Gomaa, A. "Using COMSOL to model high frequency surface acoustic wave (SAW) device," *Journal of Electrical and Electronics Engineering Research* Vol. 8, No. 1, 2016, pp. 1-8.
http://dx.doi.org/10.5897/JEEER2015.0557.

[112] Bing, C. Y., Mohanan, A. A., Saha, T., Ramanan, R. N., Parthiban, R., and Ramakrishnan, N. "Microfabrication of surface acoustic wave device using UV LED photolithography technique," *Microelectronic engineering* Vol. 122, 2014, pp. 9-12.
https://doi.org/10.1016/j.mee.2014.03.011.

[113] El Gowini, M. M., and Moussa, W. A. "A reduced three dimensional model for SAW sensors using finite element analysis," *Sensors* Vol. 9, No. 12, 2009, pp. 9945-9964.

https://doi.org/10.3390/s91209945.

[114] Holmström, J., Holweg, M., Khajavi, S. H., and Partanen, J. "The direct digital manufacturing (r) evolution: definition of a research agenda," *Operations Management Research* Vol. 9, No. 1, 2016, pp. 1-10. https://doi.org/10.1007/s12063-016-0106-z.

[115] Sajkiewicz, P., Wasiak, A., and Gocłowski, Z. "Phase transitions during stretching of poly (vinylidene fluoride)," *European polymer journal* Vol. 35, No. 3, 1999, pp. 423-429. https://doi.org/10.1016/S0014-3057(98)00136-0.

[116] Bharti, V., Kaura, T., and Nath, R. "Ferroelectric hysteresis in simultaneously stretched and corona-poled PVDF films," *IEEE transactions on dielectrics and electrical insulation* Vol. 4, No. 6, 1997, pp. 738-741. https://doi.org/10.1109/94.654689.

[117] Kumar, G. S., Vishnupriya, D., Chary, K. S., and Patro, T. U. "High dielectric permittivity and improved mechanical and thermal properties of poly (vinylidene fluoride) composites with low carbon nanotube content: effect of composite processing on phase behavior and dielectric properties," *Nanotechnology* Vol. 27, No. 38, 2016, p. 385702. https://doi.org/10.1088/0957-4484/27/38/385702.

[118] Seema, A., Dayas, K., and Varghese, J. M. "PVDF-PZT-5H composites prepared by hot press and tape casting techniques," *Journal of applied polymer science* Vol. 106, No. 1, 2007, pp. 146-151. https://doi.org/10.1002/app.26673.

[119] Srinivasaraghavan Govindarajan, R., Rojas-Nastrucci, E., and Kim, D. "Strain sensing using flexible surface acoustic wave sensor," *Sensors and Smart Structures Technologies for Civil, Mechanical, and Aerospace Systems 2020*. Vol. 11379, International Society for Optics and Photonics, 2020, p. 1137912.

[120] Chen, D., Heyer, S., Ibbotson, S., Salonitis, K., Steingrímsson, J. G., and Thiede, S. "Direct digital manufacturing: definition, evolution, and sustainability implications," *Journal of Cleaner Production* Vol. 107, 2015, pp. 615-625. https://doi.org/10.1016/j.jclepro.2015.05.009.

[121] Cai, X., Lei, T., Sun, D., and Lin, L. "A critical analysis of the α, β and γ phases in poly (vinylidene fluoride) using FTIR," *RSC advances* Vol. 7, No. 25, 2017, pp. 15382-15389. https://doi.org/10.1039/C7RA01267E.

[122] Medeiros, K. A. R., Rangel, E. Q., Sant'Anna, A. R., Louzada, D. R., Barbosa, C. R. H., and d'Almeida, J. R. M. "Evaluation of the electromechanical behavior of polyvinylidene fluoride used as a component of risers in the offshore oil industry," *Oil & Gas Science and Technology–Revue d'IFP Energies nouvelles* Vol. 73, 2018, p. 48. https://doi.org/10.2516/ogst/2018058.

[123] Yan, X., Suzuki, T., Kitahama, Y., Sato, H., Itoh, T., and Ozaki, Y. "A study on the interaction of single-walled carbon nanotubes (SWCNTs) and polystyrene (PS) at the interface in SWCNT–PS nanocomposites using tip-enhanced Raman spectroscopy," *Physical Chemistry Chemical Physics* Vol. 15, No. 47, 2013, pp. 20618-20624. https://doi.org/10.1039/C3CP53859A.

[124] Tsentalovich, D. E., Headrick, R. J., Mirri, F., Hao, J., Behabtu, N., Young, C. C., and Pasquali, M. "Influence of carbon nanotube characteristics on macroscopic fiber properties," *ACS applied materials & interfaces* Vol. 9, No. 41, 2017, pp. 36189-36198. https://doi.org/10.1021/acsami.7b10968.

[125] Soluch, W. "Scattering matrix approach to one-port SAW resonators," *IEEE transactions on ultrasonics, ferroelectrics, and frequency control* Vol. 47, No. 6, 2000, pp. 1615-1618. https://doi.org/10.1109/FREQ.1999.841440.

[126] Augustine, R., Sarry, F., Kalarikkal, N., Thomas, S., Badie, L., and Rouxel, D. "Surface acoustic wave device with reduced insertion loss by electrospinning p (vdf–trfe)/zno nanocomposites," *Nano-micro letters* Vol. 8, No. 3, 2016, pp. 282-290. https://doi.org/10.1007/s40820-016-0088-2.

[127] Rathod, V. T. "A review of electric impedance matching techniques for piezoelectric sensors, actuators and transducers," *Electronics* Vol. 8, No. 2, 2019, p. 169. https://doi.org/10.3390/electronics8020169.

[128] Achour, B., Aloui, N., Fourati, N., Zerrouki, C., and Yaakoubi, N. "Modelling and simulation of SAW delay line sensors with COMSOL Multiphysics," *MOL2NET 2018, International Conference on Multidisciplinary Sciences, 4th edition*. MDPI, 2018, p. 5887.

[129] Bharati, M., Rana, L., Tomar, M., and Gupta, V. "Theoretical simulations of SAW based sensor on PVDF," *Materials Today: Proceedings* Vol. 47, 2021, pp. 1538-1541. https://doi.org/10.1016/j.matpr.2021.03.295.

[130] Madiyar, F., Ghate, S., Nielsen, K., Govindarajan, R. S., Kim, D., and Stark, T. "Light-Enhanced Micropyramidal Sensors for Interleukin-6 Impedance Detection," *2024 IEEE Aerospace Conference*. 2024, pp. 1-8.

[131] Stark, T., Sikulskyi, S., Srinivasaraghavan Govindarajan, R., and Kim, D. "Hydrophilic surface morphology for intricate conductive coatings," *SPIE Smart Structures + Nondestructive Evaluation*. Vol. 12490, SPIE, 2023.

[132] Zhang, Q., Han, T., Tang, G., Chen, J., and Hashimoto, K.-y. "SAW characteristics of AlN/SiO 2/3C-SiC layered structure with embedded electrodes," *IEEE Transactions on Ultrasonics, Ferroelectrics, and Frequency Control* Vol. 63, No. 10, 2016, pp. 1608-1612. https://doi.org/10.1109/ULTSYM.2015.0116.

[133] Hao, W., Liu, J., Liu, M., Liang, Y., and He, S. "Mass sensitivity optimization of a surface acoustic wave sensor incorporating a resonator configuration," *Sensors* Vol. 16, No. 4, 2016, p. 562. https://doi.org/10.3390/s16040562.

[134] Wang, T., Green, R., Guldiken, R., Wang, J., Mohapatra, S., and Mohapatra, S. S. "Finite element analysis for surface acoustic wave device characteristic properties and sensitivity," *Sensors* Vol. 19, No. 8, 2019, p. 1749. https://doi.org/10.3390/s19081749.

[135] Kuypers, J. H., and Pisano, A. P. "Green's function analysis of Lamb wave resonators," *2008 IEEE Ultrasonics Symposium*. IEEE, 2008, pp. 1548-1551.

[136] Legrand, J. "Structure and ferroelectric properties of P (VDF-TrFE) copolymers," *Ferroelectrics* Vol. 91, No. 1, 1989, pp. 303-317. https://doi.org/10.1080/00150198908015747.

[137] Mao, D., Gnade, B. E., and Quevedo-Lopez, M. A. "Ferroelectric properties and polarization switching kinetic of poly (vinylidene fluoride-trifluoroethylene) copolymer," *Ferroelectrics-Physical Effects*, 2011, pp. 78-100. https://doi.org/10.5772/17147.

[138] Yuan, X., Gao, X., Shen, X., Yang, J., Li, Z., and Dong, S. "A 3D-printed, alternatively tilt-polarized PVDF-TrFE polymer with enhanced piezoelectric effect for self-powered sensor application," *Nano Energy* Vol. 85, 2021, p. 105985. https://doi.org/10.1016/j.nanoen.2021.105985.

[139] Jia, N., He, Q., Sun, J., Xia, G., and Song, R. "Crystallization behavior and electroactive properties of PVDF, P (VDF-TrFE) and their blend films," *Polymer Testing* Vol. 57, 2017, pp. 302-306. https://doi.org/10.1016/j.polymertesting.2016.12.003.

[140] Sankaranarayanan, S. K., and Bhethanabotla, V. R. "Design of efficient focused surface acoustic wave devices for potential microfluidic applications," *Journal of Applied Physics* Vol. 103, No. 6, 2008, p. 064518. https://doi.org/10.1063/1.2891577.

[141] Zheng, T., Liu, Y., Xu, C., Lu, H., and Wang, C. "Focusing surface acoustic waves assisted electrochemical detector in microfluidics," *Electrophoresis* Vol. 41, No. 10-11, 2020, pp. 860-866. https://doi.org/10.1002/elps.201900315.

[142] Yatsuda, H. "Design techniques for SAW filters using slanted finger interdigital transducers," *IEEE transactions on ultrasonics, ferroelectrics, and frequency control* Vol. 44, No. 2, 1997, pp. 453-459. https://doi.org/10.1109/58.585130.

[143] Ziping, W., Xiqiang, X., Lei, Q., Jiatao, W., Yue, F., and Maoyuan, T. "Research on the Progress of Interdigital Transducer (IDT) for Structural Damage Monitoring," *Journal of Sensors* Vol. 2021, 2021, pp. 1-10. https://doi.org/10.1155/2021/6630658.

[144] Wu, T.-T., Tang, H.-T., Chen, Y.-Y., and Liu, P.-L. "Analysis and design of focused interdigital transducers," *IEEE transactions on ultrasonics, ferroelectrics, and frequency control* Vol. 52, No. 8, 2005, pp. 1384-1392. https://doi.org/10.1109/TUFFC.2005.1509798.

[145] Rufo, J., Cai, F., Friend, J., Wiklund, M., and Huang, T. J. "Acoustofluidics for biomedical applications," *Nature Reviews Methods Primers* Vol. 2, No. 1, 2022, p. 30. https://doi.org/10.1038/s43586-022-00109-7.

[146] Srinivasaraghavan Govindarajan, R., Stark, T., Sikulskyi, S., Madiyar, F., and Kim, D. "Piezoelectric strain sensor through reverse replication based on two-photon polymerization," *SPIE Smart Structures + Nondestructive Evaluation*. Vol. 12046, SPIE, 2022.

[147] Srinivasaraghavan Govindarajan, R., Madiyar, F., and Kim, D. "Flexible Piezoelectric Wave-Based Sensor: Numerical Analysis And Validation," *Smart Materials, Adaptive Structures and Intelligent Systems*. Vol. 86274, American Society of Mechanical Engineers, 2022, p. V001T05A007.

[148] Srinivasaraghavan Govindarajan, R., Madiyar, F., and Kim, D. "Wave-based sensor responses with embedded electrode layouts," *SPIE Smart Structures + Nondestructive Evaluation*. Vol. 12486, SPIE, 2023.

[149] Song, S., Wang, Q., Zhou, J., and Riaud, A. "Design of interdigitated transducers for acoustofluidic applications," *Nanotechnology and Precision Engineering* Vol. 5, No. 3, 2022, p. 035001. https://doi.org/10.1063/10.0013405.

[150] Srinivasaraghavan Govindarajan, R., Xu, X., Sikulskyi, S., Madiyar, F., Rojas-Nastrucci, E., and Kim, D. "Additive manufacturing of flexible nanocomposite SAW sensor for strain detection," *Sensors and Smart Structures Technologies for Civil, Mechanical, and Aerospace Systems 2021*. Vol. 11591, International Society for Optics and Photonics, Online, 22 March 2021, p. 115910F.

[151] Liu, G., Li, Z., Li, X., Li, Y., Tang, H., Wang, M., and Yang, Z. "Design and experiment of a focused acoustic sorting chip based on TSAW separation mechanism," *Microsystem Technologies* Vol. 26, 2020, pp. 2817-2828. https://doi.org/10.1007/s00542-020-04828-3.

[152] Hao, Z., Park, M., Kim, D. G., Clark, A., Dargis, R., Zhu, H., and Ansari, A. "Single Crystalline ScAlN Surface Acoustic Wave Resonators with Large Figure of Merit ($Q \times k_t^2$)," *2019 IEEE MTT-S International Microwave Symposium (IMS)*. IEEE, 2019, pp. 786-789.

[153] Asseko Ondo, J. C., Blampain, E. J. J., N'Tchayi Mbourou, G., Mc Murtry, S., Hage-Ali, S., and Elmazria, O. "FEM modeling of the temperature influence on the performance of SAW sensors operating at gigahertz frequency range and at high temperature up to 500 C," *Sensors* Vol. 20, No. 15, 2020, p. 4166. https://doi.org/10.3390/s20154166.

[154] Thongsanitgarn, P., Watcharapasorn, A., and Jiansirisomboon, S. "Electrical and mechanical properties of PZT/PVDF 0–3 composites," *Surface review and letters* Vol. 17, No. 01, 2010, pp. 1-7. https://doi.org/10.1142/S0218625X10013540.

[155] Arlt, K., and Wegener, M. "Piezoelectric PZT/PVDF-copolymer 0-3 composites: aspects on film preparation and electrical poling," *IEEE Transactions on Dielectrics and Electrical Insulation* Vol. 17, No. 4, 2010, pp. 1178-1184. https://doi.org/10.1109/TDEI.2010.5539688.

[156] Koroglu, L., Ayas, E., and Ay, N. "3D Printing of Polyvinylidene Fluoride Based Piezoelectric Nanocomposites: An Overview," *Macromolecular Materials and Engineering* Vol. 306, No. 10, 2021, p. 2100277. https://doi.org/10.1002/mame.202100277.

[157] Ni, Y., Ji, R., Long, K., Bu, T., Chen, K., and Zhuang, S. "A review of 3D-printed sensors," *Applied Spectroscopy Reviews* Vol. 52, No. 7, 2017, pp. 623-652. https://doi.org/10.1080/05704928.2017.1287082.

[158] Tawk, C., and Alici, G. "A review of 3D-printable soft pneumatic actuators and sensors: research challenges and opportunities," *Advanced Intelligent Systems* Vol. 3, No. 6, 2021, p. 2000223. https://doi.org/10.1002/aisy.202000223.

[159] Sikulskyi, S., Ren, Z., Mekonnen, D. T., Holyoak, A., Srinivasaraghavan Govindarajan, R., and Kim, D. "Additively manufactured unimorph dielectric elastomer actuators: Design, materials, and fabrication," *Frontiers in Robotics and AI* Vol. 9, 2022. https://doi.org/10.3389/frobt.2022.1034914.

[160] Srinivasaraghavan Govindarajan, R., Ren, Z., Madiyar, F., and Kim, D. "Additive Manufacturing of Photocurable PVDF-Based Capacitive Sensor," *ASME 2023 Conference on Smart Materials, Adaptive Structures and Intelligent Systems*. Vol. ASME 2023 Conference on Smart Materials, Adaptive Structures and Intelligent Systems, Austin, Texas, USA, 11-13 September 2023.

[161] Che, J., Zakri, C., Bronchy, M., Neri, W., Ly, I., Poulin, P., and Yuan, J. "Inkjet Printing of All Aqueous Inks to Flexible Microcapacitors for High-Energy Storage," *Advanced Functional Materials* Vol. 33, No. 37, 2023, p. 2301544. https://doi.org/10.1002/adfm.202301544.

[162] Lee, C., and Tarbutton, J. A. "Electric poling-assisted additive manufacturing process for PVDF polymer-based piezoelectric device applications," *Smart Materials and Structures* Vol. 23, No. 9, 2014, p. 095044. https://doi.org/10.1088/0964-1726/23/9/095044.

[163] Mehta, A., Singh, R., Pabla, B., and Kumar, V. "On 3D printed polyvinylidene fluoride-based smart energy storage devices," *Journal of Thermoplastic Composite Materials*, 2023, p. 08927057231208133. https://doi.org/10.1177/08927057231208133.

[164] Quan, H., Zhang, T., Xu, H., Luo, S., Nie, J., and Zhu, X. "Photo-curing 3D printing technique and its challenges," *Bioactive materials* Vol. 5, No. 1, 2020, pp. 110-115. https://doi.org/10.1016/j.bioactmat.2019.12.003.

[165] Shim, J., Son, D. I., Lee, J. S., Lee, J., Lim, G.-H., Cho, H., Kim, E.-y., Bu, S. D., Sungbin, I., and Jeong, C. K. "BNNT-ZnO QDs nanocomposites for improving piezoelectric nanogenerator and piezoelectric properties of boron nitride nanotube," *Nano Energy* Vol. 93, 2022, p. 106886. https://doi.org/10.1016/j.nanoen.2021.106886.

[166] Poudel, A., Fernandez, M. A., Tofail, S. A., and Biggs, M. J. "Boron nitride nanotube addition enhances the crystallinity and cytocompatibility of PVDF-TrFE," *Frontiers in chemistry* Vol. 7, 2019, p. 364. https://doi.org/10.3389/fchem.2019.00364.

[167] Kundalwal, S., and Choyal, V. "Enhancing the piezoelectric properties of boron nitride nanotubes through defect engineering," *Physica E: Low-dimensional Systems and Nanostructures* Vol. 125, 2021, p. 114304. https://doi.org/10.1016/j.physe.2020.114304.

[168] Yamakov, V., Park, C., Kang, J. H., Chen, X., Ke, C., and Fay, C. "Piezoelectric and elastic properties of multiwall boron-nitride nanotubes and their fibers: A molecular dynamics study," *Computational Materials Science* Vol. 135, 2017, pp. 29-42. https://dx.doi.org/10.1016/j.commatsci.2017.03.050.

[169] Nakhmanson, S. M., Calzolari, A., Meunier, V., Bernholc, J., and Nardelli, M. B. "Spontaneous polarization and piezoelectricity in boron nitride nanotubes," *Physical Review B* Vol. 67, No. 23, 2003, p. 235406. http://dx.doi.org/10.1103/PhysRevB.67.235406.

[170] Xiang, H., Chen, Z., and Yang, J. "Electronic and piezoelectric properties of BN nanotubes from hybrid density functional method," *Journal of Computational and Theoretical Nanoscience* Vol. 3, No. 5, 2006, pp. 838-842. https://doi.org/10.48550/arXiv.cond-mat/0510412.

[171] Srinivasaraghavan Govindarajan, R., Ren, Z., Melendez, I., Boetcher, S. K., Madiyar, F., and Kim, D. "Polymer Nanocomposite Sensors with Improved Piezoelectric Properties through Additive Manufacturing," *Sensors* Vol. 24, No. 9, 2024, p. 2694. https://doi.org/10.3390/s24092694.

[172] Xu, J., Fu, C., Chu, H., Wu, X., Tan, Z., Qian, J., Li, W., Song, Z., Ran, X., and Nie, W. "Enhanced energy density of PVDF-based nanocomposites via a core–shell strategy," *Scientific reports* Vol. 10, No. 1, 2020, pp. 1-14. https://doi.org/10.1038/s41598-020-73884-6.

[173] Shanshool, H. M., Yahaya, M., Yunus, W. M. M., and Abdullah, I. Y. "Measurements of nonlinear optical properties of PVDF/ZnO using Z-scan technique," *Brazilian Journal of Physics* Vol. 45, No. 5, 2015, pp. 538-544. https://doi.org/10.1007/s13538-015-0345-8.

[174] Wu, H., Chen, P., Yan, C., Cai, C., and Shi, Y. "Four-dimensional printing of a novel acrylate-based shape memory polymer using digital light processing," *Materials & Design* Vol. 171, 2019, p. 107704. https://doi.org/10.1016/j.matdes.2019.107704.

[175] Hidalgo, A., Makarov, V., Morell, G., and Weiner, B. "High-yield synthesis of cubic and hexagonal boron nitride nanoparticles by laser chemical vapor decomposition of borazine," *Dataset Papers in Science* Vol. 2013, 2012. http://dx.doi.org/10.7167/2013/281672.

[176] Xiao, Y.-j., Wang, W.-y., Lin, T., Chen, X.-j., Zhang, Y.-t., Yang, J.-h., Wang, Y., and Zhou, Z.-w. "Largely enhanced thermal conductivity and high dielectric constant of poly (vinylidene fluoride)/boron nitride composites achieved by adding a few carbon nanotubes," *The Journal of Physical Chemistry C* Vol. 120, No. 12, 2016, pp. 6344-6355. https://doi.org/10.1021/acs.jpcc.5b12651.

[177] Tsonos, C., Pandis, C., Soin, N., Sakellari, D., Myrovali, E., Kripotou, S., Kanapitsas, A., and Siores, E. "Multifunctional nanocomposites of poly (vinylidene fluoride) reinforced by carbon nanotubes and magnetite nanoparticles," *Express Polymer Letters* Vol. 9, No. 12, 2015. http://dx.doi.org/10.3144/expresspolymlett.2015.99.

[178] Uyor, U., Popoola, A., and Popoola, O. "Flexible dielectric polymer nanocomposites with improved thermal energy management for energy-power applications," *Frontiers in Energy Research* Vol. 11, 2023, p. 1114512. https://doi.org/10.3389/fenrg.2023.1114512.

[179] Lee, J. E., Nam, R., Jakubinek, M. B., Ashrafi, B., and Naguib, H. E. "Development of PVDF nanocomposite with single-walled carbon nanotubes (SWCNT) and boron nitride nanotubes (BNNT) for soft morphing actuator," *Smart Materials and Structures* Vol. 30, No. 5, 2021, p. 055014. https://doi.org/10.1088/1361-665X/abf23d.

[180] Chen, Z., Wei, Q., Tang, G., Shi, H., and Qin, L. "Preparation and Thermal Conductivity Enhancement of Boron Nitride Nano-Material PiG Composite," *Nanomaterials* Vol. 13, No. 6, 2023, p. 1106. https://doi.org/10.3390/nano13061106.

[181] Zhang, C., Wei, W., Sun, H., and Zhu, Q. "Performance enhancements in poly (vinylidene fluoride)-based piezoelectric films prepared by the extrusion-casting process," *Journal of Materials Science: Materials in Electronics* Vol. 32, 2021, pp. 21837-21847. https://doi.org/10.1007/s10854-021-06416-1.

[182] Wu, C.-M., Chou, M.-H., and Zeng, W.-Y. "Piezoelectric response of aligned electrospun polyvinylidene fluoride/carbon nanotube nanofibrous membranes," *Nanomaterials* Vol. 8, No. 6, 2018, p. 420. https://doi.org/10.3390%2Fnano8060420.

[183] Reed, N., Srinivasaraghavan Govindarajan, R., and Kim, D. "Characterization of Adhesive Microstructures for Improved Bonding in Embedded Sensors," *AIAA SCITECH 2024 Forum*. 2024, p. 0262.

[184] Goswami, P., and Gupta, G. "Recent progress of flexible NO2 and NH3 gas sensors based on transition metal dichalcogenides for room temperature sensing," *Materials Today Chemistry* Vol. 23, 2022, p. 100726. https://doi.org/10.1016/j.mtchem.2021.100726.

[185] Nikolic, M. V., Milovanovic, V., Vasiljevic, Z. Z., and Stamenkovic, Z. "Semiconductor gas sensors: Materials, technology, design, and application," *Sensors* Vol. 20, No. 22, 2020, p. 6694. https://doi.org/10.3390/s20226694.

[186] Zhou, X., Tan, Q., Liang, X., Lin, B., Guo, T., and Gan, Y. "Novel multilayer SAW temperature sensor for ultra-high temperature environments," *Micromachines* Vol. 12, No. 6, 2021, p. 643. https://doi.org/10.3390/mi12060643.

[187] Patial, P., and Deshwal, M. "Systematic review on design and development of efficient semiconductor based surface acoustic wave gas sensor," *Transactions on Electrical and Electronic Materials* Vol. 22, No. 4, 2021, pp. 385-393. https://doi.org/10.1007/s42341-021-00332-1.

[188] Ding, J., Chen, S., Han, N., Shi, Y., Hu, P., Li, H., and Wang, J. "Aerosol assisted chemical vapour deposition of nanostructured ZnO thin films for NO2 and ethanol monitoring," *Ceramics International* Vol. 46, No. 10, 2020, pp. 15152-15158. https://doi.org/10.1016/j.ceramint.2020.03.051.

[189] Waikar, M. R., Raste, P. M., Sonker, R. K., Gupta, V., Tomar, M., Shirsat, M. D., and Sonkawade, R. G. "Enhancement in NH3 sensing performance of ZnO thin-film via gamma-irradiation," *Journal of Alloys and Compounds* Vol. 830, 2020, p. 154641. https://doi.org/10.1016/j.jallcom.2020.154641.

[190] Kang, Y., Yu, F., Zhang, L., Wang, W., Chen, L., and Li, Y. "Review of ZnO-based nanomaterials in gas sensors," *Solid State Ionics* Vol. 360, 2021, p. 115544. https://doi.org/10.1016/j.ssi.2020.115544.

[191] Hasan, M. N., Maity, S., Sarkar, A., Bhunia, C. T., Acharjee, D., and Joseph, A. M. "Simulation and fabrication of SAW-based gas sensor with modified surface state of active layer and electrode orientation for enhanced H2 gas sensing," *Journal of Electronic Materials* Vol. 46, No. 2, 2017, p. 679. https://doi.org/10.1007/s11664-016-5128-7.

[192] Lee, S. D., Nam, S.-H., Kim, M.-H., and Boo, J.-H. "Synthesis and Photocatalytic Property of ZnO nanoparticles Prepared by Spray-Pyrolysis Method," *Physics Procedia* Vol. 32, 2012, pp. 320-326. https://doi.org/10.1016/j.phpro.2012.03.563.

[193] Alvarado, J. A., Maldonado, A., Juarez, H., and Pacio, M. "Synthesis of Colloidal ZnO Nanoparticles and Deposit of Thin Films by Spin Coating Technique," *Journal of Nanomaterials* Vol. 2013, 2013, p. 903191. https://doi.org/10.1155/2013/903191.

[194] Mohammed, R., Ahmed, S., Abdulrahman, A., and Hamad, S. "Synthesis and Characterizations of ZnO Thin Films Grown by Physical Vapor Deposition Technique," *Journal of Applied Science and Technology Trends* Vol. 1, No. 2, 2020, pp. 135 - 139. 10.38094/jastt1456.

[195] Guan, Y. F., and Pedraza, A. J. "Synthesis and alignment of Zn and ZnO nanoparticles by laser-assisted chemical vapor deposition," *Nanotechnology* Vol. 19, No. 4, 2008, p. 045609. https://doi.org/10.1088/0957-4484/19/04/045609.

[196] Fernández de la Mora, J. "The Fluid Dynamics of Taylor Cones," *Annual Review of Fluid Mechanics* Vol. 39, No. Volume 39, 2007, 2007, pp. 217-243. https://doi.org/10.1146/annurev.fluid.39.050905.110159.

[197] Rohner, T. C., Lion, N., and Girault, H. H. "Electrochemical and theoretical aspects of electrospray ionisation," *Physical Chemistry Chemical Physics* Vol. 6, No. 12, 2004, pp. 3056-3068. https://doi.org/10.1039/B316836K.

[198] Marinov, G., Lovchinov, K., Madjarova, V., Strijkova, V., Vasileva, M., Malinowski, N., and Babeva, T. "Aluminum-doped zinc oxide thin films deposited by electrospray method," *Optical Materials* Vol. 89, 2019, pp. 390-395. https://doi.org/10.1016/j.optmat.2019.01.055.

[199] Li, W., Lin, J., Wang, X., Jiang, J., Guo, S., and Zheng, G. "Electrospray Deposition of ZnO Thin Films and Its Application to Gas Sensors," *Micromachines*; Vol. 9, No. 2, 2018. https://doi.org/10.3390/mi9020066.

[200] Rabeel, M., Javed, S., Khan, R., Akram, M. A., Rehman, S., Kim, D.-k., and Khan, M. F. "Controlling the wettability of ZnO thin films by spray pyrolysis for photocatalytic applications," *Materials* Vol. 15, No. 9, 2022, p. 3364. https://doi.org/10.3390/ma15093364.

[201] Mourzina, Y., Steffen, A., and Offenhäusser, A. "The evaporated metal masks for chemical glass etching for BioMEMS," *Microsystem technologies* Vol. 11, No. 2-3, 2005, pp. 135-140. https://doi.org/10.1007/s00542-004-0430-3.

[202] Pérez, M., Carou, D., Rubio, E. M., and Teti, R. "Current advances in additive manufacturing," *Procedia Cirp* Vol. 88, 2020, pp. 439-444. https://doi.org/10.1016/j.procir.2020.05.076.

[203] Ren, Z., Yang, Z., Srinivasaraghavan Govindarajan, R., Madiyar, F., Cheng, M., Kim, D., and Jiang, Y. "Two-Photon Polymerization of Butterfly Wing Scale Inspired Surfaces with Anisotropic Wettability," *ACS Applied Materials & Interfaces*, 2024. https://doi.org/10.1021/acsami.3c14765.

[204] Srinivasaraghavan Govindarajan, R., Stark, T., Madiyar, F., and Kim, D. "On the performance of PVDF based piezoelectric sensor with microstructures," *SPIE Smart Structures + Nondestructive Evaluation*. Vol. 12486, SPIE, 2023.

14 APPENDIX

Code used for getting theoretical scattering parameter (S_{11} & S_{21}) used in this research

```
clear all ;
rho=1780;E=3E9;nu=0.3;G=E/(2*(1+nu)); %Elastic properties of PVDF
v_s=sqrt(G/rho); %Shear wave velocity
v_r=v_s*(0.862+1.14*nu)/(1+nu); %SAW (Rayleigh wave) velocity on the free sections
v_m=v_r; %SAW velocity on the metallized sections is initially assumed to be the same as free sections.
lambda_r=0.0002; %SAW wavelength
f0=v_r/lambda_r; %center frequency
Nfp_in=6;Nfp_out=3; %Number of electrodes in the input and output IDTs, dictates bandwidth
C=1.5e-12;%Capacitance per finger pair per unit length, dictates IL
k_2=0.14; %Electromechanical coupling coefficient of PVDF, check in comsol
ws=1/8*lambda_r; %free section 1/4*lambda of a unit
wf=1/4*lambda_r; %metallized section 1/8*lambda of a unit
f_m=v_m/lambda_r; %frequency of metallized section
ap=8.5e-4; %Acoustic aperture
d=1e-3; %Length of the delay line (transmission line)
Z=1/(f0*C*ap*k_2); %acoustic impedance for free sections without fingers
Z_m=1/(f_m*C*ap*k_2); %acoustic impedance for the metallized sections with fingers
i=1;
f_min=1e6;
f_max=6.5e6;
for f=f_min:1000:f_max
lambda=v_r/f;
omega=2*pi*f;
%Computation of the ABCD matrix for a single finger
theta_f=2*pi*f*ws/v_r; %acoustic angle in free region
theta_m=2*pi*f*wf/v_m; %acoustic angle in metallized region
%Computation of the free region between fingers
A_f=cos(theta_f);
B_f=sqrt(-1)*Z*sin(theta_f);
C_f=sqrt(-1)*sin(theta_f)/Z;
D_f=cos(theta_f); %Computation of the metallized regions under fingers
A_m=cos(theta_m);
B_m=sqrt(-1)*Z_m*sin (theta_m);
C_m=sqrt(-1)*sin(theta_m)/Z_m;
D_m=cos(theta_m);
%Cascading matrix for a single finger to calculate 2x2 A_finger matrix
A_finger =[A_f B_f;C_f D_f]*[A_m B_m;C_m D_m]*[A_f B_f;C_f D_f];
%Single finger matrix value
A_se=A_finger(1,1);
B_se=A_finger(1,2);
C_se=A_finger(2,1);
D_se=A_finger(2,2);
theta_d=2*pi*f*d/v_r;
theta_e=acos(A_se);
Ze=B_se/(sqrt(-1)*sin(theta_e));
%transmission matrix for a single finger of the IDT
```

```
t11 =0.5*(2*A_se+(B_se/Z)+Z*C_se);
t12 =0.5*(Z*C_se-(B_se/Z));
t13 =((sqrt (-1)*tan(theta_e/2)*(Z^0.5))/(2*Ze))*(-A_se-1-(B_se/Z));
t21=-t12;
t22=conj(t11);
t23=sqrt(-1)*tan(theta_e/2)*(Z^0.5)*(1+A_se-(B_se/Z))/(2*Ze);
t31=2*t13;
t32=-2*t23;
t33=sqrt(-1)*omega*C*ap*0.5+sqrt(-1)*2*(tan(theta_e/2)/Ze)-sqrt(-
1)*(sin(theta_e)*(tan(theta_e/2)^2))/Ze;
t1 =[t11 t12;t21 t22]^Nfp_in;
t3 =[t11 t12;t21 t22]^Nfp_out;
t11_in=t1(1,1);
t12_in=t1(1,2);
t21_in=t1(2,1);
t22_in=t1(2,2);
t12_out=t3(1,2);
t11_out=t3(1,1);
t21_out=t3(2,1);
t22_out=t3(2,2);
Bp=[t13;t23]+[t11 t12;t21 t22]*[-t13;-t23];
Cp=[t31 t32]*[t11 t12;t21 t22]+[-t31 -t32];
t_33p=2*t33 +[t31 t32]*[-t13;-t23];
Tp=[t11 t12;t21 t22]^2;
BN_in=[0;0];
CN_in=[0 0];
BN_out=[0;0];
CN_out=[0 0];
t_33_out=(Nfp_out/2)*t_33p ;
t_33_in=(Nfp_in/2)*t_33p ;
%Input IDT
for i1=1:(Nfp_in/2)
BN_in=BN_in+(Tp^(i1-1))*Bp;
CN_in=CN_in+Cp*Tp^(i1-1);
t_33_in=t_33_in+((Nfp_in/2)-i1)*Cp*Tp^(i1-1)*Bp;
end
%Output IDT
for i2=1:(Nfp_out/2)
BN_out=BN_out+(Tp^(i2-1))*Bp;
CN_out=CN_out+Cp*Tp^(i2-1);
t_33_out=t_33_out+((Nfp_out/2)-i2)*Cp*Tp^(i2-1)*Bp;
end
t13_in=BN_in(1,1);
t13_out=BN_out(1,1);
t23_in=BN_in(2,1);
t23_out=BN_out(2,1);
t31_in=CN_in(1,1);
t31_out=CN_out(1,1);
t32_in=CN_in(1,2);
t32_out=CN_out(1,2);
%ABCD matrix of delay path
```

```
A_d=cos(theta_d);
B_d=sqrt(-1)*Z*sin (theta_d);
C_d=sqrt(-1)*sin(theta_d)/Z;
D_d=cos(theta_d);
%Computation of transmission matrix for delay path
d11=0.5*(2*A_d+(B_d/Z)+Z*C_d);
d12=0.5*(Z*C_d-(B_d/Z));
d21=-d12;
d22=0.5*(2*A_d-(B_d/Z)-Z*C_d);
d2=[d11 d12;d21 d22];
%Substitutions for convenience
s1=t1*d2*t3;
s2=t1*d2*[t13_out;t23_out];
s3=[t31_in t32_in]*d2*t3;
s4=[t31_in t32_in]*d2*[t13_out;t23_out];
%computing Y-parameter (Admittance) for the SAW-DL
y_11(i)=t_33_in-(s3(1,1)*t13_in/s1(1,1));
y_12(i)=s4(1,1)-(s3(1,1)*s2(1,1)/s1(1,1));
y_21(i)=-t31_out*t13_in/s1(1,1);
y_22(i)=t_33_out-(t31_out*s2(1,1)/s1(1,1));
%Computing S-parameters using the Y-parameters (assuming the input and output reference impedances
% are both equal to 50 ohm)
R1=50; R2=50; %Only real part of the impedance are considered
%modified S-parameter including source and load impedance
s_11_m(i)=((1-
R1*y_11(i))*(1+R2*y_22(i))+y_12(i)*y_21(i)*R1*R2)/((1+R1*y_11(i))*(1+R2*y_22(i))-
y_12(i)*y_21(i)*R1*R2);
s_21_m(i)=-2*sqrt(R1*R2)*y_12(i)/((1+R1*y_11(i))*(1+R2*y_22(i))-y_12(i)*y_21(i)*R1*R2);
i=i+1;
end
%Plot the S11 parameter in dB
figure(1);
f=f_min:1000:f_max;
y1=20*log10(abs(s_11_m));
plot(f,y1,'r');
xlim([f_min f_max]);
title('Frequency Response S_{11}','FontSize',16);
xlabel('Frequency/Hz','FontSize',14);
ylabel('S_{11}/dB','FontSize',14)
set(findall(gca,'type','line'),'linewidth',1,'Color','r')
grid off;
%Plot the S21 parameter in dB
figure(2);
f=f_min:1000:f_max;
y1=20*log10(abs(s_21_m));
plot(f,y1,'r');
xlim([f_min f_max]);
title('Frequency Response S_{21} (Insertion Loss)','FontSize',16);
xlabel('Frequency/Hz','FontSize',14);
ylabel('S_{21}/dB','FontSize',14)
set(findall(gca,'type','line'),'linewidth',1,'Color','b')
```

Code used for particle analysis used in this research,

```
clear all,
clc,
set(groot,'defaulttextinterpreter','latex');
set(groot, 'defaultAxesTickLabelInterpreter','latex');
set(groot, 'defaultLegendInterpreter','latex');
d1(:,1)=readtable('Results_BaTiO.xlsx','Range','D2:D383');
dba=table2array(d1);
mean_ba=mean(dba);
std_ba=std(dba);

%%
figure
hold on
hold on
hba=histogram(dba*1e3,15,'Normalization','probability','Facecolor','b','FaceA
lpha',0.8)
plot([420 420],[0 0.13],'LineStyle','--','Color','r','Linewidth',2)
lgd=legend('BaTiO_{3} 420 nm','Location','Northeast');
title(lgd,'Particles avg size')
set(lgd, 'interpreter', 'tex')
xlabel('Particle size (nm)', 'interpreter', 'tex')
ylabel('Probability', 'interpreter', 'tex')
grid on
xlim([300 600])
box
```

G-Code used for IDT lines using HYREL,

```
G53          ; clear offsets
G21          ; units        : mm
G91          ; coordinatess  : relative
G0 Z10               ; drop bed
G90          ; coordinates   : absolute
G28 X0 Y0      ; home, goto    : X and Y
G92 X0 Y0      ; home, set     : X and Y

;IDT line from starting point to the first finger = 7 mm
;Finger length = 5 mm
;wavelength = 0.6 mm
;Postivie to negative finger spacing = 0.3 mm
;Print head move rate = 160 mm/min
;Input to output spacing = 13 mm
;Input Finger number = 4
;Output Finger number = 2


G21 ; set units to millimeters
G90 ; use absolute coordinates
M82 ; use absolute distances for extrusion
G92 E0 ; reset extrusion distance
;announce new layer <0>
;---
T1
M756 S0.2
M790 ;execute any new layer actions
;---
G54 X7 Y30 ;Offset to the starting point, add 8 to Y to move print next pair of IDT
G1 Z0.000 F500.000 ; move to next layer (0)
G0 X0.000 Y0.000 F1000.000 ; move to first perimeter point
G1 X7.000 Y0.000 F160.000 ;
G1 X7.000 Y5.000 E0.00100 F160.000 ; perimeter
G0 X7.000 Y5.000 Z0.500 F1000.000 ; perimeter
G0 X7.000 Y0.000 Z0.500 F1000.000
G0 X7.000 Y0.000 Z0.000 F1000.000

G1 X7.600 Y0.000 E0.00100 F160.000 ; perimeter
G1 X7.600 Y5.000 E0.00100 F160.000 ; perimeter
G0 X7.600 Y5.000 Z0.500 F1000.000 ; perimeter
G0 X7.600 Y0.000 Z0.500 F1000.000
G0 X7.600 Y0.000 Z0.000 F1000.000

G1 X8.200 Y0.000 E0.00100 F160.000 ; perimeter
```

```
G1 X8.200 Y5.000 E0.00100 F160.000 ; perimeter
G0 X8.200 Y5.000 Z0.500 F1000.000 ; perimeter
G0 X8.200 Y0.000 Z0.500 F1000.000
G0 X8.200 Y0.000 Z0.000 F1000.000

G1 X8.800 Y0.000 E0.00100 F160.000 ; perimeter
G1 X8.800 Y5.000 E0.00100 F160.000 ; perimeter
G0 X8.800 Y5.000 Z0.500 F1000.000 ; perimeter
G0 X8.800 Y0.000 Z1.000 F1000.000

G0 X0.000 Y5.500 Z1.000
G0 X0.000 Y5.500 Z0.000
G1 X7.300 Y5.500 F160.000
G1 X7.300 Y0.500 E0.00100 F160.000 ; perimeter
G0 X7.300 Y0.500 Z0.500 F1000.000 ; perimeter
G0 X7.300 Y5.500 Z0.500 F1000.000
G0 X7.300 Y5.500 Z0.000 F1000.000

G1 X7.900 Y5.500 F160.000
G1 X7.900 Y0.500 E0.00100 F160.000 ; perimeter
G0 X7.900 Y0.500 Z0.500 F1000.000 ; perimeter
G0 X7.900 Y5.500 Z0.500 F1000.000
G0 X7.900 Y5.500 Z0.000 F1000.000

G1 X8.500 Y5.500 F160.000
G1 X8.500 Y0.500 E0.00100 F160.000 ; perimeter
G0 X8.500 Y0.500 Z0.500 F1000.000 ; perimeter
G0 X8.500 Y5.500 Z0.500 F1000.000
G0 X8.500 Y5.500 Z0.000 F1000.000

G1 X9.100 Y5.500 F160.000
G1 X9.100 Y0.500 E0.00100 F160.000 ; perimeter
G0 X9.100 Y0.500 Z0.500 F1000.000 ; perimeter
G0 X9.100 Y5.500 Z1.500 F1000.000

G0 X30.000 Y5.500 Z1.500
G0 X30.000 Y5.500 Z0.000

G1 X23.000 Y5.500 E0.00100 F160.000 ; perimeter
G1 X23.000 Y0.500 E0.00100 F160.000 ; perimeter
G0 X23.000 Y0.500 Z0.500 F1000.000 ; perimeter
G0 X23.000 Y5.500 Z0.500 F1000.000
G0 X23.000 Y5.500 Z0.000 F1000.000

G1 X22.400 Y5.500 E0.00100 F160.000 ; perimeter
G1 X22.400 Y0.500 E0.00100 F160.000 ; perimeter
```

```
G0 X22.400 Y0.500 Z1.500 F1000.000 ; perimeter

G0 X30.000 Y0.000 Z1.500
G0 X30.000 Y0.000 Z0.000

G1 X22.700 Y0.000 E0.00100 F160.000 ; perimeter
G1 X22.700 Y5.000 E0.00100 F160.000 ; perimeter
G0 X22.700 Y5.000 Z0.500 F1000.000 ; perimeter
G0 X22.700 Y0.000 Z0.500 F1000.000
G0 X22.700 Y0.000 Z0.000 F1000.000

G1 X22.100 Y0.000 E0.00100 F160.000 ; perimeter
G1 X22.100 Y5.000 E0.00100 F160.000 ; perimeter
G0 X22.100 Y5.000 Z1.500 F1000.000 ; perimeter
G0 X0.000 Y0.000 Z1.500 F1000.000


M106 T10 S0     ; fans, lasers  : off
M104 T10 S0     ; heads temps   : off
M140 S0         ; bed temp      : off

;

G91             ; coordinatess  : relative
G0 Z10          ; drop bed
G90             ; coordinates   : absolute
M84             ; motors        : disable
G53             ; clear offsets
M30             ; program       : end

; end of file
```